Effects of Particle Size Ratio on Single Particle Motion in Colloidal Dispersions

Thesis by

Nicholas J. Hoh

In Partial Fulfillment of the Requirements

for the Degree of

Doctor of Philosophy

California Institute of Technology

Pasadena, California

2013

(Defended May 31, 2013)

For my parents, Jeffrey and Donna Hoh.

Acknowledgments

First of all, many thanks are in order for my advisor Professor John Brady, who has maintained much more confidence in my abilities throughout my time at Caltech than I have. John has a keen eye for both style and substance, and I have always been impressed by his expertise with finding and developing interesting problems to tackle. If his skills have rubbed off, even ever so slightly on me, then I should consider myself lucky. My committee members, too, have been supportive in the process. Thank you to Professor Zhen-Gang Wang for having faith in me from my candidacy exam through to the end, and thank you to Professors Julie Kornfield and José Andrade for volunteering as enthusiastic additions to my thesis committee.

I am indebted to all the Brady group members, however briefly we may have crossed paths in the subbasement. They have helped to shape my understanding of fundamental concepts, to hone my programming and presentation skills, even to adjust my persistently pessimistic attitude. Thank you to graduate students Jim Swan, Manuj Swaroop, Charlie Slominski, Phares Carroll, Shaun Swanson, Mu Wang, Wen Yan, Kevin Marshall, Sho Takatori, and Isaac Fees, to postdocs Ashley Smart and Sergey Shklyaev, to visiting faculty George Petekidis, Anugrah Singh, Jim Gilchrist, and Andy Kraynik, and to visiting students Nick Koumakis and Marlon Ebert. I would like to single out a few Brady group members who went above and beyond what is expected of a colleague, to whom I am truly grateful: first and foremost, Roseanna Zia was an exemplary mentor during my first two years in the group and I look forward to working more with her in the future. Greg Rubinstein was my first undergraduate researcher and played an instrumental role in our work on hydrodynamic interactions impacting the motion of catalytic nanomotors and diffusiophoretic motion. Lastly, much of what I know of Brownian Dynamics as a simulation tool was learned through working with a diligent SURF student, Christian Aponte Rivera.

My passions truly lie in the realm of the classroom, so I am thankful that John permitted me to spend some of my time at Caltech honing my craft as a TA. I would like to thank the students of the classes ChE 103ab during the 2009-2010 school year, and ChE 151ab during the 2010-2011 school year, for being such receptive audiences. Their enthusiasm and dedication was infectious, and I look back on my time in front of whiteboards and blackboards as some of the most memorable moments in Spalding. Thanks are also in order to the lecturers of these courses, Professors Julie Kornfield and

John Brady, for offering up freedom to lead recitations. Also, the Chemical Engineering staff has always been eager to assist me, whether with room and projector reservations, computer troubles, or with something as simple as a smile and friendly "hello." Special thanks are in order for Kathy Bubash and Suresh Guptha.

A supportive network of friends carried me through difficult times, and I cannot possibly thank everyone by name lest I forget someone or end up with an acknowledgements section longer than the body of my thesis. My roommates throughout most of my time here in Pasadena, Matt Smith and JD Bagert have provided me with many fond memories both in and out of the "MadHouse." I am also thankful for the many friends I have made through Caltech PRISM; country line dancing and game nights were great stress relievers. To my fellow first year ChEs entering in fall 2008, thank you for the camaraderie throughout our classwork.

Relying on my family has been instrumental throughout the process of working toward a PhD. I can recall many times feeling so distraught and overwhelmed here, and a phone call with my mom, my most supportive cheerleader, would always improve my outlook. Thank you to my parents, Jeffrey and Donna, and to my sisters Christina and Lindsay. I love you all so much and look forward to seeing you all much more soon. Lastly, I am indebted to my boyfriend and partner of nearly four years, Andreas Hoenselaar. His selflessness knows no bounds, especially during the trying times of thesis writing. My accomplishments at Caltech belong to him as much as to me, as he is always eager to help me succeed. Ich liebe Dich von ganzem Herzen!

Abstract

The motion of a single Brownian particle of arbitrary size a through a dilute colloidal dispersion of neutrally buoyant "bath" spheres of another characteristic size $b \equiv \lambda a$ in a Newtonian solvent is examined in two contexts. First, the particle in question, the "probe" particle, is subject to a constant applied external force drawing it through the suspension as a simple model for active and nonlinear microrheology. The strength of the applied external force, normalized by the restoring forces of Brownian motion, is the Péclet number Pe. This dimensionless quantity describes how strongly the probe is upsetting the equilibrium distribution of the bath particles. The mean motion and fluctuations in the probe position are related to interpreted quantities of an effective viscosity of the suspension. These interpreted quantities are calculated to first order in the volume fraction ϕ_b of bath particles and are intimately tied to the spatial distribution, or microstructure, of bath particles relative to the probe. For weak Pe, the disturbance to the equilibrium microstructure is dipolar in nature, with accumulation and depletion regions on the front and rear faces of the probe, respectively. With increasing applied force, the accumulation region compresses to form a thin boundary layer whose thickness scales with the inverse of Pe. The depletion region lengthens to form a trailing wake. The magnitude of the microstructural disturbance is found to grow with increasing bath particle size – small bath particles in the solvent resemble a continuum with effective microviscosity given by Einstein's viscosity correction for a dilute dispersion of spheres. Large bath particles readily advect toward the minimum approach distance possible between the probe and bath particle, and the probe and bath particle pair rotating as a doublet is the primary mechanism by which the probe particle is able to move past; this is a process that slows the motion of the probe by a factor of λ^{-1}. The intrinsic microviscosity is found to force thin at low Péclet number due to decreasing contributions from Brownian motion, and force thicken at high Péclet number due to the increasing influence of the configuration-averaged reduction in the probe's hydrodynamic self mobility. Nonmonotonicity at finite sizes is evident in the limiting high-Pe intrinsic microviscosity plateau as a function of bath-to-probe particle size ratio. The intrinsic microviscosity is found to grow as λ for very small probes even at large-but-finite Péclet numbers, but even a small repulsive interparticle potential, that excludes lubrication interactions, can reduce this intrinsic microviscosity from $O(\lambda)$ to $O(1)$. The results of this active microrheology study are compared to previous theoretical studies of falling-ball and

towed-ball rheometry and sedimentation and diffusion in polydisperse suspensions, and discrepancies in the problem statements and their implications are noted.

Second, the probe particle in question is no longer subject to a constant applied external force. Rather, the particle is considered to be a catalytically-active "motor", consuming the bath reactant particles on its reactive face while passively colliding with reactant particles on its inert face. By creating an asymmetric distribution of reactant about its surface, the motor is able to diffusiophoretically propel itself with some mean velocity. The effects of finite size of the solute are examined on the leading order diffusive microstructure of reactant about the motor. Brownian and interparticle contributions to the motor velocity are computed for several interparticle interaction potential lengths and finite reactant-to-motor particle size ratios, with the dimensionless motor velocity increasing with decreasing motor size. A discussion on Brownian rotation frames the context in which these results could be applicable, and future directions are proposed which properly incorporate reactant advection at high motor velocities.

Contents

List of Figures

Chapter 1

Introduction

Complex fluids have microstructural features of various length scales that can be used to achieve certain effects. The glittery finish of some nail polishes and lacquers, and the iridescent look of certain automotive paints are the results of colloidal particles of nanometer to micrometer size. The yield stress of shaving cream allows for a layer on the order of millimeters to stay put on the skin when shaving. Hydrogels create a volume-spanning network of structure up to macroscopic lengths. Suppose you have a tool to interrogate one of these complex materials, and the tool itself has a certain length scale. For example, the company RheoSense offers a Viscometer/Rheometer on a Chip (VROC) comprising pressure sensors along a microfluidic channel of a width of a few millimeters and a depth on the order of 10-100 microns. It is important to understand how certain microstructural features within the sample of complex fluid can interact with an interrogating device and change the resulting measurement. A biological solution of 100kbp DNA fragments, and paint with suspended micron-sized particulates both have microstructural features that could affect the readout of the VROC. In this thesis, one objective is to present a careful analysis of one measurement technique, active and nonlinear microrheology, and the implications that come with microstructural features of a wide range of sizes.

This work examines the motion of a single "probe" particle through a colloidal dispersion when that particle is of some arbitrary size compared to the particles of the suspension. First, in Chapter 2, the probe particle is driven by an externally imposed force that is independent from the forces arising from solvent-particle and particle-particle interactions. One can interpret the mean motion and fluctuations of this colloidal probe in terms of a perceived microviscosity and effective diffusivity. Initially, this external force is analyzed when it is much weaker than the restoring forces of Brownian motion. This is termed the "linear response" regime because the leading-order disturbance to the equilibrium microstructure will be linear in the strength of the applied external force. Owing to the first nonlinear perturbation, the microviscosity force thins proportional to the square of the Péclet number, a dimensionless quantity relating the strength of the applied external force to the restoring forces of Brownian motion. The extent of force thinning is due to a competition between

hydrodynamic and Brownian forces, which exhibit some interesting nonmonotonicity with respect to both the length of the range of interparticle interactions and the bath-to-probe particle size ratio.

Next, the strength of the applied external force is no longer constrained to be small. When thermal motion of the dispersed particles is weak or even absent, at high Péclet number, force thickening behavior may be observed depending on how long-ranged the interparticle interactions between the probe and bath particles are, and the limiting value for the intrinsic microviscosity is found to vary nonmonotonically with the bath-to-probe particle size ratio. This high-Péclet microviscosity is strictly hydrodynamic, and not Brownian, in nature. Lubrication interactions are most important for determining the high-Péclet microviscosity for small probe particles, while long-ranged hydrodynamic interactions shape the microviscosity for large probes. A boundary-layer analysis yields consistent findings with the falling-ball theory developed by Davis and Hill [16] and Almog and Brenner [1]. Comparisons are made to the quintessential works of Batchelor [5, 7, 6], and Batchelor & Wen [8], on sedimentation and diffusion in a polydisperse suspension. The distinctions between the way the active microrheology and sedimentation problems have been posed are highlighted. A discussion of physical mechanisms for probe-bath collision resolution is also presented.

Lastly, in Chapter 3, particle size is discussed through the lens of autonomous motion. Hydrodynamic interactions between a catalytic nanomotor particle and the reactant species are added to the osmotic propulsion model employed by Córdova-Figueroa and Brady [13, 14]. In these works, solute reactant molecules are treated as colloidal species dispersed throughout a Newtonian, viscous, constant property solvent. Some concerns, from a continuum-level analysis, arose over whether motion can arise from local solute gradients [26, 27], but the colloidal-level treatment of solute matches the continuum-level analysis in the appropriate limits as shown by Brady [10]. The purpose of this chapter is to explore concepts proposed in the autonomous motion section of Brady's work on particle motion driven by solute gradients. In particular, if the reactant and product species are thought of as colloidal particles dispersed throughout a continuum solvent, the velocity field created by the motion of the motor should alter the trajectories of reactant and product past the motor. We start by highlighting key features of the autonomous motion problem statement in section 3.2 for colloidal solute reactant particles that interact hydrodynamically with the motor particle. For a detailed introduction to the problem at hand, the curious reader is referred to sections 4 and 5 of the work of Brady [10].

Chapter 2

Active and Nonlinear Microrheology in Polydisperse Systems

2.1 Introduction

Fluids behaving in an unexpected manner are bound to pique the curiosity of a rheologist. For example, finger-like structures appear to crawl from a cornstarch and water mixture vibrated on a speaker cone. Also, non-Newtonian fluids climb up a spinning rod due to normal stress differences and the Weissenberg effect. The rheology community has several methods at its disposal to interrogate complex fluids in a systematic manner to recover quantitative measures of the matter's response to deformation. Traditional rheometric techniques may apply a bulk viscometric flow to the material, *i.e.* a deformation that is a superposition of rigid-body motion and simple shearing motion. The relationships between stress and strain can be interpreted as viscous and elastic moduli: quantities that describe how energy is dissipated and stored, respectively, by the material. Small amplitude oscillatory shear tests may be used to determine the linear viscoelastic response of matter, but these alone may not be sufficient to describe the behavior of the complex fluid for all processing scenarios. In fact, two fluids that behave identically in the linear response regime may exhibit very different nonlinear behavior. Large amplitude oscillatory shear (LAOS) allows for the nonlinear regime to be tested on the scale of macroscopic deformations and systematically determine the responses of matter to varying amplitude and frequency. Although nonlinear 'macro'rheological techniques are not the focus of this work, the reader is referred to the review by Hyun *et al* [23] for the state of the art on LAOS.

Scenarios abound in which macrorheological techniques may not be a viable option. These scenarios include quantifying the viscoelastic response of microscopically confined systems like the cell cytoplasm, measuring samples of a scarce volume, probing the local character of a heterogeneous sample, and designing high-throughput measurement techniques. For these purposes, 'micro'rheological techniques, in which one or more tracer or 'probe' particles are embedded in a sample and then

observed, are proving to be effective methods to solve the aforementioned concerns. Probes move about due to thermal fluctuations and Brownian motion arising from collisions between the probe and its surrounding environment. When thermal motion drives the probes, the technique is known as passive microrheology. The positions of the tracer particles are observed and recorded using one of many established techniques: video particle-tracking microscopy, diffusing wave spectroscopy, dynamic light scattering, *etc.* Once the probes' trajectories are known, the mean-squared displacements can be related by the fluctuation-dissipation theorem to the hydrodynamic resistance of the local environment. The local resistance can be interpreted as an effective material property, such as a local storage or loss modulus or an effective 'micro'viscosity. For a walkthrough of the steps from observing colloidal probes to interpreting local and bulk rheological properties, the review by Squires and Mason [50] is particularly lucid and detailed.

Passive microrheology has several applications where it may be particularly utile. One of the proposed advantages is that the sample size required to characterize the viscoelastic properties is much smaller than with traditional bulk rheological techniques. High-throughput microrheology, using multiple particle tracking in a series of droplets, is feasible in microfluidic devices due to the minimal sample volumes required and the rapid screening time [47]. Additionally, the number of rheological measurements of a scarce complex fluid, such as certain biomaterials, can be maximized by conducting measurements on milligram quantities of sample [46]. The notion that microrheology can probe multiple microstructural features at equilibrium across different length scales has been employed by experimentalists. Liu *et al* [35] probed the mechanical properties of entangled solutions of F-actin over two decades of length scales. They conducted their experiments with F-actin filaments ranging from 1 to 100 μm in average contour length, using both one and two-particle passive microrheology techniques over 5 decades of frequency. From bulk rheological measurements, F-actin solutions exhibit a transition regime at intermediate frequencies that microrheology was also able to successfully investigate. Two-particle microrheology, or two-point microrheology, involves cross-correlation of the motion of multiple tracer or probe particles, and avoids some of the problems that befall single-probe passive microrheology experiments, such as the probe exhibiting a heightened mobility by inhabiting a cavity within a porous medium or creating its own cavity via steric hindrance [15].

The aforementioned passive microrheology experiments rely on thermal energy, causing collisions between the probe and its environment, to disturb the probes. With these experiments the measurement of linear viscoelastic moduli is possible, but as we mentioned before for bulk rheological techniques, this only allows for an equilibrium view of the material. In order to interrogate the non-equilibrium behavior of a material, active and nonlinear microrheology has been proposed. By applying an external force to the probe whose strength is independent of the thermal energy of the material, one can drive the microstructure of the complex fluid out of equilibrium, and a nonlinear

response is probed. One example of active and nonlinear microrheology that may come to mind is falling-ball rheometry; although it is a technique often practiced on length scales much larger than the micron-size environments proposed for microrheology. Theoretical and experimental concerns for falling-ball rheometry in colloidal dispersions have included the finite size of the background colloidal elements, the bounded versus unbounded nature of the sedimentation environment *e.g.* how cylindrical walls affect falling-ball rheometry [11], and constant-force versus constant-velocity rheometry achieved by sedimentation and "towing", respectively [44]. Another method of applying an external force to one or more colloidal probe particles include focusing lasers to create an optical trap for a particle situated in a dispersion where all other colloidal species are index matched to the suspending solvent [52, 51].

These experimental and theoretical studies lead us to discuss a common system used in the analysis of active and nonlinear microrheology: colloidal dispersions. Colloidal dispersions are a quintessential model for a complex fluid. Hard-sphere colloidal dispersions exhibit rheopectic and thixotropic behavior; on the macroscale, hard-sphere suspensions are known to initially shear thin with increasing strength of applied stress; this is owed to a decreasing Brownian stress [9]. Under even stronger applied stresses, colloidal dispersions exhibit rheopectic behavior that can arise due to hydroclusters forming a percolating network and jamming [36]. Theoretical and computational studies of active or nonlinear microrheology have used the model system of one or more colloidal probe particles situated amongst background bath particles; Brownian dynamics simulations allow for probe particles to be forced through a collection of hard-sphere colloids either at a fixed force or fixed velocity, and the mean motion and fluctuations can be interpreted as a microviscosity and effective diffusivity [12, 60, 61]. Time dependent microstructural features have been examined, whether from an oscillatory applied force [28], or from startup or cessation of probe particle motion through a quiescent dispersion [62]. Dilute theory analyses allow for analytical considerations of the steady bath microstructure about the probe particle with full hydrodynamic interactions [29]; however, some questions remain. As mentioned earlier in the discussion of experiments probing F-actin solutions, passive microrheology allows for the equilibrium mechanical response to be observed over decades of length scale. Is the same possible for active microrheology? If so, the *non*-equilibrium mechanical response can be probed over a range of microstructural feature sizes. Certainly probes of all sizes, great and small, can be embedded in a sample. Dragging each of these probes through a suspension merits a careful analysis of how their sizes influence the disturbances created to the surrounding complex fluid. How much larger does a probe need to be than the surrounding bath particles before the entire suspension resembles a continuum? In such a limit, we expect to recover Einstein's viscosity correction $\eta^{\text{eff}}/\eta_0 = 1 + \frac{5}{2}\phi$. For what probe sizes do lubrication effects contribute most to the perceived microviscosity? What about probe sizes affected most by long-ranged hydrodynamic interactions? For probes identical in size to the suspension constituents, force-thinning at low Péclet

numbers and force-thickening at high Péclet numbers are predicted, in line with the shear-thinning and shear-thickening behavior exhibited in macroscopically sheared colloidal dispersions. Is this feature of force thinning followed by force thickening with increasing Péclet number universal for all probe sizes? What connections can be made between active microrheology of arbitrary probe sizes and sedimentation studies of polydisperse dispersions?

The remainder of the chapter attempts to answer some of these questions, and is laid out as follows: in Section 2.2 the model system for constant force active microrheology in dilute colloidal systems is established. This requires a brief review of two-body hydrodynamic interactions, and we attempt to adhere to notation conventions from the sedimentation literature. In Section 2.3, the constant force applied to the probe particle is considered when it is much weaker than the thermal energy of the solvent, corresponding to a small Péclet number. In the limit where the Péclet number approaches zero, we should recover the linear viscoelastic properties as one would for passive microrheology experiments. The contributions to the intrinsic microviscosity and effective diffusivity shift from purely hydrodynamic in nature for large probes, to Brownian contributions dependent on lubrication interactions for small probes. In Section 2.4, the $O\left(\mathrm{Pe}^2\right)$ disturbance to the equilibrium microstructure and its impact on the intrinsic hydrodynamic microviscosity are discussed. Nonmonotonic behavior, with respect to the bath-to-probe particle size ratio and with respect to the interparticle interaction potential, are noted.

Section 2.5 covers the numerical techniques necessary to compute the suspension microstructure at arbitrary Péclet numbers. When the Péclet number is not too large, a finite series of angular moments of the microstructure weighted by radial functions are used to approximate the probability distribution of bath particles about the probe. This Legendre polynomial solution method is motivated as an extension of the low-Pe perturbation expansions of the previous section. For larger Péclet numbers, many moments are required to capture the complex microstructural features of a thin accumulation region on the anterior face of the probe and a wake of probability deficit coalescing behind the probe. It is more computationally tractable to solve for the microstructure at larger Péclet number using a second-order finite difference scheme that concentrates grid points in the boundary layer to capture the large microstructural gradients present.

Analytic techniques for computing the infinite-Péclet suspension microstructure are presented in section 2.6. The purely advective solution to the microstructure for non-Brownian systems is shown to be spherically symmetric. Techniques are presented that were originally proposed by Almog and Brenner [1] to write the pair distribution function in terms of the far-field multipole expansion coefficients of the hydrodynamic mobility functions given by Jeffrey and Onishi [25]. The advection solution for the microstructure does not satisfy the condition of no relative flux through the surface of the probe particle, and so a singular perturbation expansion is needed, which matches the outer advective problem to a boundary-layer solution, in which radial diffusion is comparable in magnitude

to advection. The applicability of the boundary-layer solution for finite size ratios is put into question by examining the boundary layer thickness as a function of angular distance from the line of forcing, and for small probes, this boundary layer thickness diverges at the midpoint between the anterior and posterior probe faces, long before the coalescence region of probability density in the trailing wake opposite the direction of forcing. Lastly, the suspension microstructures and intrinsic microviscosity results for the range of Pe and λ are shown in Section 2.7. Methods to interpret microstructures across different size ratios and different Péclet numbers require consideration of what quantities stay fixed at constant Pe versus at constant Pe/λ, and these considerations are addressed. A continuation of this study, to determine the nonlinear effects on the effective diffusivity, is proposed.

2.2 Model system

Consider a collection of $(N-1)$ rigid, spherical, neutrally-buoyant particles of radii b dispersed homogeneously throughout a Newtonian, viscous solvent of density ρ and dynamic viscosity η. Another rigid, spherical particle of radius a, which we will refer to as the "probe" particle, is situated among these "bath" particles. An external force $\mathbf{F}_1^{\text{ext}}$, which may arise from a solvent-probe particle density difference or from optical/magnetic tweezers, drags the probe particle through the suspension. In this analysis, the applied external force is presumed constant. This is in contrast to constant-velocity microrheology where the probe velocity is prescribed, and fluctuations of the position are disallowed. The crux of the fixed force microrheology problem is to determine the mean translational motion of the probe particle in response to the applied force. In addition, the modified diffusivity of the probe particle in response to the applied force can be determined by analyzing the fluctuations in the probe particle position. Both of these quantities, the mean motion and fluctuations of the probe, are intimately tied to the spatiotemporal arrangement of the bath particles about the probe. We begin by determining the probability fluxes of probe and bath particles. These fluxes will ultimately provide insight into the likelihood of each configuration. Once the probability of each configuration is known, weighted averages of the probe flux over all possible configurations will yield expressions for the mean motion and diffusivity. The particles are small enough and the probe translates slowly enough, with some characteristic velocity U, such that the Reynolds number characterizing the ratio of inertial to viscous effects, $\text{Re} \equiv \rho U a/\eta$ is much less than unity. The Stokes equations of motion accurately capture the fluid physics. In this regime, the velocity of any one particle is linear in the forces acting on each particle in the suspension. In addition to the constant external force, the probe and bath particles may interact with one another via some interparticle interactive force $\mathbf{F}^P$. For micron-sized and smaller particles, the collisions between solvent molecules and particles are significant enough that the Brownian force $\mathbf{F}^B$ is non-negligible. Following previously set-forth methodology in several works ([39], [49], [29], and [60]), diluteness of the dispersion is assumed in

order to investigate the probe behavior in the presence of a single bath particle. The probe-and-bath geometry in one realization is visualized in Figure 2.1. The velocity of the probe or bath particle is given by:

$$\mathbf{U}_\alpha = \mathbf{M}^{UF}_{\alpha 1} \cdot \left(\mathbf{F}^{\text{ext}}_1 + \mathbf{F}^P_1 + \mathbf{F}^B_1\right) + \mathbf{M}^{UF}_{\alpha 2} \cdot \left(\mathbf{F}^P_2 + \mathbf{F}^B_2\right), \tag{2.1}$$

where $\mathbf{M}^{UF}_{\alpha\beta}$ is the two-sphere translational mobility tensor coupling the forces acting on particle β with the resulting velocity of particle α. The indices α and β can each take on the values 1 or 2 to signify the probe or bath particle, respectively. For a two-sphere geometry, it is useful to change to a frame of reference moving with the probe particle. Let $\mathbf{x}_1$ and $\mathbf{x}_2$ denote the centers of the probe and bath particles, respectively. The preferred coordinates moving with the probe particle are $\mathbf{z} \equiv \mathbf{x}_1$ and $\mathbf{r} \equiv \mathbf{x}_2 - \mathbf{x}_1$. The scalar separation distance between the probe and bath particle centers is r, defined as the magnitude of the center-to-center separation vector $\mathbf{r}$. In a two-sphere geometry, the mobility tensors take on the form:

$$\mathbf{M}^{UF}_{\alpha\beta}(\mathbf{r}) \equiv \frac{1}{3\pi\eta\left(a_\alpha + a_\beta\right)} \left[x^A_{\alpha\beta}(s,\lambda)\,\mathbf{nn} + y^A_{\alpha\beta}(s,\lambda)\left(\mathbf{I} - \mathbf{nn}\right)\right]. \tag{2.2}$$

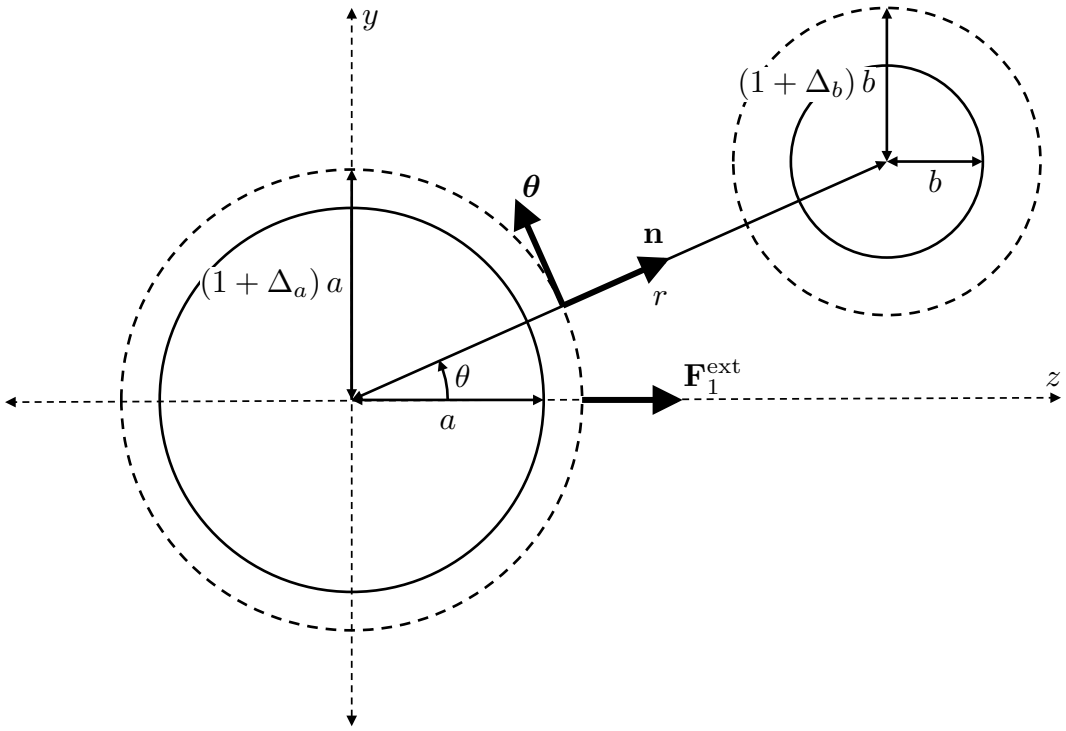

Figure 2.1: Geometry for analysis of the dilute microrheology problem.

Here, the vector $\mathbf{n} \equiv \mathbf{r}/r$ is the unit normal pointing outward from the probe particle parallel to the line-of-centers, and $\mathbf{I}$ is the second-order identity tensor. In Equation 2.2, we have followed

the lead of Batchelor [5] and introduced two dimensionless quantities which fully characterize the geometry of the two-sphere system: first, the dimensionless center-to-center separation distance $s \equiv 2r/(a+b)$ based on the hydrodynamic radii of the particles, and second, the bath-to-probe particle radii size ratio $\lambda \equiv b/a$. The scalar mobility functions $x^A_{\alpha\beta}$ and $y^A_{\alpha\beta}$ denote how readily particle α will translate in response to a force on particle β parallel to and perpendicular to the line-of-centers, respectively. In the literature, particularly for work discussing hydrodynamics in systems that are free of external torques and other higher moments of force, the functions $x^A_{\alpha\beta}$ and $y^A_{\alpha\beta}$ are sometimes more compactly referred to as $A_{\alpha\beta}$ and $B_{\alpha\beta}$. Note that the mobility tensor has no dependence on the absolute location $\mathbf{z}$ of the configuration in space, only the relative separation vector $\mathbf{r}$ of the probe and bath particle is relevant.

The interparticle force $\mathbf{F}^P_\alpha$ is derivable from a scalar potential field Φ and is made dimensionless by the thermal energy kT. The choice of interparticle potential in this analysis is the excluded annulus, frequently applied in theoretical models [45] as simple short-ranged repulsions beyond hard-sphere interactions. This potential fixes a minimum approach distance $r_{\min}$ between the probe and bath particle centers:

$$\Phi\left(\mathbf{z}, \mathbf{r}\ ;\ t\right) \equiv \begin{cases} \infty, & r < r_{\min}, \\ 0, & r > r_{\min}. \end{cases} \tag{2.3}$$

Note that the minimum approach distance $r_{\min}$ for rigid, spherical particles is at least as large as the sum of the hydrodynamic radii of the probe and the bath particle $a+b$. The value of $r_{\min}$ can be adjusted to "tune" the strength of the hydrodynamic interactions in the model, approaching full incorporation of hydrodynamic interactions as $r_{\min}$ approaches $a+b$. The interparticle force on particle α, resulting from Φ, may thus be written as the gradient of the interparticle potential

$$\mathbf{F}^P_\alpha \equiv -kT\nabla_\alpha \Phi\left(\mathbf{z}, \mathbf{r}\ ;\ t\right). \tag{2.4}$$

The operator ∇_α represents a gradient with respect to the absolute spatial coordinate $\mathbf{x}_\alpha$, *i.e.* $(\partial/\partial\mathbf{x}_\alpha)$.

As shown by Batchelor [4], the Brownian force may be interpreted as if a steady force equal and opposite to the interparticle force acts on each particle. That is to say, for a configuration of N particles, the relative diffusive flux of particle α due to Brownian motion is as if the steady force

$$\mathbf{F}^B_\alpha \equiv -kT\nabla_\alpha \ln P_N\left(\mathbf{x}_1,\ \cdots,\ \mathbf{x}_N\ ;\ t\right) \tag{2.5}$$

were acting on particle α. Note that $P_N\left(\mathbf{x}_1,\ \cdots,\ \mathbf{x}_N\ ;\ t\right)$ is the joint probability distribution of the position vectors of all N particle centers at time t. For dilute systems, we integrate out the positions of $N-2$ of the bath particle centers. This leaves only the pair probability density function

$P(\mathbf{x}_1, \mathbf{x}_2\ ;\ t)$, which describes the likelihood of a configuration with the probe particle centered at $\mathbf{x}_1$ and a bath particle centered at $\mathbf{x}_2$ simultaneously at time t. In terms of the relative coordinates, the probability density function $P_2(\mathbf{z},\ \mathbf{r}\ ;\ t)$ describes the likelihood of the probe particle residing at $\mathbf{z}$ while a bath particle is situated at some location $\mathbf{r}$ from the probe.

Solving in a frame of reference translating with the probe necessitates the conversion of gradients in terms of the absolute coordinates $\mathbf{x}_1$ and $\mathbf{x}_2$ into gradients in terms of the relative coordinates $\mathbf{z}$ and $\mathbf{r}$. Thus $\nabla_1 = +\nabla_{\mathbf{z}} - \nabla_{\mathbf{r}}$ and $\nabla_2 = +\nabla_{\mathbf{r}}$. Applying the expressions for the interparticle and Brownian force from Equations 2.4 and 2.5 into Equation 2.1, the velocity of particle $\beta = 1, 2$, in a given configuration $\{\mathbf{z},\ \mathbf{r}\}$ of probe and bath particle is given by the expression

$$\mathbf{U}_\beta = \mathbf{M}^{UF}_{\beta 1} \cdot \mathbf{F}^{\text{ext}}_1 + kT\left(\mathbf{M}^{UF}_{\beta 1} - \mathbf{M}^{UF}_{\beta 2}\right) \cdot \nabla_{\mathbf{r}} \ln P_2(\mathbf{z}, \mathbf{r}\ ;\ t) - kT\mathbf{M}^{UF}_{\beta 1} \cdot \nabla_{\mathbf{z}} \ln P_2(\mathbf{z}, \mathbf{r}\ ;\ t). \quad (2.6)$$

Gradients of the excluded-annulus potential Φ as defined in equation 2.3 are identically zero for all accessible configurations, and hence $\nabla_{\mathbf{r}}\Phi$ does not explicitly appear in equation 2.6. This velocity expression is valid only for configurations in which $r > r_{\min}$; assemblages with smaller radial separations than $r_{\min}$ are disallowed by the excluded-annulus potential. The probability flux $\mathbf{j}_\beta$ of particle β is the product of the configuration-dependent particle velocity with the pair-probability density of that configuration

$$\begin{aligned}
\mathbf{j}_\beta &\equiv \mathbf{U}_\beta P_2(\mathbf{z}, \mathbf{r}\ ;\ t) \\
&= \mathbf{M}^{UF}_{\beta 1} \cdot \mathbf{F}^{\text{ext}}_1 P_2(\mathbf{z}, \mathbf{r}\ ;\ t) \\
&\quad + kT\left(\mathbf{M}^{UF}_{\beta 1} - \mathbf{M}^{UF}_{\beta 2}\right) \cdot \nabla_{\mathbf{r}} P_2(\mathbf{z}, \mathbf{r}\ ;\ t) \\
&\quad - kT\mathbf{M}^{UF}_{\beta 1} \cdot \nabla_{\mathbf{z}} P_2(\mathbf{z}, \mathbf{r}\ ;\ t). \qquad (2.7)
\end{aligned}$$

The volume of the dispersion is presumed to be so large that the confinement effects arising from any boundaries are negligible and the suspension is essentially unbounded. As described by Zia and Brady [60], Fourier space is well-suited for such an infinite domain, and will allow for the determination of the long-time self-diffusivity of the probe. The Fourier transform, denoted by the hat symbol $\hat{}$, is performed with respect to the location of the probe particle center $\mathbf{z}$

$$\hat{f}(\mathbf{k},\ \mathbf{r}) \equiv \int_{\text{all } \mathbf{z}} f(\mathbf{z},\ \mathbf{r}) \exp(-i\mathbf{k} \cdot \mathbf{z})\ d\mathbf{z}. \quad (2.8)$$

The Fourier-transformed probability flux may be written as

$$\hat{\mathbf{j}}_\beta = \mathbf{M}^{UF}_{\beta 1} \cdot \mathbf{F}^{\text{ext}}_1 \hat{P}_2(\mathbf{k}, \mathbf{r}\ ;\ t) + kT\left(\mathbf{M}^{UF}_{\beta 1} - \mathbf{M}^{UF}_{\beta 2}\right) \cdot \nabla_{\mathbf{r}} \hat{P}_2(\mathbf{k}, \mathbf{r}\ ;\ t) - i\ kT\mathbf{M}^{UF}_{\beta 1} \cdot \mathbf{k}\hat{P}_2(\mathbf{k}, \mathbf{r}\ ;\ t), \quad (2.9)$$

where $\mathbf{k}$ is the wavevector from the Fourier transform and $\hat{P}_2$ is the Fourier-transformed pair-

probability density. Note that in the limit of neglected hydrodynamic interactions ($r_{\min} \gg a+b$), the hydrodynamic mobility tensors $\mathbf{M}_{11}^{UF}$, $\mathbf{M}_{22}^{UF}$, and $\mathbf{M}_{12}^{UF}$ approach $(6\pi\eta a)^{-1}\mathbf{I}$, $(6\pi\eta b)^{-1}\mathbf{I}$ and $\mathbf{0}$, respectively, resulting in the simple forms for the Fourier-transformed probability fluxes of the probe and bath particles

$$\hat{\mathbf{j}}_{1,\text{ No HI}} = (\mathbf{U}_a - i\ D_a\mathbf{k})\,\hat{P}_2 + D_a\nabla_{\mathbf{r}}\hat{P}_2, \tag{2.10}$$

and

$$\hat{\mathbf{j}}_{2,\text{ No HI}} = -D_b\nabla_{\mathbf{r}}\hat{P}_2. \tag{2.11}$$

The term $\mathbf{U}_a = \mathbf{F}_1^{\text{ext}}/(6\pi\eta a)$ represents the translational velocity of the probe particle through the solvent due to the applied external force in the absence of probe-bath interactions. The terms D_a and D_b represent the self-diffusivities of the probe and bath particle in pure solvent, $kT/6\pi\eta a$ and $kT/6\pi\eta b$, respectively. When assessing the problem with hydrodynamic interactions, though, it is useful to introduce certain combinations of the dimensionless scalar mobility functions. Batchelor introduced combinations of these functions for analyzing sedimentation in polydisperse systems [5]. First, we use two combinations L and M that describe relative motion between the probe and bath particle. The motion described by L and M arises from an applied external force. Relative motion along the line-of-centers is given by L while relative motion perpendicular to the line-of-centers is given by M. These functions are

$$L(s,\lambda) \equiv x_{11}^A(s,\lambda) - \frac{2}{1+\lambda}x_{12}^A(s,\lambda), \tag{2.12}$$

and

$$M(s,\lambda) \equiv y_{11}^A(s,\lambda) - \frac{2}{1+\lambda}y_{12}^A(s,\lambda). \tag{2.13}$$

The dimensionless hydrodynamic functions $x_{\alpha\beta}^A$ and $y_{\alpha\beta}^A$ were introduced in Equation 2.2. Next, we use the two scalar combinations G and H that arise in the Brownian diffusivity tensor $\mathbf{D}_r \equiv \mathbf{D}_{22} - \mathbf{D}_{21} - \mathbf{D}_{12} + \mathbf{D}_{11}$. These functions describe the hydrodynamics of diffusive motion parallel and perpendicular to the line-of-centers, respectively:

$$G(s,\lambda) \equiv \frac{\lambda x_{11}^A(s,\lambda) + x_{22}^A(s,\lambda)}{1+\lambda} - \frac{4\lambda}{(1+\lambda)^2}x_{12}^A(s,\lambda), \tag{2.14}$$

$$H(s,\lambda) \equiv \frac{\lambda y_{11}^A(s,\lambda) + y_{22}^A(s,\lambda)}{1+\lambda} - \frac{4\lambda}{(1+\lambda)^2}y_{12}^A(s,\lambda). \tag{2.15}$$

Note that for same-sized particles ($\lambda = 1$), the functions L and G are equivalent, as are the quantities M and H. All four of these hydrodynamic functions approach unity at infinite separations, and are monotonically increasing functions of the dimensionless particle center-to-center separation distance s. For the sake of compactness in the ensuing derivation, we define the following dimen-

sionless tensors: the configuration-dependent probe particle self-mobility tensor $\hat{\mathbf{M}}_{11}$, the relative mobility tensor $\hat{\mathbf{M}}_r$ arising from an applied external force on the probe, and the relative Brownian diffusivity tensor $\hat{\mathbf{D}}_r$:

$$\hat{\mathbf{M}}_{11} \equiv \mathbf{M}_{11}^{UF} / \left(\frac{1}{6\pi\eta a} \right) = x_{11}^{A} \mathbf{nn} + y_{11}^{A} \left(\mathbf{I} - \mathbf{nn} \right), \tag{2.16}$$

$$\hat{\mathbf{M}}_r \equiv \left(\mathbf{M}_{11}^{UF} - \mathbf{M}_{12}^{UF} \right) / \left(\frac{1}{6\pi\eta a} \right) = L\mathbf{nn} + M \left(\mathbf{I} - \mathbf{nn} \right), \tag{2.17}$$

$$\hat{\mathbf{D}}_r \equiv \mathbf{D}_r / \left(D_a + D_b \right) = G\mathbf{nn} + H \left(\mathbf{I} - \mathbf{nn} \right). \tag{2.18}$$

It would behoove the reader to note that the hats in Equations 2.16, 2.17, and 2.18 do not represent Fourier-transformed quantities but rather dimensionless tensors. The quantitative and qualitative variance in suspension microstructures about probes of variable sizes can be attributed to the aforementioned hydrodynamic functions: how readily bath particles compress into a thin boundary layer on the anterior face of the probe (L) or slide past the probe (M) in response to the external force; how easily concentration gradients normal to the probe surface are dissipated (G), or how bath particles that are pushed aside by the probe migrate to fill in the trailing wake (H).

2.2.1 Ensemble-Averaged Fluxes and Interpretation as Intrinsic Microviscosity and Intrinsic Microdiffusivity

The Fourier-space representations of the probability flux of the probe particle $\hat{\mathbf{j}}_1$ and the of relative probability flux $\hat{\mathbf{j}}_2 - \hat{\mathbf{j}}_1$ in terms of these combinations of hydrodynamic functions are

$$\hat{\mathbf{j}}_1 = \hat{\mathbf{M}}_{11} \cdot \left(\mathbf{U}_a - i\mathbf{k}D_a \right) \hat{P}_2 + D_a \hat{\mathbf{M}}_r \cdot \nabla_{\mathbf{r}} \hat{P}_2, \tag{2.19}$$

and

$$\hat{\mathbf{j}}_2 - \hat{\mathbf{j}}_1 = -\hat{\mathbf{M}}_r \cdot \left(\mathbf{U}_a - i\mathbf{k}D_a \right) \hat{P}_2 - \left(D_a + D_b \right) \hat{\mathbf{D}}_r \cdot \nabla_{\mathbf{r}} \hat{P}_2. \tag{2.20}$$

These expressions for the probe and bath particle probability fluxes will be used in the Smoluchowski equation, which describes the spatiotemporal evolution of the suspension microstructure. Detailed knowledge of the suspension microstructure allows for the determination of ensemble-averaged quantities such as the effective translational velocity and effective diffusivity of the probe particle. As was done for the probability flux, the positions of $N-2$ of the bath particles are averaged out to arrive at the two-particle form of the Smoluchowski equation; which we express in terms of the relative coordinate system in Fourier space:

$$\frac{\partial \hat{P}_2}{\partial t} + \nabla_{\mathbf{r}} \cdot \left(\hat{\mathbf{j}}_2 - \hat{\mathbf{j}}_1 \right) + i\mathbf{k} \cdot \hat{\mathbf{j}}_1 = 0. \tag{2.21}$$

As in the work of Zia and Brady [60], this equation is averaged over all accessible bath particle configurations, *i.e.* for all $r \geq r_{\min}$, by integrating out the $\mathbf{r}$-dependence. This averaging determines the effective motion of the probe particle. The divergence theorem is applied to the relative probability flux term when Equation 2.21 is integrated over all $\mathbf{r}$-space. The relative flux approaches a constant value for infinitely far values of $\mathbf{r}$, and by choice of the excluded-annulus potential, the relative probability flux is zero at $r_{\min}$. Thus the second term vanishes, leaving

$$\frac{\partial \hat{P}_1}{\partial t} + i\mathbf{k} \cdot \left\langle \hat{\mathbf{j}}_1 \right\rangle = 0, \tag{2.22}$$

where the average probe flux is defined as $\left\langle \hat{\mathbf{j}}_1 \right\rangle \equiv \int_{\text{all } \mathbf{r}} \hat{\mathbf{j}}_1 \, \mathrm{d}\mathbf{r}$. Note that $\hat{P}_1 (\mathbf{k} \, ; \, t)$ is the single-particle probability density for finding the probe in Fourier space with wave vector $\mathbf{k}$ at time t. The average probe flux may be written as the sum of the probe particle flux in isolation with deviations that are hydrodynamic $\left\langle \hat{\mathbf{j}}_1^H \right\rangle$, interparticle $\left\langle \hat{\mathbf{j}}_1^P \right\rangle$, and Brownian $\left\langle \hat{\overline{\mathbf{j}}}_1^B \right\rangle$ in nature:

$$\left\langle \hat{\mathbf{j}}_1 \right\rangle = (\mathbf{U}_a - i\mathbf{k} D_a) \hat{P}_1 + \left\langle \hat{\mathbf{j}}_1^H \right\rangle + \left\langle \hat{\mathbf{j}}_1^P \right\rangle + \left\langle \hat{\overline{\mathbf{j}}}_1^B \right\rangle. \tag{2.23}$$

The expressions for these contributions to the average probe flux shall be parsed apart into velocity and diffusivity corrections later; for now, it suffices to note that all three deviations scale with the bath particle volume fraction ϕ_b. That is to say, $\left\langle \hat{\mathbf{j}}_1^H \right\rangle$, $\left\langle \hat{\mathbf{j}}_1^P \right\rangle$, and $\left\langle \hat{\overline{\mathbf{j}}}_1^B \right\rangle$ are all $O(\phi_b)$ small.

The structure function $g (\mathbf{k}, \mathbf{r} \, ; \, t)$ describes the real-space microstructure of bath particles about the probe particle. It may be thought of as a conditional likelihood of finding, at time t, a bath particle center located in real space some distance $\mathbf{r}$ from the probe particle center, given that the probe particle is described by the wave vector $\mathbf{k}$ in Fourier space. The pair-probability density $\hat{P}_2$ is defined in terms of this structure function g, along with the background number density n_b of bath particles and the single-particle probability density $\hat{P}_1$:

$$\hat{P}_2 (\mathbf{k}, \mathbf{r} \, ; \, t) = n_b g (\mathbf{k}, \mathbf{r} \, ; \, t) \hat{P}_1 (\mathbf{k} \, ; \, t). \tag{2.24}$$

For a dilute dispersion in the absence of applied external forces and interparticle interactions, the probability density of finding a bath particle anywhere in the suspension is uniform and equal to the background number density. Thus, the equilibrium form of the structure function $g_{\text{eq}} (\mathbf{k}, \mathbf{r} \, ; \, t) = 1$ for all radial separations greater than the excluded-annulus interaction distance $r_{\min}$. For the long-time self-diffusion of the probe particle undergoing steady forcing, *i.e.* the suspension microstructure has developed to a steady-state configuration, the structure function is expressed as an expansion for small values of $\mathbf{k}$:

$$g (\mathbf{k}, \mathbf{r}) = g_0 (\mathbf{r}) + i\mathbf{k} \cdot \mathbf{d} (\mathbf{r}) + \cdots \tag{2.25}$$

Note that $g_0(\mathbf{r})$ is the steady-state microstructure of bath particles in real-space about the probe particle, and $\mathbf{d}(\mathbf{r})$ is the probability-weighted displacement from a fluctuation. This expansion allows us to write the average probe flux from Equation 2.23 through $O(\mathbf{k})$:

$$\left\langle \hat{\mathbf{j}}_1 \right\rangle = \left(\left[\mathbf{U}_a + \left\langle \mathbf{U}_1^H \right\rangle + \left\langle \mathbf{U}_1^P \right\rangle + \left\langle \overline{\mathbf{U}_1^B} \right\rangle \right] - i\mathbf{k} \cdot \left[D_a \mathbf{I} + \left\langle \mathbf{D}_1^H \right\rangle + \left\langle \mathbf{D}_1^P \right\rangle + \left\langle \overline{\mathbf{D}_1^B} \right\rangle \right] \right) \hat{P}_1 + O\left(|\mathbf{k}|^2 \right). \tag{2.26}$$

The same three forces (hydrodynamic, interparticle, and Brownian) disturb both the mean $O(1)$ and fluctuating $O(\mathbf{k})$ behavior of the probe particle from its translational motion $\mathbf{U}_a$ and diffusivity $D_a\mathbf{I}$ in pure solvent. All the leading-order deviations of the probe particle from the pure solvent behavior are proportional to the background volume fraction ϕ_b of bath particles. The average velocity $\left\langle \mathbf{U}_1^H \right\rangle$ and diffusivity $\left\langle \mathbf{D}_1^H \right\rangle$ due to hydrodynamic interactions simply describe how the motion of the probe in the presence of the suspension microstructure differs from that in isolated solvent. The hydrodynamic velocity correction has one component weighted by the suspension microstructure g_0

$$\left\langle \mathbf{U}_1^H \right\rangle = n_b \int_{\text{all } \mathbf{r}} \left(\hat{\mathbf{M}}_{11} - \mathbf{I} \right) \cdot (\mathbf{U}_a)\, g_0(\mathbf{r})\ \mathrm{d}\mathbf{r}, \tag{2.27}$$

while the hydrodynamic diffusivity correction has two components, one weighted by the steady-state microstructure g_0 while the other is weighted by the deflection field $\mathbf{d}$.

$$\left\langle \mathbf{D}_1^H \right\rangle = n_b \left[D_a \int_{\text{all } \mathbf{r}} \left(\hat{\mathbf{M}}_{11} - \mathbf{I} \right) g_0(\mathbf{r})\ \mathrm{d}\mathbf{r} - \int_{\text{all } \mathbf{r}} \mathbf{d}(\mathbf{r}) \left(\hat{\mathbf{M}}_{11} - \mathbf{I} \right) \cdot \mathbf{U}_a\ \mathrm{d}\mathbf{r} \right]. \tag{2.28}$$

As expected, since the hydrodynamic velocity correction, as with the interparticle and Brownian velocity corrections, is presumed to be parallel to the applied external force, the integral in Equation 2.27 when projected onto the direction of the applied external force is equivalent to the component of the first integral in Equation 2.28, describing a contribution to the effective diffusivity for fluctuations parallel to the applied external force.

Gradients in the interparticle potential Φ are nonzero only at radial separations of $r_{\min}$. The interparticle contributions to the average velocity and diffusivity are thus given by surface integrals at the excluded-annulus boundary. For the interparticle velocity correction, we have a surface integral of the suspension microstructure at contact,

$$\left\langle \mathbf{U}_1^P \right\rangle = -D_a n_b \oint_{r=r_{\min}} g_0\ \mathbf{n} \cdot \hat{\mathbf{M}}_r\ \mathrm{d}S, \tag{2.29}$$

and for the interparticle diffusivity correction, we have a surface integral of the deflection field at contact,

$$\left\langle \mathbf{D}_1^P \right\rangle = D_a n_b \oint_{r=r_{\min}} \mathbf{d}\ \mathbf{n} \cdot \hat{\mathbf{M}}_r\ \mathrm{d}S. \tag{2.30}$$

In the limit where the excluded-annulus potential is coincident with the hydrodynamic radii of the

particles, *i.e.* $r_{\min} \to (a+b)$, due to lubrication interactions, there is no relative mobility of the probe and bath particle along the line of centers in response to a force exerted on the probe. Thus, these interparticle corrections vanish for full hydrodynamics.

Brownian motion contributes to the effective velocity and diffusivity because the probe and bath particles are unlikely to drift apart from configurations with hindered relative mobility but are likely to drift from regions of greater mobility. To compensate for the resulting probability gradient from this drift behavior, the Brownian probability flux is directed away from regions of lesser mobility as given by the divergence of the relative translational mobility tensor. The Brownian velocity correction is

$$\left\langle \overline{\mathbf{U}_1^B} \right\rangle = -D_a n_b \int_{\text{all } \mathbf{r}} g_0 \ \nabla_{\mathbf{r}} \cdot \hat{\mathbf{M}}_r \ \mathrm{d}\mathbf{r}, \tag{2.31}$$

and the average Brownian diffusivity correction is

$$\left\langle \overline{\mathbf{D}_1^B} \right\rangle = D_a n_b \int_{\text{all } \mathbf{r}} \mathbf{d} \ \nabla_{\mathbf{r}} \cdot \hat{\mathbf{M}}_r \ \mathrm{d}\mathbf{r}. \tag{2.32}$$

These ensemble-averaged velocity corrections are consistent with the results presented by Khair and Brady for monodisperse suspensions [29] and in the limit of no hydrodynamic interactions ($\Delta \to \infty$) the interparticle velocity and diffusivity corrections agree with the results presented by Squires and Brady [49] and Zia and Brady [60].

The choices of scales to render the applied external force and the radial center-to-center separation vector dimensionless are as follows:

$$\mathbf{u} \equiv \frac{\mathbf{F}_1^{\text{ext}}}{F_0} = \frac{6\pi\eta a \mathbf{U}_a}{F_0}; \quad \mathbf{s} \equiv \frac{2\mathbf{r}}{r_{\min}} = \frac{2\mathbf{r}}{(a+b)\,(1+\Delta)}, \tag{2.33}$$

where F_0 is the magnitude of the applied external force $\|\mathbf{F}_1^{\text{ext}}\|$, and the quantity Δ is the excluded-annulus parameter, which describes the difference between the interaction length of the interparticle potential and the sum of the probe and bath particle hydrodynamic radii. It is critical to note that the choice of dimensionless radial separation $\mathbf{s}$ presented in Equation 2.33 is not the same as the definition of s used in the definitions of the hydrodynamic functions $x_{\alpha\beta}^A$ and $y_{\alpha\beta}^A$. Henceforth, s will refer to the quantity defined in Equation 2.33. The excluded-annulus parameter ranges from purely excluded volume behavior $\Delta \to \infty$ to full hydrodynamic interactions $\Delta \to 0$. Note that the excluded-annulus behavior can be achieved and tuned in real systems by surface-bound polymers, electrostatic repulsion, and the addition of salts to the suspending medium. Also note that the excluded-annulus potential needs not be evenly distributed between the probe and bath particle. If $(1+\Delta_a)\,a$ and $(1+\Delta_b)\,b$ are the excluded-annulus radii of the probe and bath particles, respectively,

then the excluded annulus parameter Δ, defined in terms of these quantities, is simply

$$\Delta = \frac{\Delta_a + \lambda \Delta_b}{1+\lambda}. \tag{2.34}$$

The critical criterion for diluteness of the dispersion is that the volume fraction ϕ_b of bath particles based on their excluded volume is much less than unity, so defining a separate excluded-annulus parameter for the bath particles is useful to this end. With these dimensionless groups and parameters in mind, the average probability flux may be interpreted as:

$$\left\langle \hat{\mathbf{j}}_1 \right\rangle = \left(\frac{\mathbf{F}_1^{\text{ext}}}{6\pi\eta a} \left[1 - \eta_i \phi_b^*\right] - i\mathbf{k} D_a \cdot \left[\mathbf{I} + \mathbf{D}_i \phi_b^*\right] \right) \hat{P}_1 + O\left(|\mathbf{k}|^2\right) \tag{2.35}$$

where η_i is the intrinsic microviscosity and $\mathbf{D}_i$ is the intrinsic microdiffusivity. There are several parallels between these two intrinsic quantities. First, they represent the deviation of the mean motion and diffusive behavior of the probe particle by an $O\left(\phi_b^*\right)$ correction, where ϕ_b^* is simply the volume fraction of bath particles with radii based on the excluded-annulus parameter Δ:

$$\phi_b^* \equiv \left(\frac{1+\Delta}{1+\Delta_b} \right)^3 \phi_b = \frac{4\pi}{3} \left(1+\Delta\right)^3 b^3 n_b. \tag{2.36}$$

Second, drawing from the previous expression for the probability flux, Equation 2.26, we know that both intrinsic quantities will have hydrodynamic, interparticle, and Brownian contributions, *i.e.* $\eta_i = \eta_i^H + \eta_i^P + \eta_i^B$ and $\mathbf{D}_i = \mathbf{D}_i^H + \mathbf{D}_i^P + \mathbf{D}_i^B$. The intrinsic microviscosity η_i, as discussed by Khair and Brady [29], is an interpretation of the $O\left(\phi_b^*\right)$ hindrance to the mean motion of the probe due to the presence of bath particles in the suspension. The first term inside the parenthesis of Equation 2.35 is the mean motion $\langle \mathbf{U} \rangle$ of the probe. Substituting this expression for the mean motion into an effective Stokes drag law, *e.g.* $\mathbf{F}_1^{\text{ext}} = 6\pi\eta_{\text{eff}} a \langle \mathbf{U} \rangle$, and Taylor expanding the resulting expression for η_{eff}/η for small ϕ_b^* shows that, to leading order, the apparent viscosity of the suspension is $\eta_{\text{eff}} = \eta\left(1 + \eta_i \phi_b^*\right)$. The three contributions to the intrinsic microviscosity are the hydrodynamic contribution η_i^H:

$$\eta_i^H = -\frac{3}{4\pi} \left(\frac{1+\lambda^{-1}}{2} \right)^3 \int_{s \geq 2} g_0\left(\mathbf{s}\right) \left(\hat{\mathbf{M}}_{11} - \mathbf{I} \right) : \mathbf{uu} \, \mathrm{d}\mathbf{s}, \tag{2.37}$$

the interparticle contribution η_i^P:

$$\eta_i^P = \frac{3}{4\pi} \left(\frac{1+\lambda^{-1}}{2} \right)^2 \frac{2}{\text{Pe}} \oint_{s=2} g_0\left(\mathbf{s}\right) \left(\mathbf{n} \cdot \hat{\mathbf{M}}_r \right) \cdot \mathbf{u} \, \mathrm{d}\Omega, \tag{2.38}$$

and the Brownian contribution η_i^B:

$$\eta_i^B = \frac{3}{4\pi}\left(\frac{1+\lambda^{-1}}{2}\right)^2 \frac{1}{2\mathrm{Pe}}\int_{s\geq 2} g_0(\mathbf{s})\ \left(\nabla_{\mathbf{s}}\cdot\hat{\mathbf{M}}_r\right)\cdot\mathbf{u}\ \mathrm{d}\mathbf{s}, \tag{2.39}$$

where one may recall the definition of the unit vector $\mathbf{u}$ from Equation 2.33. We have also introduced the Péclet number

$$\mathrm{Pe} \equiv F_0\ b\left(1+\Delta\right)/2kT, \tag{2.40}$$

describing the relative strength of the external force F_0 disturbing the equilibrium suspension microstructure to the strength of Brownian forces $2kT/b\left(1+\Delta\right)$ repairing the disruption caused by the probe. The Péclet number is defined with respect to the excluded-volume size, and not the hydrodynamic size, of the bath particles. Note that in the integrals over all space (equations 2.37 and 2.39), the deviation of the dimensionless self-mobility of the probe particle from isotropy ($\hat{\mathbf{M}}_{11}-\mathbf{I}$), and the divergence of the relative mobility ($\nabla_{\mathbf{s}}\cdot\hat{\mathbf{M}}_r$), decay at large radial separations s as $O\left(s^{-4}\right)$ and $O\left(s^{-5}\right)$, respectively. Thus, these microviscosity integrals are convergent. Note that for the sake of compactness, we introduce the scalar function W to represent the divergence of the relative mobility tensor $\nabla_{\mathbf{s}}\cdot\hat{\mathbf{M}}_r$. The function W may be expressed in terms of the relative mobility functions L and M as follows:

$$\nabla_{\mathbf{s}}\cdot\hat{\mathbf{M}}_r = \left[\frac{2}{s}\left(L-M\right)+\frac{dL}{ds}\right]\mathbf{n} \equiv W\mathbf{n}. \tag{2.41}$$

The three contributions to the intrinsic microdiffusivity are analogous to the three microviscosity contributions. First, the intrinsic microdiffusivity due to hydrodynamic interactions $\mathbf{D}_i^H$ is defined as

$$\mathbf{D}_i^H = \frac{3}{4\pi}\left[\left(\frac{1+\lambda^{-1}}{2}\right)^3\int_{s\geq 2} g_0(\mathbf{s})\ \left(\hat{\mathbf{M}}_{11}-\mathbf{I}\right)\ \mathrm{d}\mathbf{s} - 2\mathrm{Pe}\left(\frac{1+\lambda^{-1}}{2}\right)^4\int_{s\geq 2}\mathbf{d}(\mathbf{s})\left(\hat{\mathbf{M}}_{11}-\mathbf{I}\right)\cdot\mathbf{u}\ \mathrm{d}\mathbf{s}\right]. \tag{2.42}$$

The **uu** component of the first integral for the hydrodynamic intrinsic microdiffusivity is identical to the expression for the hydrodynamic intrinsic microviscosity. The same hydrodynamic interactions between the probe and bath particles, that retard the mean motion of the probe, also hinder diffusion parallel to the direction of the applied external force. Also notable in this expression is the fact that both the steady state microstructure and the deflection field contribute to the hydrodynamic intrinsic microdiffusivity.

Both the interparticle and Brownian contributions to the intrinsic microdiffusivity resemble the respective intrinsic microviscosity contributions. The interparticle contribution to the intrinsic microdiffusivity is a surface integral of the first moment of the deflection field, just as the interparticle contribution to the intrinsic microviscosity is a surface integral of the first moment of the microstructure:

$$\mathbf{D}_i^P = \frac{3}{4\pi}\left(\frac{1+\lambda^{-1}}{2}\right)^3 4\oint_{s=2}\mathbf{d}\left(\mathbf{s}\right)\ \mathbf{n}\cdot\hat{\mathbf{M}}_r\ \mathrm{d}\Omega. \tag{2.43}$$

Just as the Brownian contribution to the microviscosity is the divergence of the relative mobility weighted by the suspension microstructure, the Brownian microdiffusivity is the divergence of the relative mobility weighted by the deflection field:

$$\mathbf{D}_i^B = \frac{3}{4\pi}\left(\frac{1+\lambda^{-1}}{2}\right)^3 \int_{s\geq 2}\mathbf{d}\left(\mathbf{s}\right)\ \nabla_{\mathbf{s}}\cdot\hat{\mathbf{M}}_r\ \mathrm{d}\mathbf{s}. \tag{2.44}$$

Determining the steady-state suspension microstructure g_0 and the deflection field $\mathbf{d}$ is the next step toward evaluating these expressions for the microviscosity and microdiffusivity.

2.2.2 Microstructural Governing Equations

To obtain governing partial differential equations for the steady-state suspension microstructure g_0 and the deflection field $\mathbf{d}$, the Fourier-space expressions for the probe particle and relative probability fluxes, $\hat{\mathbf{j}}_1$ and $\hat{\mathbf{j}}_2 - \hat{\mathbf{j}}_1$ defined from Equations 2.19 and 2.20, respectively, are substituted into the two-body Smoluchowski equation, Equation 2.21.The definition for the structure function g, Equation 2.24 is substituted into this expression. The bath-averaged probe flux terms, equations 2.22 and 2.23, are neglected in a dilute-theory approach, as those terms are $O\left(\phi_b^*\right)$ smaller than the rest. The choices of scales for the length and velocity, Equation 2.33, render the remaining terms in the Smoluchowski equation dimensionless as follows:

$$\begin{aligned}\frac{\partial g}{\partial t} - \nabla_{\mathbf{s}}\cdot\left(\hat{\mathbf{M}}_r\cdot\left(\mathrm{Pe}\ \mathbf{u} - i\mathbf{k}\frac{\lambda}{1+\lambda}\right)g\right) - \nabla_{\mathbf{s}}\cdot\hat{\mathbf{D}}_r\cdot\nabla_{\mathbf{s}}g \\ +i\mathbf{k}\cdot\left[\left(\hat{\mathbf{M}}_{11}-\mathbf{I}\right)\cdot\left(\mathrm{Pe}\ \mathbf{u} - i\mathbf{k}\frac{\lambda}{1+\lambda}\right)g + \frac{\lambda}{1+\lambda}\hat{\mathbf{M}}_r\cdot\nabla_{\mathbf{s}}g\right] &= 0.\end{aligned} \tag{2.45}$$

The disturbance caused by the translating probe must decay away at large distances from the probe:

$$g\left(\mathbf{k},\mathbf{s}\ ;\ t\right)\to 1 \quad \text{as } s\to\infty. \tag{2.46}$$

Said differently, this boundary condition indicates that there is no long-ranged order in the dispersion caused by the probe particle disturbance.

The excluded-annulus potential prevents any relative flux of probability along the line-of-centers at the minimum approach distance $r_{\min}$, or in terms of the dimensionless coordinates:

$$\mathbf{n}\cdot\left[-\hat{\mathbf{M}}_r\cdot\left(\mathrm{Pe}\ \mathbf{u} - i\mathbf{k}\frac{\lambda}{1+\lambda}\right)g - \hat{\mathbf{D}}_r\cdot\nabla_{\mathbf{s}}g\right] = 0 \quad \text{at } s=2. \tag{2.47}$$

The small-$\mathbf{k}$ expansion for the structure function g, Equation 2.25, and the assumption of steady state to determine the fully-developed microstructure about the probe, result in two leading order equations of $O(1)$ for the microstructure g_0 and $O(\mathbf{k})$ for the deflection field $\mathbf{d}$. From the choice of interparticle potential as the excluded-annulus model, Equation 2.3, one can show that the equilibrium microstructure is simply $g_0^{\text{eq}} = 1$ for all radial separations $s \geq 2$. With this in mind, it is useful to define the structural deformation function $f(\mathbf{s})$ in terms of the equilibrium microstructure:

$$g_0(\mathbf{s}) = g_0^{\text{eq}}(1 + f(\mathbf{s})). \tag{2.48}$$

The governing partial differential equations for the microstructural deformation function f and the deflection field $\mathbf{d}$ are

$$\begin{aligned} \text{Pe}\ \nabla_{\mathbf{s}} \cdot \left(\hat{\mathbf{M}}_r \cdot \mathbf{u}\ f\right) + \nabla_{\mathbf{s}} \cdot \hat{\mathbf{D}}_r \cdot \nabla_{\mathbf{s}} f &= -\text{Pe}\ \nabla_{\mathbf{s}} \cdot \left(\hat{\mathbf{M}}_r \cdot \mathbf{u}\right), & (2.49) \\ \text{Pe}\ \nabla_{\mathbf{s}} \cdot \left(\hat{\mathbf{M}}_r \cdot \mathbf{u}\ \mathbf{d}\right) + \nabla_{\mathbf{s}} \cdot \hat{\mathbf{D}}_r \cdot \nabla_{\mathbf{s}} \mathbf{d} &= \text{Pe}\left(\hat{\mathbf{M}}_{11} - \mathbf{I}\right) \cdot \mathbf{u}\ g_0 \\ &\quad + \frac{\lambda}{1+\lambda}\left[\nabla_{\mathbf{s}} \cdot \left(\hat{\mathbf{M}}_r\ g_0\right) + \hat{\mathbf{M}}_r \cdot \nabla_{\mathbf{s}} g_0\right]. & (2.50) \end{aligned}$$

The corresponding boundary conditions for the microstructural deformation function f are

$$f \to 0 \quad \text{as } s \to \infty, \tag{2.51}$$

$$\text{Pe}\ \mathbf{n} \cdot \hat{\mathbf{M}}_r \cdot \mathbf{u}\ f + \mathbf{n} \cdot \hat{\mathbf{D}}_r \cdot \nabla_{\mathbf{s}} f = -\text{Pe}\ \mathbf{n} \cdot \hat{\mathbf{M}}_r \cdot \mathbf{u} \quad \text{at } s = 2. \tag{2.52}$$

The corresponding boundary conditions for the deflection field $\mathbf{d}$ are

$$\mathbf{d} \to \mathbf{0} \quad \text{as } s \to \infty \tag{2.53}$$

$$\text{Pe}\ \mathbf{n} \cdot \hat{\mathbf{M}}_r \cdot \mathbf{u}\ \mathbf{d} + \mathbf{n} \cdot \hat{\mathbf{D}}_r \cdot \nabla_s \mathbf{d} = \frac{\lambda}{1+\lambda} g_0\ \mathbf{n} \cdot \hat{\mathbf{M}}_r \quad \text{at } s = 2. \tag{2.54}$$

The governing equations are scalar and vector inhomogeneous partial differential equations for the spatial evolution of the structural deformation function and the deflection field, respectively. For the structural deformation, the inhomogeneity in the PDE arises from a nonzero divergence of the relative mobility. For the deflection field, a nonzero divergence of the relative mobility, gradients in the suspension microstructure, and deviation of the dimensionless self mobility from isotropy all contribute to the inhomogeneity. The boundary conditions are also inhomogeneous at the minimum approach distance, owing to an inability of the equilibrium probability flux to penetrate the surface due to the imposition of the excluded-annulus potential. The coupled nature of the PDEs is evident; the solution for the steady-state microstructure is the driving inhomogeneity for the governing equations of the deflection field.

2.3 Linear Response Microstructure

When the restoring forces of Brownian motion are much stronger than the applied external force acting on the probe particle, the Péclet number is much less than unity. The leading-order disturbance from the equilibrium microstructure will be linear in the Péclet number, hence the name "linear response" is used in reference to this regime of a gentle disturbance easily repaired by random thermal fluctuations. In this limit, the deviation from the equilibrium microstructure f is expressed as a perturbation expansion in the small parameter Pe, as follows:

$$f\left(\mathbf{s};\ \mathrm{Pe}\to 0\right)=\mathrm{Pe}\ u_i n_i\ f_1\left(s\right)+\mathrm{Pe}^2\ u_i u_j\left[n_i n_j\ f_2\left(s\right)+\delta_{ij}\ f_3\left(s\right)\right]+O\left(\mathrm{Pe}^3\right) \tag{2.55}$$

Likewise, the deflection field $\mathbf{d}$ may also be expressed as a perturbation expansion in the small parameter Pe:

$$\mathbf{d}\left(\mathbf{s};\ \mathrm{Pe}\to 0\right)=n_i\ d_1\left(s\right)+\mathrm{Pe}\ u_j\left[n_i n_j\ d_2\left(s\right)+\delta_{ij}\ d_3\left(s\right)\right]+O\left(\mathrm{Pe}^2\right) \tag{2.56}$$

These forms for the departure from the equilibrium microstructure and the deflection field can be substituted into equations 2.49 and 2.50 to obtain a system of coupled ordinary differential equations. The details for these ODEs governing the perturbations to the microstructure and deflection field may be found in Appendix A. The perturbation to the suspension microstructure will be regular through terms of order $O\left(\mathrm{Pe}^2\right)$ while the perturbation to the deflection field is regular through $O\left(\mathrm{Pe}\right)$. In the limit where the Péclet number approaches zero, the intrinsic microviscosity contributions each approach a value independent of the Péclet number. The values of these $O\left(1\right)$ microviscosity contributions are as follows:

$$\eta^H_{i,0}=-\left(\frac{1+\lambda^{-1}}{2}\right)^3\int_2^\infty s^2\left(x^A_{11}+2y^A_{11}-3\right)\ \mathrm{d}s, \tag{2.57}$$

$$\eta^P_{i,0}=2\left(\frac{1+\lambda^{-1}}{2}\right)^2 L\left(\Delta\right)\ f_1\left(s=2\right), \tag{2.58}$$

$$\eta^B_{i,0}=\frac{1}{2}\left(\frac{1+\lambda^{-1}}{2}\right)^2\int_2^\infty f_1\left(s\right)\ s^2 W\ \mathrm{d}s. \tag{2.59}$$

From Equations 2.57-2.59, one can see that only the equilibrium suspension microstructure contributes to the leading linear-response hydrodynamic term of the intrinsic microviscosity, while the first perturbation to the microstructure is necessary to determine the leading linear-response interparticle and Brownian pieces of the intrinsic microviscosity. Note that $L\left(\Delta\right)$ denotes the value of the relative mobility function L evaluated at the minimum allowed separation between the probe and a bath particle $r=r_{\min}$, or in terms of the dimensionless coordinates $s=2\left(1+\Delta\right)$. Also note

that W is the divergence of the relative mobility as introduced in Equation 2.41.

The $O\left(\mathrm{Pe}^0\right)$ hydrodynamic contribution to the intrinsic microviscosity in the linear response regime $\eta_{i,0}^H$ is plotted in Figure 2.2 for various size ratios as a function of the excluded annulus parameter Δ. Recall that $\eta_{i,0}^H$ describes the hindrance of the probe due to a reduced self-mobility from the equilibrium distribution of bath particles. The hydrodynamic contribution to the intrinsic microviscosity is a monotonically decreasing function of the excluded annulus parameter, eventually becoming negligible for all size ratios once the excluded annulus parameter Δ is $\gtrsim O(1)$. For a given excluded annulus parameter, $\eta_{i,0}^H$ is a monotonically decreasing function of the particle size ratio λ. A probe particle that is much smaller than the bath particles does not get to sample as much of the equilibrium distribution within a few radii of its center, while large probes are affected by a much larger sample of the bath equilibrium distribution. As the size ratio λ approaches zero indicating that the bath particles are infinitesimally small, the result is that the suspended bath particles in solvent resembles a continuum to the large probe particle and Einstein's viscosity correction of $\eta_{i,0}^H \to 5/2$ is recovered for small excluded annuli. For small probes, the deviation of the probe's self mobility from isotropy $\hat{\mathbf{M}}_{11} - \mathbf{I}$ is $O(1)$ in a region of thickness $O\left(\lambda^{-1}\right)$ about the probe, indicating that the hydrodynamic contribution to the intrinsic microviscosity is $O\left(\lambda^{-1}\right)$.

The $O\left(\mathrm{Pe}^0\right)$ Brownian contribution to the intrinsic microviscosity in the linear response regime $\eta_{i,0}^B$ is plotted in Figure 2.3 for various size ratios as a function of the excluded annulus parameter Δ. With no excluded volume interactions ($\Delta \to 0$), the function $\eta_{i,0}^B$ is a monotonically increasing function of the particle size ratio λ, eventually reaching a maximum value of $\eta_{i,0}^B(\lambda \to \infty, \Delta = 0) = 1/2$ denoted by the dashed line in Figure 2.3. This limiting value of $1/2$ holds for small probe particles so long as the excluded annulus interaction distance $\Delta(a+b)$ is much smaller than the probe's hydrodynamic radius a, indicating that the Brownian contribution arises from lubrication hydrodynamic interactions. Note that for certain excluded annulus parameters Δ around $O(1)$, the Brownian contribution $\eta_{i,0}^B$ exhibits nonmonotonicity in the size ratio λ.

The $O\left(\mathrm{Pe}^0\right)$ interparticle contribution to the intrinsic microviscosity in the linear response regime $\eta_{i,0}^P$ is plotted in Figure 2.4 for various size ratios as a function of the excluded annulus parameter Δ. Note that the curve for each size ratio is normalized by the limiting value $\eta_{i,0}^P(\lambda, \Delta \to \infty) = \left(1+\lambda^{-1}\right)^2/2$. In terms of the parameter $\beta \equiv 2/\left(1+\lambda^{-1}\right)$, used by Zia and Brady [60], this limiting interparticle contribution to the intrinsic microviscosity is $\eta_{i,0}^P(\lambda, \Delta \to \infty) = 2\beta^{-2}$. From this series of curves one can infer that for small probes, corresponding with large λ, once the lubrication interactions are excluded, bath particles can easily reach the minimum approach distance without hydrodynamic hindrance and collide with the probe. For large probes, which corresponds with small λ, long-ranged hydrodynamic effects continue to stall the trajectories of bath particles from reaching the probe; collisions are hence less frequent even with moderate values of Δ. These collisions at the minimum approach distance are what contribute to $\eta_{i,0}^P$, and so we see that as λ decreases from 8

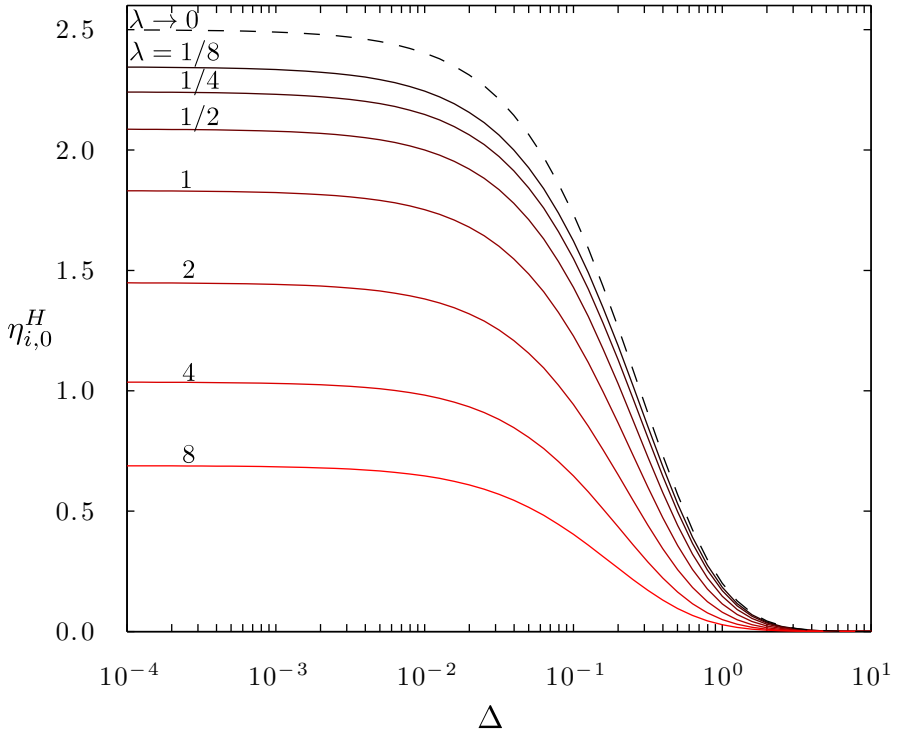

Figure 2.2: Intrinsic hydrodynamic microviscosity contribution $\eta^H_{i,0}$ in the limit $\mathrm{Pe} \to 0$ as a function of the excluded-annulus parameter Δ for multiple bath-to-probe particle size ratios $\lambda \equiv b/a$. Colors brighten with decreasing probe particle size.

to 1/8, larger and larger excluded annulus parameters are necessary to reach the limiting value of the interparticle contribution.

The leading-order perturbations to the suspension microstructure $f_1(s)$ and the deflection field $d_1(s)$ for a given size ratio and excluded annulus parameter are a scalar multiple of one another: $d_1(s) = -\lambda f_1(s)/(1+\lambda)$. The values of the $O(1)$ effective diffusivity contributions are isotropic and are thus directly related to their respective linear-response intrinsic microviscosity contributions as follows:

$$\mathbf{D}^H_{i,0} = -\eta^H_{i,0}\mathbf{I}, \tag{2.60}$$

$$\mathbf{D}^P_{i,0} = -\eta^P_{i,0}\mathbf{I}, \tag{2.61}$$

$$\mathbf{D}^B_{i,0} = -\eta^B_{i,0}\mathbf{I}. \tag{2.62}$$

Without directed motion of the probe, *i.e.* when the Péclet number is identically zero, there is nothing driving the probe to preferentially diffuse in a specific direction, and it diffuses with an effective long-time self diffusivity, which can be interpreted as the leading order intrinsic microviscosity. The corrections to these $O(1)$ intrinsic quantities depend on higher-order terms in the perturbation ex-

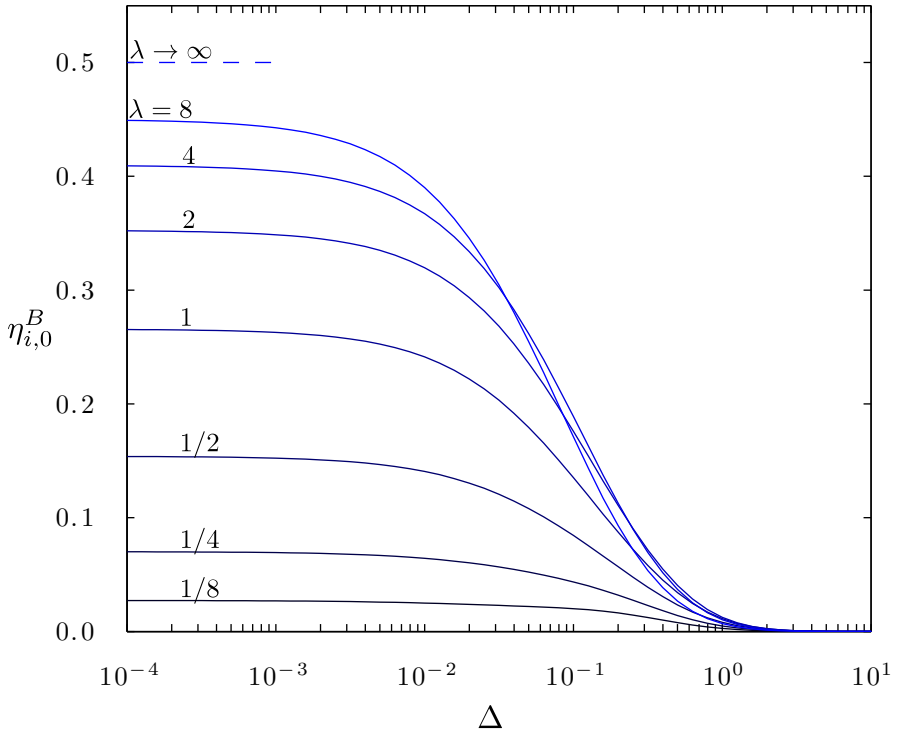

Figure 2.3: Intrinsic Brownian microviscosity contribution $\eta^B_{i,0}$ in the limit $\mathrm{Pe} \to 0$ as a function of the excluded-annulus parameter Δ for multiple bath-to-probe particle size ratios $\lambda \equiv b/a$. Colors brighten with decreasing probe particle size. A discussion of the limiting value of $\eta^B_{i,0} \to 1/2$ for small probes, denoted by the dashed line, can be found in section 2.3.2.

pansion, for whose consideration we should address the singular nature of the perturbation expansion in powers of Péclet number.

2.3.1 Outer Problem

As discussed by Khair and Brady [29], the higher-order perturbations to the equilibrium microstructure will not all decay to zero as $s \to \infty$ to satisfy the far-field boundary condition of no long-ranged suspension order. The key feature to this perturbation expansion is that the advective motion of a given term in the expansion drives the next smallest term, in terms of powers of Pe, from equilibrium. This assumes that the advective term is always $O(\mathrm{Pe})$ small compared to the diffusive term. At radial separations of $O\left(\mathrm{Pe}^{-1}\right)$, this is no longer the case. At these distances, advection of the probe is comparable in magnitude to diffusion. We define an outer radial coordinate $\rho \equiv \mathrm{Pe}\ s \sim O(1)$ which will be used to determine the outer solution $F(\boldsymbol{\rho})$. To leading order, for the structural deformation we find

$$\mathbf{u} \cdot \nabla_{\boldsymbol{\rho}} F(\boldsymbol{\rho}) + \nabla^2_{\boldsymbol{\rho}} F = 0. \tag{2.63}$$

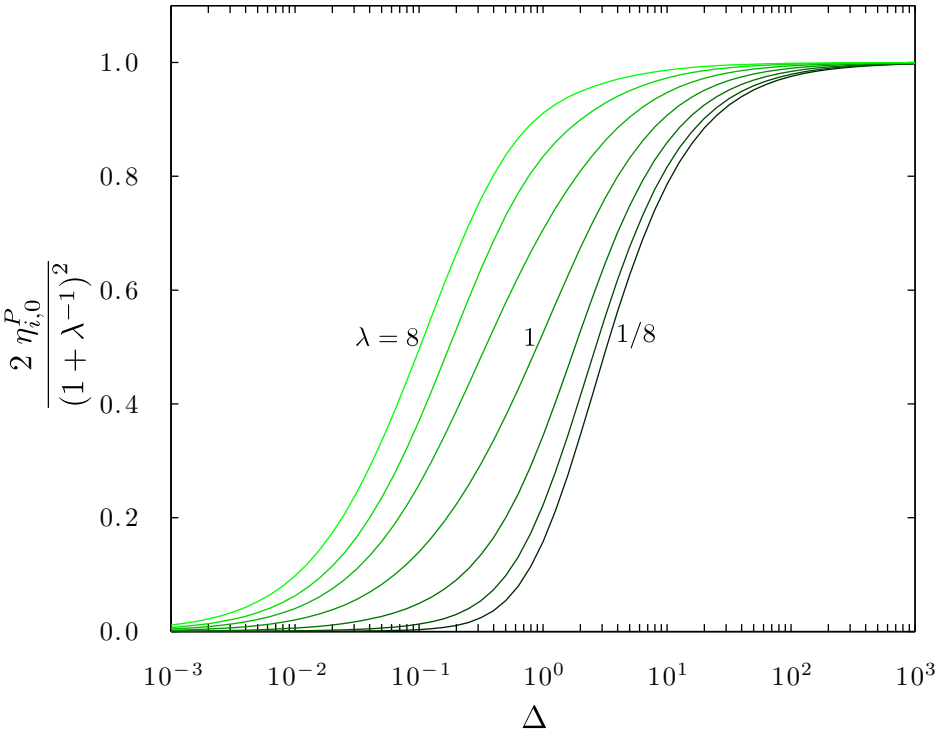

Figure 2.4: Intrinsic interparticle microviscosity contribution $\eta_{i,0}^{P}$ normalized by the no-hydrodynamics value of the intrinsic microviscosity $\left(1+\lambda^{-1}\right)^{2}/2$. Values are expressed in the limit $\mathrm{Pe} \to 0$ as a function of the excluded-annulus parameter Δ for the bath-to-probe particle size ratios $\lambda \equiv b/a$ of 8, 4, 2, 1, 1/2, 1/4, and 1/8. Colors brighten with decreasing probe particle size.

Note that the hydrodynamic functions L, M, G, and H are all absent from the leading-order governing equation for the outer problem, as each of these hydrodynamic functions may be written in a far-field expansion as $1 + O\left(\mathrm{Pe}\ \rho^{-1}\right)$. Likewise, the divergence of the relative mobility W decays like $O\left(\mathrm{Pe}^{5}\rho^{-5}\right)$ in the outer region and is thus neglected from the leading order governing equation. The solution $F\left(\boldsymbol{\rho}\right)$ to this outer problem must match the functional form of the perturbation f given in Equation 2.55 as the outer coordinate ρ approaches zero. The far-field behavior of the leading-order structural deformation $\mathrm{Pe} f_1\left(s\right)$, which is a dipole in character, is $O\left(\mathrm{Pe}\ s^{-2}\right)$ which scales as $O\left(\mathrm{Pe}^{3}\rho^{-2}\right)$ in terms of the outer coordinate. Thus, the outer solution F is predicted to be $O\left(\mathrm{Pe}^{3}\right)$ to leading order

$$F\left(\boldsymbol{\rho};\ \mathrm{Pe} \to 0\right) = \mathrm{Pe}^{3} F_1\left(\boldsymbol{\rho}\right) + O\left(\mathrm{Pe}^{4}\right).$$

The advection and diffusion terms are identical for the governing equations for the suspension microstructure and the deflection field. Thus, the perturbation to the deflection field is also singular, and the transition to the outer solution $\mathbf{D}\left(\boldsymbol{\rho}\right)$ occurs at the same length scale $\rho = \mathrm{Pe}\ s$ as for the outer solution for the steady microstructure. Similarly, the far-field behavior of the leading-order

perturbation to the deflection field $d_1(s)$, which is also a dipole in character, is $O\left(s^{-2}\right)$ which behaves as $O\left(\mathrm{Pe}^2\rho^{-2}\right)$ in terms of the outer coordinate. The outer solution $\mathbf{D}$ is thus predicted to be $O\left(\mathrm{Pe}^2\right)$ to leading order

$$\mathbf{D}\left(\boldsymbol{\rho};\ \mathrm{Pe}\to 0\right)=\mathrm{Pe}^2\mathbf{D}_1\left(\boldsymbol{\rho}\right)+O\left(\mathrm{Pe}^3\right).$$

The governing equation for the leading-order outer solution for the deflection field requires the gradient of the leading-order outer solution for the steady microstructure

$$\mathbf{u}\cdot\nabla_{\boldsymbol{\rho}}\mathbf{D}_1+\nabla^2_{\boldsymbol{\rho}}\mathbf{D}_1=\frac{2\lambda}{1+\lambda}\nabla_{\boldsymbol{\rho}}F_1\left(\boldsymbol{\rho}\right).$$

The detailed outer solutions are not necessary for determining the leading-order contributions in Pe to the intrinsic microviscosity or the effective diffusivity. Recall that the integrand of the hydrodynamic contribution to the intrinsic microviscosity is $\sim f\left(\mathbf{s}\right)\left(\hat{\mathbf{M}}_{11}-\mathbf{I}\right):\mathbf{uu}$. For large separations, the departure of the dimensionless self-mobility $\hat{\mathbf{M}}_{11}$ from isotropy is $O\left(s^{-4}\right)$ or $O\left(\mathrm{Pe}^4\rho^{-4}\right)$ in terms of the outer coordinate. Similarly, recall that the integrand of the Brownian contribution to the intrinsic microviscosity is $\sim \mathrm{Pe}^{-1}\ f\ \nabla_s\cdot\hat{\mathbf{M}}_r$. For large separations, the divergence of the relative mobility $\nabla_{\mathbf{s}}\cdot\hat{\mathbf{M}}_r$ is $O\left(s^{-5}\right)$ or $O\left(\mathrm{Pe}^5\rho^{-5}\right)$ in terms of the outer coordinate. Thus, the leading order hydrodynamic and Brownian contributions to the intrinsic microviscosity from the outer solution are $O\left(\mathrm{Pe}^4\right)$ small.

In the next section, specific microstructural considerations will be addressed for very small and large probes.

2.3.2 Small Probe Limit $\lambda \gg 1$

As was seen in Figure 2.3, the Brownian contribution to the intrinsic microviscosity becomes larger with decreasing probe size, and is shown to approach an asymptotic limit of $\eta^B_{i,0}\left(\lambda\to\infty,\Delta=0\right)$ of 1/2. In this section, this asymptotic result is verified. This analysis incorporates full hydrodynamic interactions, so the excluded volume radii of the probe and bath particles are coincident with the hydrodynamic radii. When the probe particle is much smaller compared to the other bath particles in the dispersion, it is the inverse of the particle size ratio $\lambda^{-1}=a/b$ that is much less than unity. Lubrication interactions between the probe and bath particle become important in this regime when the gap spacing $r-(a+b)$ is less than the smaller of the two particle radii, in this case the probe radius a. In terms of the dimensionless gap spacing $\xi=s-2$, this lubrication criterion is simply $\xi\lesssim\lambda^{-1}$. Outside the lubrication region, the relative diffusivity $\mathbf{D}^*_r$ and relative mobility $\mathbf{M}^*_r$ both simplify to the isotropic identity tensor $\mathbf{I}$ plus corrections of order $O\left(\lambda^{-1}\right)$, while the divergence of the relative mobility scales as λ^{-1} to leading order. These limiting forms simplify the governing

PDE for the microstructure outside of the lubrication region as follows:

$$\text{Pe}\ \mathbf{u}\cdot\nabla_s g_0 + \nabla_s^2 g_0 + O\left(\lambda^{-1}\right) = 0. \tag{2.64}$$

Note that the leading order PDE outside of the lubrication region is identical to the governing equation in the absence of hydrodynamic interactions, *i.e.* for an infinite excluded-annulus parameter Δ. Inside the lubrication region, when $\xi \ll \lambda^{-1} \ll 1$, we use the results presented in section 2 of Batchelor's work on sedimentation in polydisperse suspensions [5] to show that the relative diffusivity and relative mobility take on the following forms:

$$\hat{\mathbf{D}}_r\left(\lambda^{-1}\ll 1,\ \xi \ll \lambda^{-1}\right) \sim \frac{(1+\lambda)^2}{2\lambda}\xi\ \mathbf{nn} + \left(h_0 + \frac{h_1}{\ln \xi^{-1}}\right)(\mathbf{I}-\mathbf{nn}), \tag{2.65}$$

$$\hat{\mathbf{M}}_r\left(\lambda^{-1}\ll 1,\ \xi \ll \lambda^{-1}\right) \sim \frac{(1+\lambda)^3}{2\lambda^2}\xi\ \mathbf{nn} + \left(m_0 + \frac{m_1}{\ln \xi^{-1}}\right)(\mathbf{I}-\mathbf{nn}). \tag{2.66}$$

In equations 2.65 and 2.66, h_α and m_α are constants that are no greater than $O\left(\lambda^0\right)$. With these forms in mind, the leading order governing PDE for the microstructure inside the lubrication region is simply a radial flux balance

$$\frac{\lambda}{2}\ \mathbf{n}\cdot\left[\text{Pe}\ \mathbf{u}g_0 + \nabla_s g_0\right] + O\left(\lambda^0\right) = 0 \quad \left(\xi \ll \lambda^{-1}\right). \tag{2.67}$$

Note that microstructural gradients with respect to s (and not with respect to ξ) are $O(1)$ in the linear response regime. This form of the governing equation is identical to the boundary condition at the surface. In fact, the same perturbation expansion for the microstructure in the absence of hydrodynamic interactions satisfies the governing equation in the lubrication region to leading order in λ

$$\begin{aligned} g_0\left(\text{Pe}\ll 1;\ \lambda^{-1}\ll 1\right) \quad = \quad & 1 + \text{Pe}\ \mathbf{u}\cdot\mathbf{n}\ \left[\left(\frac{2}{s}\right)^2 + O\left(\lambda^{-1}\right)\right] \\ & + \text{Pe}^2\mathbf{uu}:\mathbf{nn}\left[\left(\frac{2}{s}\right)^3 - \frac{2}{s} + O\left(\lambda^{-1}\right)\right] \\ & - \text{Pe}^2\mathbf{uu}:\mathbf{I}\left[\frac{1}{3}\left(\frac{2}{s}\right)^3 - \frac{2}{s} + O\left(\lambda^{-1}\right)\right] + O\left(\text{Pe}^3\right). \end{aligned} \tag{2.68}$$

The Brownian piece of the intrinsic microviscosity is represented by the integral in equation 2.39. This integrand is $O\left(\lambda^{-1}\right)$ small outside of the lubrication region, where the divergence of the relative mobility scales as λ^{-1}. Thus, we can use the divergence theorem to re-write the Brownian

contribution to the intrinsic microviscosity as

$$\eta_i^B = \frac{3}{4\pi}\left(\frac{1+\lambda^{-1}}{2}\right)^2 \frac{1}{2\mathrm{Pe}}\left[-\oint_{s=2} g_0(\mathbf{s})\ \mathbf{n}\cdot\mathbf{M}_r^*\cdot\mathbf{u}\ \mathrm{d}\Omega + \oint_{s=2+\epsilon} g_0(\mathbf{s})\ \mathbf{n}\cdot\mathbf{M}_r^*\cdot\mathbf{u}\ \mathrm{d}\mathbf{\Omega}\right], \quad (2.69)$$

where a radial center-to-center separation of $2+\epsilon$ lies just outside of the lubrication region, and so $\epsilon \gtrsim \lambda^{-1}$. The surface integral at $s=2$ is zero owing to the zero relative mobility of particles in hydrodynamic contact with one another. Outside the lubrication layer, the relative mobility tensor is simply the identity tensor. We thus see that the Brownian contribution to the intrinsic microviscosity for small probe particles takes on the form of a surface integral much like the interparticle contribution to the intrinsic microviscosity, displaced just outside the lubrication region. The value of the Brownian contribution to the microviscosity in this limit is

$$\eta_i^B\left(\mathrm{Pe}\ll 1,\ \lambda^{-1}\ll 1\right) = \frac{1}{2} + O\left(\lambda^{-1},\ \mathrm{Pe}^2\right). \quad (2.70)$$

Note that this value is identical the interparticle contribution to the intrinsic microviscosity for small probes with an excluded annulus parameter $\Delta \gtrsim \lambda^{-1}$. Thus, we predict that the sum of the interparticle and Brownian contributions to the intrinsic microviscosity for infinitesimally small probe particles will uniformly approach 1/2. When the excluded annulus parameter Δ is greater than $O\left(\lambda^{-1}\right)$, the contribution is strictly a result of the excluded annulus interparticle potential.

Lastly, we can consider the hydrodynamic contribution to the intrinsic microviscosity $\eta_{i,0}^H$ for infinitesimally small probes. Recall that the $O(1)$ hydrodynamic piece is given by the equilibrium microstructure and so for small probes is equal to:

$$\eta_{i,0}^H = \frac{3}{8}\int_2^{2+\epsilon} s^2\ \mathrm{d}s + O\left(\lambda^{-1}\right),$$

where $\epsilon(\lambda) \sim O\left(\lambda^{-1}\right)$ so that the integral captures only the lubrication region. This integral is $O\left(\lambda^{-1}\right)$ and so we expect the hydrodynamic contribution to the intrinsic microviscosity to vanish for small probes in the linear-response regime.

2.3.3 Large Probe Limit $\lambda \ll 1$

When we consider small bath particles and small excluded annulus parameters, care must be taken in the order of these limits approaching zero. As long as the bath particles are smaller in size than the excluded annulus thickness, *i.e.* $a \gg \Delta a > b$, then nearly-touching configurations of the probe and bath particle, in which lubrication interactions are important, are prohibited by the excluded-annulus potential. Thus, the two-body hydrodynamic functions take on simple forms. The relative diffusivity tensor $\hat{\mathbf{D}}_r$ to leading order in λ is isotropic and unchanged from the value neglecting hydrodynamic interactions; in other words, G and H are equal to unity. The functions L and M

appearing in the relative mobility tensor $\hat{\mathbf{M}}_r$ take on the following forms:

$$L\left(s, \lambda \ll 1\right) = 1 - \frac{3}{\left(1+\Delta\right)} s^{-1} + \frac{4}{\left(1+\Delta\right)^3} s^{-3} + O\left(\lambda\right), \tag{2.71}$$

$$M\left(s, \lambda \ll 1\right) = 1 - \frac{3}{2\left(1+\Delta\right)} s^{-1} - \frac{2}{\left(1+\Delta\right)^3} s^{-3} + O\left(\lambda\right). \tag{2.72}$$

Equations 2.71 and 2.72 are simply expressions for the fluid velocity outside of a translating sphere, indicating that bath particles simply are carried along with the fluid. The contact value of the mobility function $L\left(s=2\right)$ is important because it describes the strength of the advective flux evaluated at the minimum radial separation of the probe and bath particle, *i.e.* how easy is it for bath particles to be compressed toward the surface of the probe particle. We define this parameter as $L\left(\Delta\right)$

$$L\left(\Delta\right) = \frac{3}{2}\Delta^2 \left[\frac{1+2\Delta/3}{\left(1+\Delta\right)^3}\right]. \tag{2.73}$$

Note that $L\left(\Delta\right)$ scales with the square of the excluded annulus parameter. The equivalent contact value of the mobility function governing sliding motion past the probe $M\left(\Delta\right)$ is linear in the excluded annulus parameter to leading order. This means small bath particles will more readily move around the oncoming probe particle than advect toward its surface. Thus, we expect there to be great difficulty in accumulating bath particle probability density on the anterior face of the large probe. This fact manifests itself in the the pair-distribution function g_0 for large probes,

$$\begin{aligned} g_0\left(\mathrm{Pe} \ll 1;\ \lambda \ll 1\right) &= 1 + \mathrm{Pe}\ \mathbf{u}\cdot\mathbf{n}\ f_1\left(s;\ \lambda \ll 1\right) \\ &\quad + \mathrm{Pe}^2\ \mathbf{uu}:\mathbf{nn}\ f_2\left(s;\ \lambda \ll 1\right) \\ &\quad + \mathrm{Pe}^2\ \mathbf{uu}:\mathbf{I}\ f_3\left(s;\ \lambda \ll 1\right) + O\left(\mathrm{Pe}^3\right), \end{aligned} \tag{2.74}$$

where the scaling of the microstructural disturbance as $L\left(\Delta\right)$ is evident in each of the perturbations f_1, f_2, and f_3 to the equilibrium microstructure:

$$f_1\left(s;\ \lambda \ll 1\right) = 4L\left(\Delta\right) s^{-2} + O\left(\lambda\right), \tag{2.75}$$

$$f_2\left(s;\ \lambda \ll 1\right) = L\left(\Delta\right)\left[-\frac{2}{s} + \frac{15}{2\gamma s^2} + \left(8 - \frac{18}{\gamma}\right) s^{-3} + \frac{4}{\gamma^3 s^4} + O\left(\lambda\right)\right], \tag{2.76}$$

$$f_3\left(s;\ \lambda \ll 1\right) = L\left(\Delta\right)\left[\frac{2}{s} - \frac{9}{2\gamma s^2} - \left(\frac{8}{3} - \frac{6}{\gamma}\right) s^{-3} + O\left(\lambda\right)\right]. \tag{2.77}$$

Here, $\gamma = 1 + \Delta$. When the probe is much larger than the bath particles, the Brownian contribution to the intrinsic microviscosity vanishes even for very small excluded annulus parameters. This is because the divergence of the relative mobility $\nabla\cdot\hat{\mathbf{M}}_r = W\mathbf{n}$, which appears in the integrand for the Brownian contribution, is $O\left(\lambda^3\right)$ small. The hydrodynamic contribution to the intrinsic

microviscosity results from a reduction in the probe's self mobility due to the equilibrium distribution of bath particles about the probe. As long as the bath particles are smaller in size than the excluded annulus thickness, *i.e.* $\Delta a > b$, then the hydrodynamic contribution to the intrinsic microviscosity has the following functional form:

$$\eta_{i,0}^{H}\left(\Delta, \lambda \ll 1\right) = \frac{5}{2}\left(\frac{3}{2\gamma^4} - \frac{1}{\gamma^6} + \frac{1}{2\gamma^8}\right) + O\left(\lambda\right). \tag{2.78}$$

In the limit where the minimum approach distance between the probe and bath particle is coincident with the hydrodynamic radius, $\Delta \rightarrow 0$, $\eta_{i,0}^{H}$ approaches the value 5/2 consistent with the $O\left(\phi\right)$ Einstein viscosity correction. As the excluded annulus parameter is increased, the hydrodynamic contribution $\eta_{i,0}^{H}$ decreases monotonically with Δ eventually reaching zero once the interactions between the probe and bath particle are strictly via collisions at the excluded annulus.

2.4 Weakly Nonlinear Trends

The intrinsic microviscosity and effective diffusivity at low Péclet number are $O\left(\mathrm{Pe}^0\right)$ quantities, as was seen in Section 2.3. The next largest contribution to each of these quantities is $O\left(\mathrm{Pe}^2\right)$ and results from the first nonlinear perturbation to the suspension microstructure, namely $f_2\left(s\right)$ and $f_3\left(s\right)$. The perturbations $f_2\left(s\right)$ and $f_3\left(s\right)$ are monopolar and quadrupolar in nature, and hence they only contribute to the hydrodynamic intrinsic microviscosity and effective diffusivity. Dipolar disturbances to the microstructure affect the interparticle and Brownian contributions to the microviscosity and effective diffusivity, but the next dipolar perturbation comes in at $O\left(\mathrm{Pe}^3\right)$ for the suspension microstructure and at $O\left(\mathrm{Pe}^2\right)$ for the deflection field. The $O\left(\mathrm{Pe}^2\right)$ hydrodynamic contribution to the intrinsic microviscosity is as follows:

$$\frac{\eta_i^H\left(\mathrm{Pe} \ll 1\right) - \eta_{i,0}^H}{\mathrm{Pe}^2} = -\left(\frac{1+\lambda^{-1}}{2}\right)^3 \int_2^\infty \frac{s^2}{5} f_2\left[3x_{11}^A + 2y_{11}^A - 5\right] + s^2 f_3\left[x_{11}^A + 2y_{11}^A - 3\right]\, \mathrm{d}s. \tag{2.79}$$

The results of Equation 2.79 are plotted in Figure 2.5. This contribution is positive for all size ratios and excluded annulus parameters, indicating that the hydrodynamic contribution always has a force-thickening effect on the perceived viscosity of a translating probe. Interestingly, the $O\left(\mathrm{Pe}^2\right)$ contribution exhibits nonmonotonicity in both the excluded annulus parameter for certain size ratios and in the particle size ratio λ for certain excluded annulus parameters. In the limit where the excluded annulus coincides with the hydrodynamic radii of the probe and bath particle, *i.e.* $\Delta \rightarrow 0$, the $O\left(\mathrm{Pe}^2\right)$ force-thickening due to hydrodynamic interactions attains a maximum value between $\lambda = 2$ and $\lambda = 8$. Beyond size ratios of $\lambda = 8$, as the probe gets smaller, the hydrodynamic contribution will continue to decrease. Again, the deviation of the probe particle's self mobility from isotropy $\hat{\mathbf{M}}_{11} - \mathbf{I}$ is $O\left(1\right)$ only in a region of thickness $O\left(\lambda^{-1}\right)$, and so the Pe^2 force thickening for

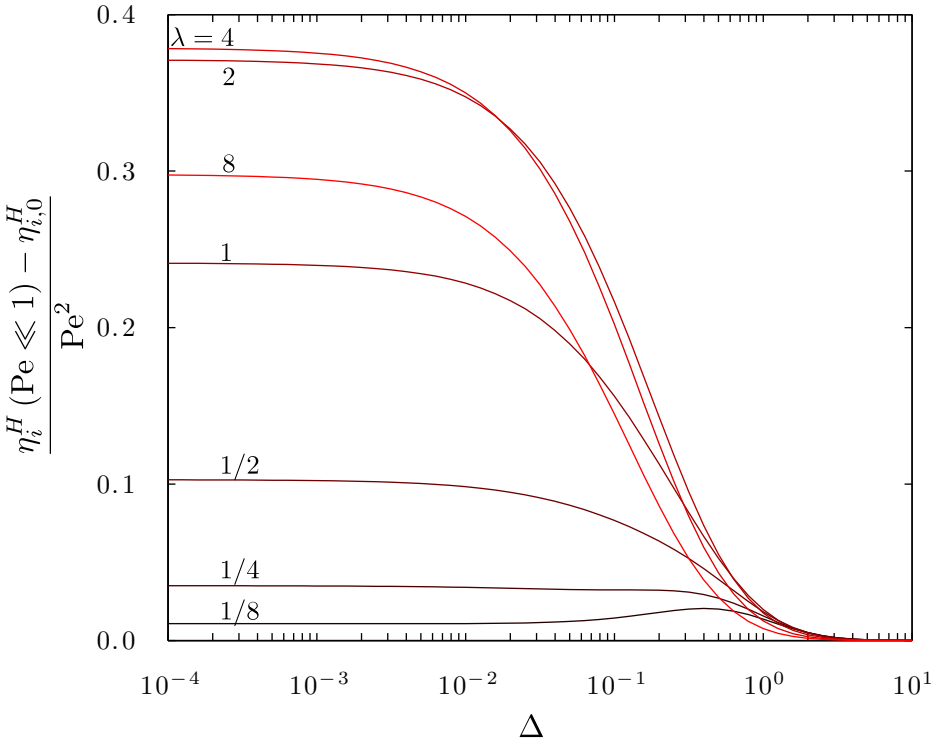

Figure 2.5: The $O\left(\mathrm{Pe}^2\right)$ contribution to the hydrodynamic microviscosity η_i^H in the limit $\mathrm{Pe} \to 0$ as a function of the excluded-annulus parameter Δ for multiple bath-to-probe particle size ratios $\lambda \equiv b/a$. Colors brighten with decreasing probe particle size.

small probes is $O\left(\lambda^{-1}\right)$.

For small bath particles, recall that the perturbations to the equilibrium microstructure, and consequently the contributions to the intrinsic microviscosity, are proportional to the small parameter $L(\Delta) \sim \Delta^2$, so it appears there is some value of Δ at which the competing effects of a disturbance from the equilibrium microstructure and the deviation of the self-mobility from isotropy can maximize the force-thickening due to hydrodynamic interactions. This is evidenced in the $\lambda = 1/8$ curve in Figure 2.5. As was discussed in Section 2.3, the outer region of the suspension microstructure results in leading order $O\left(\mathrm{Pe}^4\right)$ contributions to the intrinsic microviscosity, so it makes sense that these $O\left(\mathrm{Pe}^2\right)$ contributions decay to zero with increasing Δ. Lastly, it is important to note that although the hydrodynamic contribution to the intrinsic microviscosity results in force-thickening, we will see when we examine the Brownian and interparticle contributions for finite Péclet numbers that the total intrinsic microviscosity actually force-*thins* with increasing Péclet number at low Pe, indicating that initially the Brownian contribution to the intrinsic microviscosity decays faster than the hydrodynamic contribution grows. In order to see this from the perturbation expansion, we would need to continue the expansion of the microstructure to the next power of Péclet number,

namely to $O\left(\mathrm{Pe}^3\right)$.

2.5 Numerical Methods for Finite Péclet Number

The perturbation methods in Section 2.3 rely on the Péclet number being small enough that only the leading order terms in the perturbation expansions are significant, namely the dipole in the suspension microstructure and the deflection field. As the Péclet number increases, the simple dipolar field develops into a more complex structure; on the upstream face of the probe the accumulation region compresses toward the surface and the probability density grows with the Péclet number. On the downstream face, the depletion region lengthens into a trailing wake because the probe can make more and more forward progress before bath particles can anneal the disturbance. In order to solve for these features in the spatial distribution of the suspension microstructure g_0 and the deflection field $\mathbf{d}$ once the Péclet number is $\sim O(1)$ or larger, different numerical techniques are required. In this section, two numerical techniques are discussed. The first method, a Legendre polynomial expansion, is a natural extension of the small-Péclet perturbation expansion, and it works well for low-to-moderate Péclet numbers. The second method, a second-order finite difference scheme, concentrates grid points in the compression boundary layer to capture the large microstructural gradients present near the surface at high Péclet number. In this work, the Legendre polynomial solution method is used for Péclet from 10^{-3} up to 10^{1}, while the finite difference method solves the Smoluchowski equation up through Péclet numbers of 10^{4}. The microstructure is axially symmetric about the direction of probe forcing. Hence, both of these schemes solve for the microstructure in terms of two coordinates: the center-to-center separation of the probe and bath particle s, and the polar angle θ as measured from the direction of the constant applied external force. These numerical methods worked well for same-sized probe and bath particles in the work of Khair and Brady [29] and are extended here to arbitrary size ratios.

2.5.1 Orthogonal Polynomial Expansion

In order to motivate the solution method via orthogonal polynomials, we return our attention to the perturbation expansions from Section 2.3. At low Péclet number, the pair-distribution function can be solved for using a perturbation expansion in powers of Pe. We know that the Péclet number is linear in the applied external force, so each occurrence of the Péclet number is accompanied by one applied external force vector $\mathbf{u}$:

$$f(\mathbf{s}) = \mathrm{Pe}\ \mathbf{u}\cdot\mathbf{n}\ f_1(r) + \mathrm{Pe}^2\mathbf{uu} : (\mathbf{nn}\ f_2(r) + \mathbf{I}\ f_3(r)) + O\left(\mathrm{Pe}^3\right). \tag{2.80}$$

Note that for the Legendre polynomial method, the coordinate system is as follows: $\theta = 0$ corresponds to the compressional region in front of the probe and $\theta = \pi$ corresponds to the extensional region behind the probe, and so $\mathbf{u} \cdot \mathbf{n} = \cos\theta$. The largest term in the perturbation expansion, proportional to Pe, has angular dependence $\cos\theta$. In terms of Legendre polynomials, this is simply $\cos\theta = P_1(\cos\theta)$. Similarly, we may write the double-dot product $\mathbf{uu} : \mathbf{nn} = \cos^2\theta$ using the Legendre Polynomials P_2 and P_0

$$\cos^2\theta = \frac{2}{3}P_2(\cos\theta) + \frac{1}{3}P_0(\cos\theta). \tag{2.81}$$

If we approximate the function $f(s,\theta)$ as an expansion of the first three Legendre polynomials:

$$f(s,\theta) \approx q_0(r)\,P_0(\cos\theta) + q_1(r)\,P_1(\cos\theta) + q_2(r)\,P_2(\cos\theta), \tag{2.82}$$

we can replicate the functional form of the perturbation expansion of f, Equation 2.80, up to order Pe^3. Thus, when the Péclet number is small, namely $< O(1)$, one only needs the first few terms in a Legendre polynomial expansion to faithfully capture the salient features of the pair-distribution function. For moderate Péclet numbers ($\sim O(1) - O(10)$), a longer series of terms can still approximate the microstructure successfully.

The detailed method is as follows: we approximate the pair-distribution function as a finite series of as-yet unknown radial functions $q_m(s)$. Each radial function $q_m(s)$ multiplies the corresponding Legendre polynomial P_m. It is useful to transform the angular variable θ to the natural argument for Legendre Polynomials, $\mu \equiv \cos\theta$. The series truncates at some index $m_{\max}$

$$f(s,\mu) = \sum_{m=0}^{m_{\max}} q_m(s)\,P_m(\mu). \tag{2.83}$$

This series is substituted into the governing equation for the microstructure expressed in terms of s and μ, and a system of coupled radial ODEs is recovered;

$$\mathrm{Pe}\,\left[W\alpha_m(s) + L\beta_m(s) + \frac{M}{s}\gamma_m(s)\right] + \mathscr{D}_m[q_m(s)] = 0, \tag{2.84}$$

where the diffusion operator $\mathscr{D}_m$ is defined as

$$\mathscr{D}_m[q_m(s)] = Gq_m''(s) + \left(\frac{2}{s}G + \frac{dG}{ds}\right)q_m'(s) - m(m+1)\frac{H}{s^2}q_m(s), \tag{2.85}$$

and the radial advection operators α_m, β_m, and γ_m are defined as follows:

$$\alpha_m(s) = \delta_{1m} + \frac{m}{2m-1}\cdot q_{m-1}(s) + \frac{m+1}{2m+3}\cdot q_{m+1}(s), \tag{2.86}$$

$$\beta_m(s) = \frac{m}{2m-1} \cdot q'_{m-1}(s) + \frac{m+1}{2m+3} \cdot q'_{m+1}(s), \tag{2.87}$$

$$\gamma_m(s) = \frac{m \cdot (1-m)}{2m-1} \cdot q_{m-1}(s) + \frac{(m+1) \cdot (m+2)}{2m+3} \cdot q_{m+1}(s). \tag{2.88}$$

The equations for $q_0(s)$ and $q_{m_{\max}}(s)$ are special cases, as they are at the boundaries of our finite series. The no flux and no long-ranged order boundary conditions in terms of the functions q_m are

$$\mathrm{Pe}\ L\left(\delta_{1m} + \frac{m}{2m-1} q_{m-1}(s) + \frac{m+1}{2m+3} q_{m+1}(s)\right) + G\ q'_m(s) = 0 \quad \text{at} \quad s = 2, \tag{2.89}$$

and

$$q_m \to 0 \quad \text{as} \quad s \to \infty. \tag{2.90}$$

The computational solution method, described previously in Khair and Brady [29], is as follows: the initial guess for the microstructure $f(\mathbf{s};\ \mathrm{Pe}_i)$ at the smallest value of Pe is guided by the linear-response analysis of Section 2.3. With this initial guess for f, the system of ODEs for $q_m(s;\ \mathrm{Pe}_i)$ is solved using the boundary-value problem solver `bvp4c` in `MATLAB`. The truncation value of the series $m_{\max}$ is initially set to 2 and is incremented until the solutions for each microviscosity contribution η_i^H, η_i^B and η_i^P change by less than 0.1% between $m_{\max}$ and $m_{\max+1}$. The solutions for $q_m(s;\ \mathrm{Pe}_i)$ are then used as the initial guess for the system $q_m(s,\ \mathrm{Pe}_{i+1})$ at the next largest Péclet number. The efficiency of the computational method hinges on the quality of the initial guess, making this bootstrapping technique critical when a large number $m_{\max}$ of terms are required for convergence of the microviscosity contributions.

Lastly, it should be noted that `bvp4c` solves boundary value problems on a finite domain. Thus, the far-field boundary condition, Equation 2.90, is set at some finite but large value of the radial separation $s_{\max}$. From the linear response analysis section, it was shown that, even at small Péclet numbers, the disturbance of the probe influences a region that is $O\left(\mathrm{Pe}^{-1}\right)$ far from the probe itself, indicating that $s_{\max}$ should be at least $O\left(\mathrm{Pe}^{-1}\right)$ for small Péclet numbers to capture the outer region of the microstructural disturbance. For large Péclet numbers, the depletion of probability density behind the probe forms a trailing wake of characteristic length $O(\mathrm{Pe})$, hence it is important for $s_{\max}$ to be at least this large.

2.5.2 Finite Difference Methods

For Péclet number $\sim O(10)$ and larger, so many terms are required in the Legendre polynomial expansion, that it becomes computationally intractable to simultaneously solve all coupled radial ODEs. Also, the magnitude of the pair distribution function changes most rapidly in a small boundary layer of thickness $\delta \sim O\left(\mathrm{Pe}^{-1}\right)$ on the anterior face of the probe. In this regime, it is useful to solve the Smoluchowski equation numerically via finite difference methods that concentrate grid

points in this region of most rapid change. We use the method detailed in Appendix B of the work of Khair and Brady [29]. The method is summarized as follows: beginning with the Smoluchowski equation in terms of the coordinates s and θ, we stretch the radial coordinate by the boundary layer thickness using the transform $y \equiv (s-2)/\delta = \mathrm{Pe}\,(s-2)$. With this transformation, the radial domain is now $y \in [0,\infty)$, which is mapped to the finite domain $t \in [0,1]$ using the coordinate transform

$$t = \exp\left[-\left(\omega + \frac{1-\omega}{1+y}\right) y\right]. \tag{2.91}$$

For a fixed discretization in the coordinate t, the parameter ω can be adjusted to set the maximum value of y in the interior domain of the grid, which is important to capture the trailing wake, a microstructural feature $\sim O\,(\mathrm{Pe})$ in length behind the probe. In terms of the coordinates t and θ, the Smoluchowski equation now reads

$$C_1 \frac{\partial f}{\partial t} + C_2 \frac{\partial^2 f}{\partial t^2} + C_3 \frac{\partial f}{\partial \theta} + C_4 \frac{\partial^2 f}{\partial \theta^2} + C_5 f = C_6, \tag{2.92}$$

where the coefficients C_α are as follows:

$$\begin{aligned}
C_1 &= L\cos\theta \frac{dt}{dy} + G\frac{\mathrm{d}^2 t}{\mathrm{d}y^2} + \mathrm{Pe}^{-1}\left(\frac{2G}{s} + \frac{\mathrm{d}G}{\mathrm{d}s}\right)\frac{\mathrm{d}t}{\mathrm{d}y}, \\
C_2 &= G\left(\frac{\mathrm{d}t}{\mathrm{d}y}\right)^2, \\
C_3 &= -\mathrm{Pe}^{-1}\frac{M\sin\theta}{s} + \mathrm{Pe}^{-2}\frac{H\cot\theta}{s^2}, \\
C_4 &= \mathrm{Pe}^{-2}\frac{H}{s^2}, \\
C_5 &= \mathrm{Pe}^{-1} W\cos\theta, \\
C_6 &= -\mathrm{Pe}^{-1} W\cos\theta.
\end{aligned}$$

The Smoluchowski equation is then discretized using a non-uniform grid spacing in t and in θ to concentrate grid points in regions where the most rapid change of the pair-distribution function is anticipated, namely near the boundary layer. Symmetry boundary conditions are employed at $\theta = 0$ and π while the radial boundary conditions of no long-ranged order and no flux are used at $t = 0$ and 1, respectively. By writing out the derivatives in Equation 2.92, which is discretized using second-order central differences, the resulting equation is of the form $Af = B$, where A is a pentadiagonal sparse matrix. This system of equations is solved in `MATLAB` using a `LAPACK` iterative banded solver. This solution method proves most useful for $\mathrm{Pe} \geq 10$.

2.6 Large Péclet Number

For very large Péclet number, the sharp microstructural gradients in the boundary layer on the anterior face of the probe and the long trailing wake behind the probe pose a challenge for discrete numerical methods. An analytical solution, for infinitely large Péclet numbers, and a boundary layer solution using matched asymptotic expansions are alternatives to the numerical approaches from Section 2.5. First, we will discuss the suspension microstructure when there is no Brownian motion at all, in which case the interesting result of a spherically symmetric microstructure is noted.

2.6.1 Infinite Péclet Number and Non-Brownian Systems

For non-Brownian suspensions, the governing equation for the suspension microstructure is strictly advective:

$$\mu\left(Wg_0 + L\frac{\partial g_0}{\partial s}\right) - \frac{M}{s}\left(\mu^2 - 1\right)\frac{\partial g_0}{\partial \mu} = 0. \tag{2.93}$$

In this limit, the suspended particles are unable to diffuse to dissipate gradients in the suspension microstructure. It is interesting to note that the order of the governing partial differential equation reduces by one for non-Brownian systems. Only one boundary condition, that of no long-ranged order in the dispersion, may be satisfied. The condition of no relative probability flux through the excluded-annulus separation cannot be met for the purely advective problem and hence a boundary layer is needed here in order to satisfy the condition of no flux. For now, we proceed with the solution outside of the boundary layer. Batchelor [5] had noted that the microstructure in this limit is spherically symmetric and depends only on the radial separation of probe and bath particles. The solution to Equation 2.93 is:

$$g_0\left(s\right) = \exp\left(\int_s^\infty \frac{W\left(z\right)}{L\left(z\right)}\mathrm{d}z\right) = \frac{1}{L\left(s\right)}\exp\left(\int_s^\infty \frac{2}{z}\left(1 - \frac{M\left(z\right)}{L\left(z\right)}\right)\mathrm{d}z\right). \tag{2.94}$$

At large separations , *i.e.* $s \gg 2$, Almog and Brenner [1] recognized that the twin multipole expansions of Jeffrey and Onishi are sufficient to determine the leading-order behavior of the microstructure;

$$g_0\left(s \gg 2\right) = 1 + \frac{30\lambda^3}{\left(1+\Delta\right)^4\left(1+\lambda\right)^4}s^{-4} + O\left(s^{-5}\right). \tag{2.95}$$

The far-field deviation from the equilibrium microstructure, *i.e.* the first term beyond unity in Equation 2.95, decays like s^{-4} and is proportional to λ^3 for very large probes and proportional to λ^{-1} for very small probes. For closer separations, e.g. $0.5 < s-2 \lesssim O\left(1\right)$, additional terms from the twin multipole expansions are required to obtain an accurate estimate for the integral in Equation 2.94. The analytic method of Almog and Brenner to evaluate g_0 at these moderate separations is as

follows: the quantity $g_0 L$ is expanded in powers of $(2/s)$

$$g_0 L \equiv \sum_{n=0}^{\infty} p_n(\lambda) \left(\frac{2}{\gamma s}\right)^n, \tag{2.96}$$

then, a recursive relation for each p_n can be obtained from Equation 2.94 using the coefficients of the twin multipole expansions of $L = \sum L_n(\lambda)(2/s)^n$ and $M = \sum M_n(\lambda)(2/s)^n$

$$p_n(\lambda) = -\frac{2}{n} \sum_{k=1}^{n} p_{n-k}(\lambda)\, \overline{g}_k(\lambda), \tag{2.97}$$

where

$$\overline{g}_n(\lambda) = M_n(\lambda) - \sum_{k=1}^{n} \overline{g}_{n-k}(\lambda)\, L_k(\lambda). \tag{2.98}$$

The initial terms must be defined for the recursion relations: $\overline{g}_0$ is equal to unity because of the limiting values of the hydrodynamic functions L and M at infinite separations, and $p_0 = 1$ in order for the microstructure to approach unity at infinite probe and bath particle separations to satisfy the condition of no long-ranged order.

For separations that are closer still, the lubrication forms of the mobility functions are required to assess the functional form of the microstructure. Recall that the functional forms for L and M for nearly-touching spheres, in which the radial coordinate $\xi \equiv s - 2 \ll 1$, are as follows:

$$L(\xi \ll 1, \lambda) = L_1(\lambda)\,\xi + L_2(\lambda)\,\xi^2 \ln \xi + L_3(\lambda)\,\xi^2 + O\left(\xi^3 \ln \xi\right), \tag{2.99}$$

$$M(\xi \ll 1, \lambda) = M_0(\lambda) + \frac{M_1(\lambda)}{\ln \xi^{-1} - z_1(\lambda)} + \frac{M_2(\lambda)}{\ln \xi^{-1} - z_2(\lambda)} + O(\xi \ln \xi). \tag{2.100}$$

Substituting these forms of the mobility functions into equation 2.94, the limiting behavior of the suspension microstructure near hydrodynamic contact can be obtained:

$$g_0(\xi \ll 1, \lambda) \sim A_0(\lambda)\, \xi^{(M_0 - L_1)/L_1} \left(\ln \xi^{-1} - z_1\right)^{-M_1/L_1} \left(\ln \xi^{-1} - z_2\right)^{-M_2/L_1}. \tag{2.101}$$

The value of the prefactor $A_0(\lambda)$ can be obtained for a specific size ratio λ by numerically integrating Equation 2.94 from infinity to a radial separation very close to hydrodynamic contact; Almog and Brenner [1] recommend this approach to obtain the pair-distribution function for $\xi < 10^{-6}$. For intermediate radial separations, $10^{-6} < \xi < 0.5$, in which the hydrodynamic functions L and M transition from being best approximated by the lubrication forms given in Equations 2.99 and 2.100 to the series expansions in powers of $(2/s)$, it is appropriate to instead expand the following function in powers of $(2/s)$,

$$g_0 L \tilde{\xi}^{-M_0/L_1} \left(\ln \tilde{\xi}^{-1} - z_1\right)^{-M_1/L_1} \left(\ln \tilde{\xi}^{-1} - z_2\right)^{-M_2/L_1}, \tag{2.102}$$

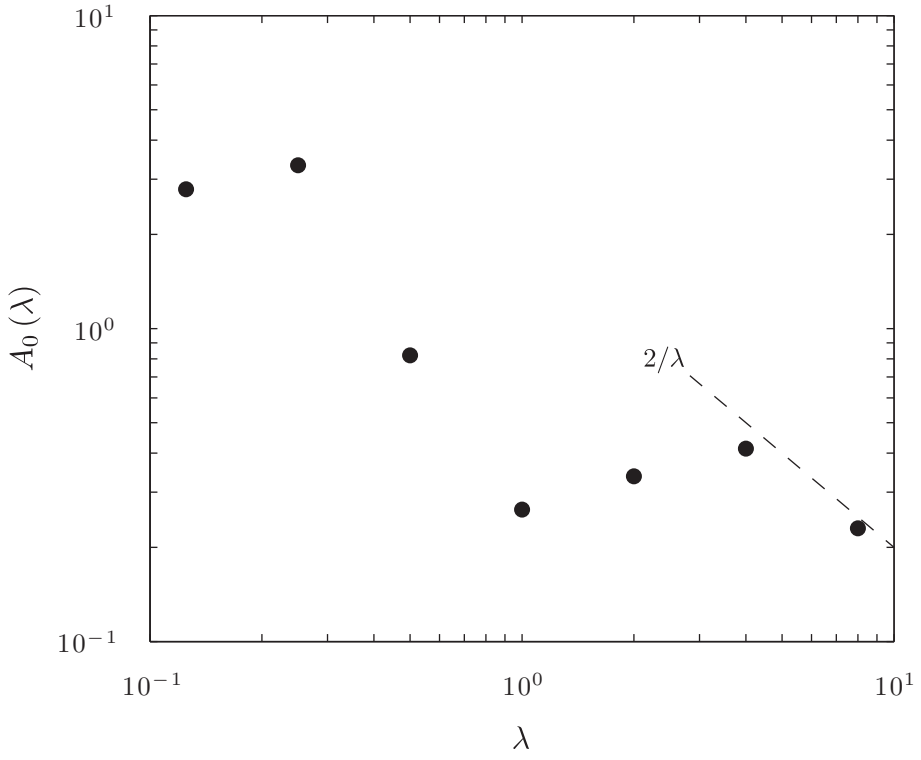

Figure 2.6: The value of the prefactor $A_0(\lambda)$ appearing in the expression for the near-field ($\xi \ll 1$) asymptotic form of the steady microstructure function g_0. The asymptote $A_0(\lambda) \sim 2/\lambda$ applies to large bath particles.

where the choice of $\tilde{\xi} = \xi/(1 + c\,\xi)$ remains analytic even as $s \to \infty$.

Alternatively, one may avoid the power series approximations of Almog and Brenner by numerically evaluating Equation 2.94 at any radial separation using adaptive Gauss-Kronrod quadrature, the function `quadgk` in `MATLAB`, which can handle both the semi-infinite domain of integration and the moderate singularity as $s \to 2$. This entirely numeric approach can yield values of the prefactor $A_0(\lambda)$ from Equation 2.101, as shown in Figure 2.6. To obtain the values of $A_0(\lambda)$, Equation 2.94 was integrated using `quadgk` from $\xi = 10^{-6}$ to infinity. To approximate the hydrodynamic functions L and M in this expression, twin-multipole expansions of Jeffrey and Onishi are used through powers of $2/s$ up to 300 for separations $s \geq 2.01$, while the lubrication forms of Kim and Karrila are used for values of $s < 2.01$. The resulting value of g_0 is then substituted into Equation 2.101 along with the value of ξ and the coefficients from the near-field approximations for L and M to obtain $A_0(\lambda)$. The termination at $\xi = 10^{-6}$ gives a sufficiently accurate approximation for A_0 for all values of λ tested, and further decreasing the lower bound for the integration as small as ξ=10^{-9} changed the approximations for $A_0(\lambda)$ by no more than 0.001%.

The values of $A_0(\lambda)$ exhibit nonmonotonicity in λ over the range of finite size ratios from $\lambda = 1/8$

to $\lambda = 8$. Beyond this finite range, for large λ, the coefficient $A_0(\lambda)$ approaches $2/\lambda$ owing strictly to the near-field form of the radial relative mobility function L. Note that for large λ, the first coefficient L_1 in the lubrication expansion for L is given by $(\lambda+1)^3/2\lambda^2$, which approaches $\lambda/2$ for small probes. Knowing this coefficient is important for calculating the hydrodynamic contribution to the intrinsic microviscosity for small probes for large Péclet numbers. For large probes, recall that we are unable to disturb the equilibrium microstructure and hence $g_0 = 1$ at all radial separations, indicating that $A_0 \to 1$ as $\lambda \to 0$.

2.6.2 Finite Péclet Number - Boundary Layer Solution

In real colloidal systems, arresting all thermal motion to arrive at an infinite Péclet number scenario is impossible. At best, the Péclet number will be large but still finite. Because the Péclet number is finite, there should be some small nondimensional distance $\delta \sim \mathrm{Pe}^{-1}$ near the surface of the probe particle over which gradients in the spherical microstructure can be dissipated by thermal motion. We rescale the dimensionless surface separation $\xi \equiv s-2$ by Pe^{-1} to arrive at the boundary layer coordinate $y \equiv \mathrm{Pe}^{-1}(s-2)$. Outside of the boundary layer, the purely advective solution for the microstructure from Section 2.6.1 still holds. Near the surface of the probe, radial diffusion of probability density, away from the probe, balances the advection of probability density toward the surface. This boundary-layer solution is discussed in detail in Appendix B for finite size ratios. The final form that we arrive at for the microstructure inside the boundary layer is

$$g_0(y,\mu) = A_0(\lambda)\ \Gamma\left(\frac{M_0}{L_1}\right)\ \left(\frac{\mathrm{Pe}}{Y(\mu)}\right)^{W_0/L_1}\ M\left(\frac{W_0}{L_1},\ 1,\ -\frac{y}{Y(\mu)}\right), \tag{2.103}$$

where Γ is the gamma function; $L_1,\ G_1,\ M_0$ and W_0 are the leading-order coefficients in the lubrication expansions of the respective hydrodynamic mobility functions, $Y(\mu)$ is the boundary layer thickness as a function of angular position $\mu = \cos\theta$ as measured from the direction of mean motion, and M here is the Kummer function, a confluent hypergeometric function which decreases monotonically in y from unity at $y = 0$. This boundary-layer expression for g_0 matches the asymptotic behavior of the outer solution (equation 2.101) as $y \to \infty$. The boundary-layer thickness is a monotonically increasing function of μ, increasing from $Y = G_1/L_1$ at $\mu = 1$. The expression for Y as a function of μ is

$$Y(\mu) = \frac{2G_1}{M_0}\left(1-\mu^2\right)^{-L_1/M_0}\int_\mu^1 \left(1-\xi^2\right)^{W_0/M_0}\mathrm{d}\xi. \tag{2.104}$$

Note that the maximum value of the pair-distribution function $g_{0,\max}$ occurs at $y = 0$ and $\mu = 1$, in the compression boundary layer along the line of applied force. So we can predict the microstructural

scaling behavior with large Pe:

$$g_{0,\max} = A_0(\lambda)\,\Gamma\left(\frac{M_0}{L_1}\right)\left(\frac{\mathrm{Pe}}{G_1/L_1}\right)^{W_0/L_1}. \tag{2.105}$$

The values of $g_{0,\max}$, as found by the finite difference solutions of Section 2.5.2, are plotted in Figure 2.7 as a function of Pe. The slight variations in the slopes of the curves for different λ are a result of the different scaling exponents with different size ratio from Equation 2.105. The maximum value of g_0 appears to grow with decreasing probe particle size, indicating that more and more probability density accumulates on the front face of a small probe. An explanation for this feature is that advection lateral to the surface of a very large probe particle happens much more readily than advection toward the probe face. Thus, when a small bath particle diffuses out of this boundary layer region back into the advection-dominated outer region, that bath particle will more easily advect past the probe than reenter the boundary layer region where its relative mobility is most hindered. However, once a large bath particle diffuses outside of this boundary layer region of hindered mobility, if it is on the anterior face of the probe, it will readily advect right back into the boundary layer as the radial relative mobility for large bath particles is unhindered.

In order to collapse the small-probe curves in Figure 2.7, the limiting behavior of the prefactor $A_0\Gamma(M_0/L_1)$ as a function of λ should be considered. In the limit of small probe particles, $\lambda \to \infty$, the ease of relative motion of the probe past a large bath particle, *i.e.* M_0, scales like λ^{-1}, but the coefficient L_1 multiplying the ξ term in the lubrication expansion for the relative mobility along the line of centers is proportional to λ. The ratio of the two functions thus is $O\left(\lambda^{-2}\right)$ small. The gamma function of a small argument goes like the inverse of the argument, so $\Gamma(M_0/L_1) \sim \lambda^2$. As was shown in Figure 2.6, the coefficient A_0 is equal to $2/\lambda$ for small probes, and so the prefactor in Equation 2.105 is proportional to λ. By normalizing the $g_{0,\max}$ versus Pe curves by λ, they collapse onto a single curve as seen in Figure 2.8, with slight variations in the slope owing to differences in the divergence of the relative mobility near contact W_0.

The applicability of the form of the boundary layer solution, Equation 2.103, for small probes is brought into question when visualizing the boundary layer thickness function $Y(\mu)$ for successively smaller probes as seen in Figure 2.9. Khair and Brady [29] recognized that the boundary layer solution fails on the rear face of the probe when the boundary layer thickness function $Y(\mu)$ diverges. A second boundary layer with respect to the angular coordinate μ defines the coalescence region of probability density behind the probe. In this angular boundary layer of thickness $1/\mathrm{Pe}$ about $\mu = -1$, relative diffusion laterally along the probe face balances advective motion. However, the divergence of Y on the posterior face of the probe, for negative μ, appears to happen more and more rapidly with decreasing probe size, increasing λ, until eventually, when the probe is infinitesimally small, the boundary layer thickness diverges at $\mu = 0$. In this limit of small probe particle, $W_0 \approx L_1 = \lambda/2$

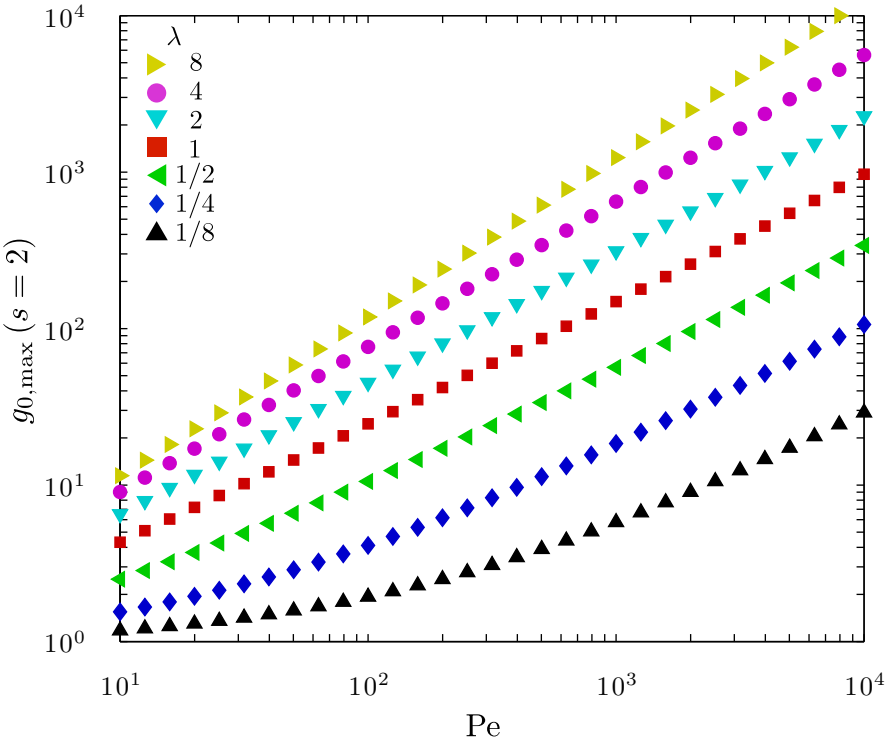

Figure 2.7: The maximum value of the steady microstructure at contact $g_0(s=2)$ as a function of Péclet number for various bath-to-probe particle size ratios. This maximum value occurs parallel to the applied external force on the anterior face of the probe. These values were computed for an excluded annulus parameter $\Delta = 10^{-5}$.

and Kummer's function $M(1,1,-y/Y(\mu)) = \exp(-y/Y)$, which no longer matches with the outer solution in Equation 2.101 for large y. A separate matched asymptotic solution for small probes is presented in Appendix C, where the results are applicable for the boundary layer on only the anterior face of the probe. In this appendix, we do find a leading-order exponentially-decaying boundary layer,

$$g_0(y,\mu;\ \mathrm{Pe} \gg 1, \lambda \gg 1) = \mathrm{Pe}\lambda\left[\frac{4}{3}\mu\exp(-\mu y)\right] + O(\mathrm{Pe}). \tag{2.106}$$

Matching to the outer solution happens at $O\left(\mathrm{Pe}\lambda^{-1}\right)$ in the perturbation expansion. This boundary layer solution leads to the hydrodynamic piece of the intrinsic microviscosity η_i being equal to λ, which is exactly $1/2$ the perceived viscosity predicted by Davis and Hill [16] at infinite Péclet numbers for small sedimenting spheres. The reason for this $1/2$ discrepancy is resolved when considering the truly infinite Péclet versus large-but-finite Péclet problems. When the Péclet number is infinite, as was explained earlier the microstructure about the probe particle becomes spherically symmetric and the boundary layer does not diverge at $\mu = 0$. However, for the large but finite Péclet number, once all the bath particle probability density reaches the rear face of the probe, should a bath particle

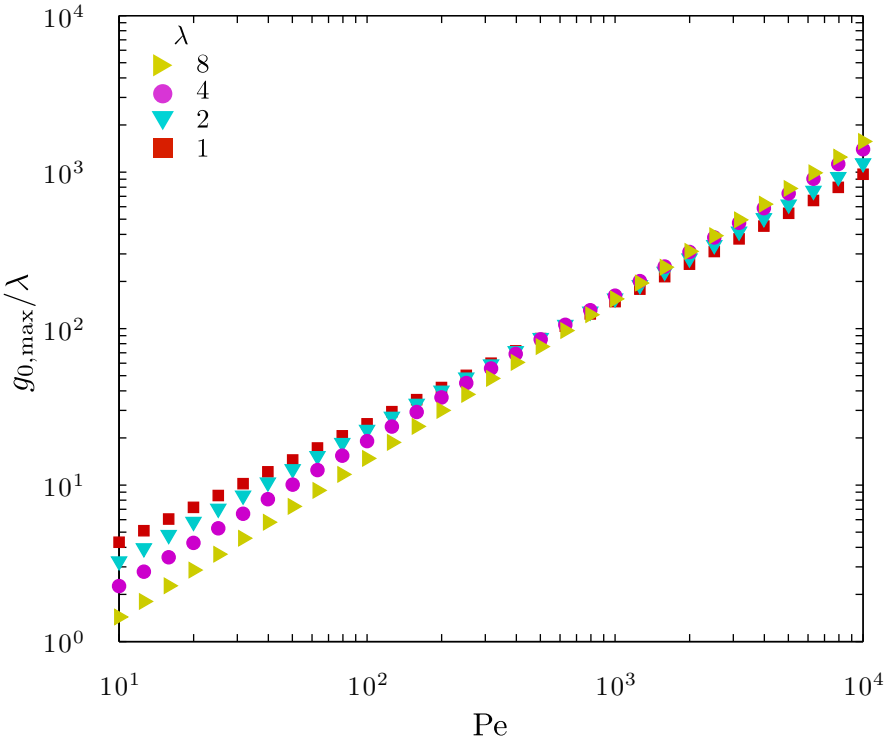

Figure 2.8: The maximum value of the steady microstructure at contact g_0 normalized by the bath-to-probe particle size ratio λ as a function of Péclet number. These values were computed for an excluded annulus parameter $\Delta = 10^{-5}$.

diffuse outside of the lubrication boundary layer, advection will never return it to the surface and it advects away from the probe instantaneously along a trajectory parallel to $\mathbf{u}$, the vector along the line of constant applied external force. Thus, the rear face of the probe thus a depletion region and only the compressional/pushing piece of the intrinsic microviscosity is present; the extensional/dragging piece would contribute the other half of the intrinsic microviscosity as predicted by Davis and Hill.

This leads us to the following question: how large would the Péclet number need to be in order to achieve a spherically symmetric microstructure about a small probe? Even for probes of the same size as the bath particles, Khair and Brady showed that the force thickening of the hydrodynamic contribution of the intrinsic microviscosity is very slow to reach the high-Péclet limiting value. From the outer region, there is an $O\left(\mathrm{Pe}^{0}\right)$ contribution to η_i^H owing to the long-ranged hydrodynamic interactions. Inside the boundary layer of thickness $O\left(\mathrm{Pe}^{-1}\right)$, we see from Equation 2.105 that the magnitude of the microstructure scales as $O\left(\mathrm{Pe}^{W_0/L_1}\right)$. The product of the boundary layer thickness and the magnitude of the microstructure in side the boundary layer indicates that there is an $O\left(\mathrm{Pe}^{W_0/L_1-1}\right)$ contribution to η_i^H, where $W_0/L_1 - 1$ is equal to $-M_0/L_1$. Recall that for small probe particles, $M_0 \sim \lambda^{-1}$ and $L_1 \sim \lambda$, so the inner region contributes $O\left(\mathrm{Pe}^{-1/\lambda^2}\right)$. Khair

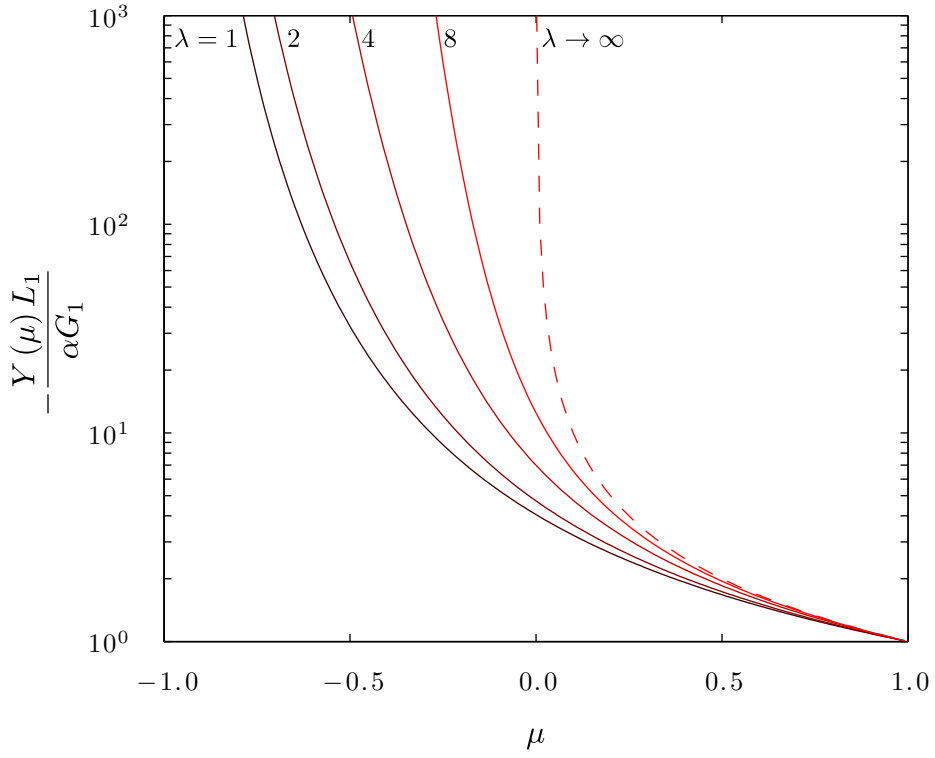

Figure 2.9: Boundary layer thickness $Y(\mu)$ normalized by its value at the leading edge of the probe $Y(\mu = 1) = -\alpha G_1/L_1$ for several size ratios λ

and Brady [29] found the approach toward a limiting microviscosity to go like $\eta_i^H \sim \alpha - \beta \mathrm{Pe}^{-M_0/L_1}$. Thus we can expect the second term to vanish for small probes when $\mathrm{Pe} \gg \exp\left(\lambda^2\right)$, emphasizing how strong the external force must be to achieve a spherically symmetric microstructure.

2.7 Results and Discussion

The suspension microstructure g_0 is visualized in Figure 2.10. The Péclet number increases down the figure from the linear response regime in the top row down to the highly nonlinear microstructures in the bottom row. The relative radii of the bath particles are 1/8, 1, and 8 times that of the probe in the first three columns, respectively. Each microstructure figure is normalized such that the maximum value of the steady microstructure g_0 corresponds to red, the equilibrium value $g_0 = 1$ corresponds to green, and the minimum value corresponds to blue. The hydrodynamic size of the probe particle is depicted with the blue circle, and the volume excluded to the bath particle centers is denoted by the white annulus about the probe. In the fourth column, the excluded annulus parameter is infinite, indicating that the bath and probe particles interact only by collisions at the excluded-volume radius. Each microstructure plot has a side length of $5r_{\min} = 5(a+b)(1+\Delta)$

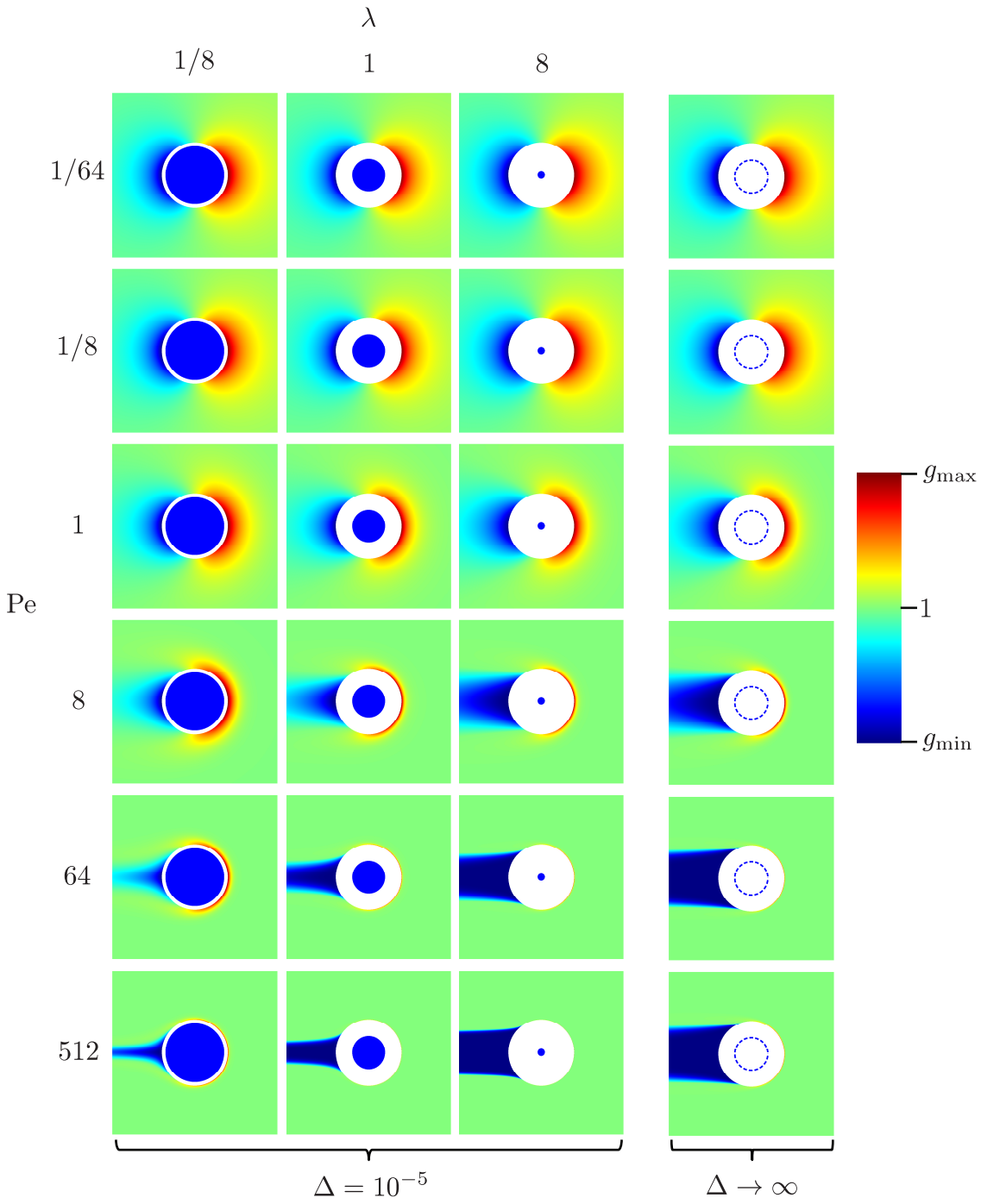

Figure 2.10: The microstructure function $g_0(\mathbf{r})$ visualized for various Péclet numbers and particle size ratios. The side length of each visualized microstructure is $5r_{\min} = 5(a+b)(1+\Delta)$. For the three leftmost columns, the excluded annulus parameter is 10^{-5} to represent full hydrodynamics, while in the rightmost column the excluded annulus parameter approaches infinity. The color values for each microstructure are normalized according to the same color bar. The solid blue circle in the center of each microstructure represents the hydrodynamic radius of the probe particle while the white annulus represents the volume excluded to the bath particles. On the right, the dashed blue line represents the fact that all probe-bath interactions are excluded-volume in nature.

Some interesting features of the microstructures are the fore-aft symmetry in the low Péclet microstructures across all size ratios. The two symmetric accumulation and depletion lobes are characteristic of a diffusive dipole. With increasing Péclet number, the accumulation region in front of the probe compresses toward the minimum approach distance while the depletion region behind the probe coalesces and lengthens into a wake. Eventually, when the Péclet number is large, an $O\left(\mathrm{Pe}^{-1}\right)$ thick boundary layer on the leading edge of the probe houses nearly all the probability density. The magnitude of the maximum value in the boundary layer grows with λ as was shown in Figure 2.7. By normalizing each microstructure plot to the same colorbar as described above, the boundary layers for smaller probes appear thinner at the same value of the Péclet number, even though the thickness is $O\left(\mathrm{Pe}^{-1}\right)$ regardless of the probe to bath particle size ratio.

The most notable qualitative change with increasing size ratio is the broadening of the trailing wake with increasing bath particle size. This should make intuitive sense - the change in the relative mobility is small from that when hydrodynamic interactions are neglected due to an applied external force on a small probe, so once a bath particle diffuses out from the boundary layer on the surface of the probe particle, it will advect away parallel to the applied external force. However, when a small bath particle diffuses out of the accumulation boundary region into the purely advective region, its relative mobility along the line of centers is still $O(\Delta)$ small compared with its relative mobility transverse to the line of centers; advective effects outside of the boundary layer contribute to the pinching off of the trailing wake for small bath particles.

Comparisons of microstructures between different particle size ratios λ and different Péclet numbers Pe can be difficult. The Péclet number $\mathrm{Pe} \equiv F_0 b\,(1+\Delta)\,/2kT$ contains the excluded-annulus bath particle size as its characteristic length scale. Thus, if one were to conduct active microrheology experiments at a fixed temperature T where the size of the bath particles and the strength of the applied external force acting on the probe were held constant while the size of the probe particle is varied, plots of constant Pe can be compared. However, if the size of the *probe* particle and the strength of the applied external force are held constant, and the bath particle sizes are varied, plots of constant $\mathrm{Pe}/\lambda = F_0 a\,(1+\Delta)\,/2kT$ should guide the expectations. It is this second case that corresponds with falling-ball rheometry; the gravitational potential energy and the size and relative density of the falling ball dictate the ratio Pe/λ. Looking at Figure 2.10 along a downward-sloping diagonal of constant Pe/λ, it can be seen that decreasing the bath particle size for a given probe will always shift the behavior toward the linear-response regime, in which we recover Einstein's viscosity correction for infinitesimally small bath particles. At the same time, we observe that by increasing the size of the bath particles for a fixed probe size, the trailing wake lengthens and broadens, indicating that the microstructure will not converge on a spherically symmetric form for falling-ball rheometry with a fixed probe size.

We now turn our attention to the microviscosity results as computed from these suspension

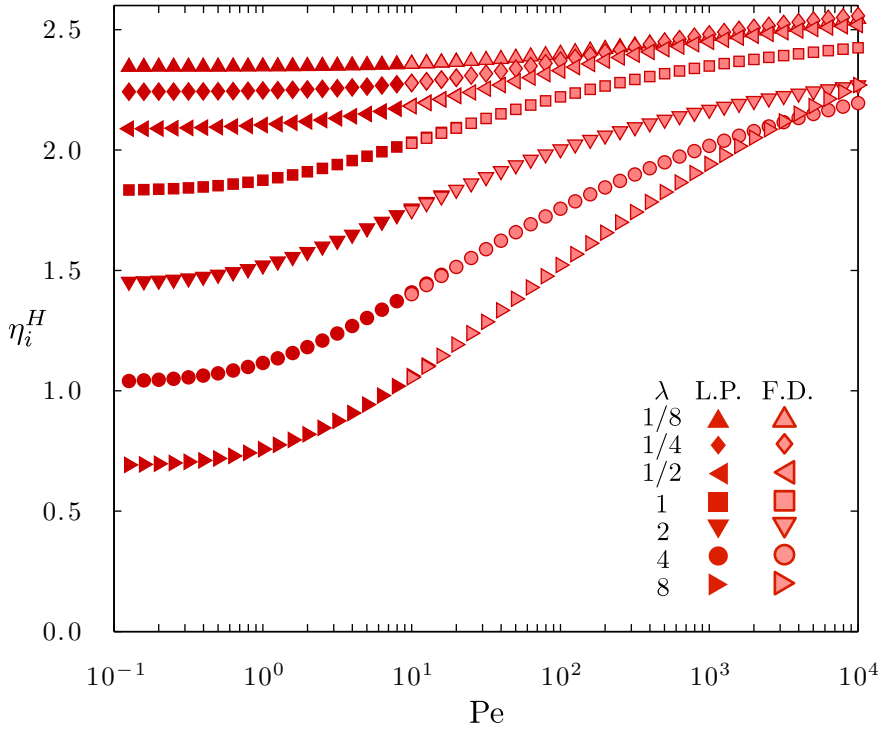

Figure 2.11: The hydrodynamic contribution η_i^H to the intrinsic microviscosity as a function of Péclet number Pe for finite size ratios λ ranging from $1/8$ to 8. For Péclet numbers up to 10, the microstructures were computed using the Legendre polynomial method of Section 2.5.1, while for Péclet numbers greater than 10 the finite-difference methods of Section 2.5.2 were employed. These results are for a small excluded annulus parameter $\Delta = 10^{-5}$.

microstructures. In Figure 2.11, the hydrodynamic contribution to the intrinsic microviscosity is plotted as a function of Péclet number for an excluded annulus parameter $\Delta = 10^{-5}$ meant to approximate full hydrodynamic interactions. We see that force thickening with increasing Péclet number is a universal phenomenon; the hydrodynamic contribution grows with increasing applied external force for all finite size ratios. The extent of force-thickening increases with decreasing probe particle size, and this leads to interesting nonmonotonicity in η_i^H at large Pe as a function of λ, for example the crossing of the η_i^H curves of $\lambda = 4$ and $\lambda = 8$ when the Péclet number is $O\left(10^3\right)$. The increasingly slow approach toward a limiting value of η_i^H for larger and larger λ as mentioned in the boundary layer discussion of Section 2.6.2 is also seen in these η_i^H curves.

In Figure 2.12, the Brownian contribution to the intrinsic microviscosity η_i^B is plotted as a function of Pe at this same excluded annulus parameter of $\Delta = 10^{-5}$. The Brownian contribution, which is most significant for small probes at small Pe, exhibits force thinning from its maximum value in the limit of purely diffusive probe motion. Recall in Section 2.3.2, it was found that the maximum value of the Brownian contribution to the intrinsic microviscosity is $1/2$ for $\lambda \to \infty$

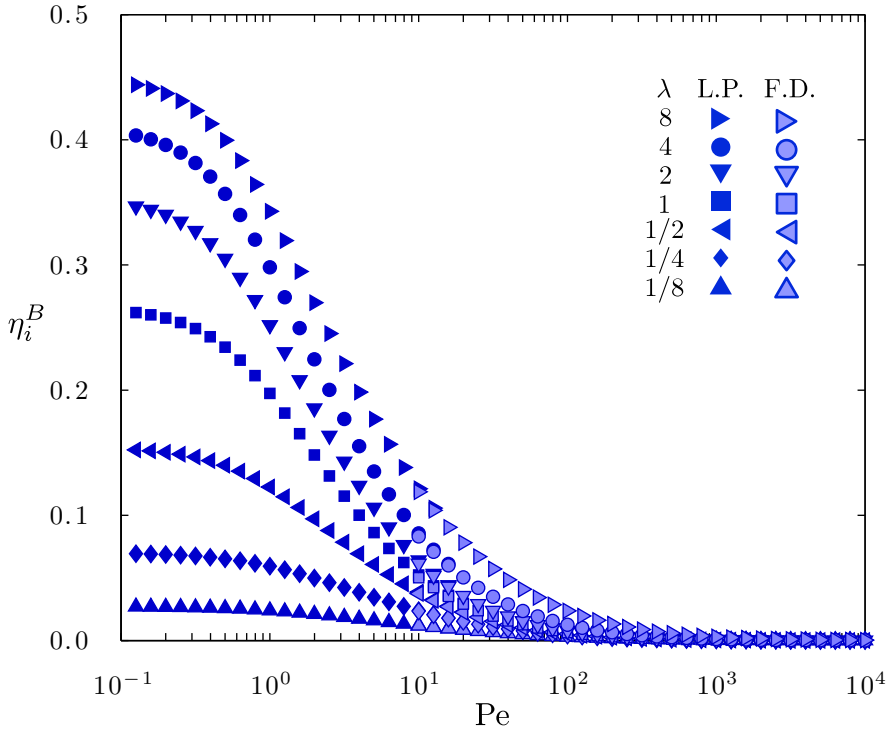

Figure 2.12: The Brownian contribution η_i^B to the intrinsic microviscosity as a function of Péclet number Pe for finite size ratios λ ranging from 1/8 to 8. For Péclet numbers up to 10, the microstructures were computed using the Legendre polynomial method of Section 2.5.1, while for Péclet numbers greater than 10 the finite-difference methods of Section 2.5.2 were employed. These results are for a small excluded annulus parameter $\Delta = 10^{-5}$.

as long as lubrication interactions between the probe and bath particle are not excluded. The extent of force thinning of η_i^B at low to moderate Pe is initially greater than the force-thickening phenomenon seen in the hydrodynamic contribution to the intrinsic microviscosity. However, for moderate to large Pe the force thickening observed in the hydrodynamic contribution becomes the dominant factor in shaping the microrheological response. We see the transition from force-thinning to force thickening for the total intrinsic microviscosity occur around Pe $\sim O(1)$ in Figure 2.13. The total intrinsic microviscosity η_i also includes the interparticle contribution η_i^P which scales with the excluded annulus parameter Δ as shown in Appendix D. The nonmonotonicity of η_i becomes more and more prominent for $\lambda \gg 1$. In the limiting case of $\lambda \to 0$, the intrinsic microviscosity becomes independent of Péclet number and is equal to 5/2 for any applied external force, consistent with the Einstein viscosity correction for a dilute dispersion of spheres. For $\lambda \to \infty$ and $\Delta = 0$, we expect the low Pe limit of the total intrinsic microviscosity to be 1/2 , which it force thickens to a large Pe microviscosity of λ as predicted in Appendix C. Additionally, the Δ-dependence of each of the microviscosity contributions is shown in several figures in Appendix D.

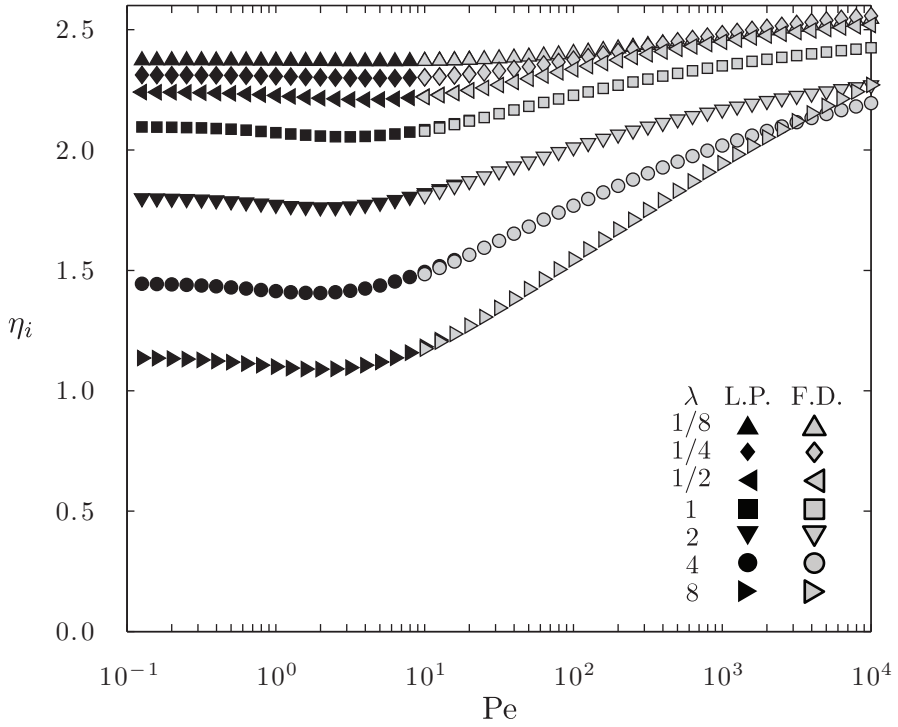

Figure 2.13: The total of the hydrodynamic, Brownian, and interparticle contributions $\eta_i = \eta_i^H + \eta_i^B + \eta_i^P$ to the intrinsic microviscosity as a function of Péclet number Pe for finite size ratios λ ranging from 1/8 to 8. For Péclet numbers up to 10, the microstructures were computed using the Legendre polynomial method of Section 2.5.1, while for Péclet numbers greater than 10 the finite-difference methods of Section 2.5.2 were employed. These results are for a small excluded annulus parameter $\Delta = 10^{-5}$.

The problem of active and nonlinear microrheology has been examined classically in the sedimentation literature. Batchelor [5, 7, 6], together with Wen [8], studied sedimentation in polydisperse systems of rigid spheres. In the work, gravity provides the driving external force for motion, and the density ratio $\gamma \equiv (\rho_j - \rho) / (\rho_i - \rho)$ characterizes the rate of sedimentation of the "probe" species with density ρ_i through a collection of "bath" species with density ρ_j, both of which are dispersed homogeneously throughout Newtonian solvent of density ρ and viscosity η. By examining their analysis with a density ratio $\gamma = 0$, we have nearly a direct comparison to our problem of active microrheology through a neutrally buoyant suspension. A distinction may still be found in the choice of boundary condition imposed due to the rigidity of the spheres. Batchelor observed that the advective flux along the line of centers approaches zero as the radial separation between the test sphere and a background sphere approaches the sum of their hydrodynamic radii. This makes intuitive sense: in most introductory fluid mechanics classes, one learns that an infinite force is required to bring two rigid spheres into contact with one another due to the strength of lubrication interactions, so with

a finite constant applied force, two spheres may never be brought into contact with one another. Consequently, the diffusive flux must also approach zero as the surface separation approaches zero. In his work, Batchelor constrains the normal component of the diffusive particle flux to equal zero at hydrodynamic contact. In the work presented in this thesis, we approach the limit of full hydrodynamic interactions by making the excluded annulus parameter smaller and smaller, but still finite. When the excluded annulus potential acts at a finite distance from the hydrodynamic radius, we must impose a boundary condition of no net flux, comprising both advective and diffusive motion. This underscores the singular nature of the limit of full hydrodynamic interactions: it is important to consider the order in which limits are taken for the governing parameters Δ, λ, and Pe.

It is useful to consider the limits of particle size ratio for which the results of Batchelor's sedimentation analysis best correspond with this study of microrheology. When the relative velocity due to an applied external force approaches zero much more rapidly than the relative diffusivity, the boundary conditions of no normal component of the diffusive flux and no normal component of total flux resemble one another for finite Δ. Said differently, for values of the ratio $L/G \to 0$, Batchelor's sedimentation problem and the microrheology problem for small-but-finite excluded annuli are identical. In Figure 2.14, the ratio L/G is plotted versus the surface separation for different size ratios λ. We see that when the relative probe size is dominant ($\lambda \to 0$) the ratio L/G approaches zero as the surface separation distance approaches zero, and the sedimentation and microrheology problems are most identical. Once the bath particles have finite size, however, the ratio L/G approaches a finite value. The larger L/G becomes, the more of a discrepancy we can expect between the results of the sedimentation and microrheology analyses. In fact, once the bath particles become larger than the probe particle ($\lambda > 1$) relative motion parallel to the line-of-centers due to the applied external force is hindered less than relative diffusion. The maximum value of L/G for nearly-touching spheres occurs for a size ratio λ between 1 and 4. The ratio eventually approaches unity again when the relative bath size is dominant ($\lambda \to \infty$).

Batchelor and Wen present their findings in terms of a sedimentation coefficient S_{ij}, defined as the $O(\phi_j)$ correction to the mean velocity, or the negative of what we call the intrinsic microviscosity η_i. In the limiting cases of asymptotically small ($\lambda \gg 1$) or large ($\lambda \ll 1$) probes, Batchelor predicted that the sedimentation coefficient becomes independent of the relative strength of gravitational potential energy versus the thermal energy (*i.e.* independent of the Péclet number) and behaves as follows:

$$S_{ij}(\lambda) = \begin{cases} -\frac{5}{2} - \gamma + O(\lambda), & \lambda \ll 1; \\ -\gamma\left(\lambda^2 + 3\lambda + 1\right) + O\left(\lambda^{-1}\right), & \lambda \gg 1. \end{cases} \tag{2.107}$$

Einstein's viscosity correction is evident in equation 2.107 for large probes. It is for large probes that the bath particles and solvent together resemble a continuum to the probe particle with effective

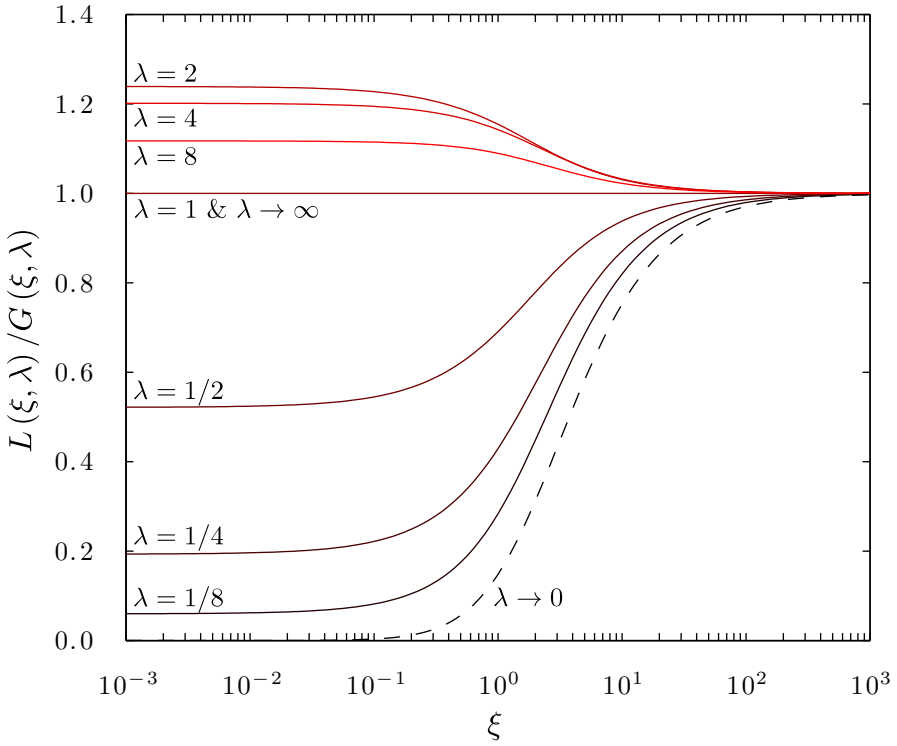

Figure 2.14: The ratio of the hydrodynamic functions L and G as a function of dimensionless radial separation distance $\xi \equiv s - 2$ for several bath-to-probe particle size ratios λ. The relative probe size decreases with increasing curve brightness. The curves of L/G for $\lambda = 1$ and $\lambda \to \infty$ are coincident and equal to unity for all radial separations.

viscosity $\eta\,(1 + (5/2)\,\phi_j)$. All other leading-order contributions to the sedimentation coefficient, for small and large particles, are nonzero only when the bath particles are not neutrally buoyant. This prediction of invariance in Pe is not seen for small probe particles in the limit where the finite excluded annulus is made smaller and smaller. Even for neutrally-buoyant bath particles, with full consideration of hydrodynamic interactions, the intrinsic microviscosity for large λ force-thickens from a low Pe limiting value of $\eta_i = 1/2$ to a high Pe limiting value of $\eta_i \sim \lambda$.

For this chapter, we first focused on the behavior for small perturbations from equilibrium. That is to say, how would sedimenting particles behave when gravitational potential energy is weak compared to thermal energy and the Péclet number is much less than unity? At small Péclet number, Batchelor decomposes the sedimentation coefficient into a linear function of γ, *i.e.*

$$S_{ij}\,(\lambda, \gamma;\ \mathrm{Pe} \ll 1) = S'_{ij}\,(\lambda;\ \mathrm{Pe} \ll 1) + \gamma S''_{ij}\,(\lambda;\ \mathrm{Pe} \ll 1)\,, \tag{2.108}$$

as the system is a perturbation of an equilibrium system. The relevant coefficient to examine is S'_{ij} as it corresponds with neutrally-buoyant background particles. In a corrigendum [6], Batchelor gives

an empirical relation for S'_{ij} at small Pe (*c.f.* eq II. 5.5),

$$S'_{ij}\left(\lambda;\ \mathrm{Pe} \ll 1\right) = \frac{-2.5}{1+0.16\lambda}, \tag{2.109}$$

indicating that the sedimentation coefficient decays from Einstein's viscosity correction for large probes to zero for small probes. Again, this empirical model must be modified slightly for the problem of active microrheology for a finite excluded annulus; small probes will still be hindered slightly from their mean velocity in pure solvent even at low Pe. Lastly, it should be noted that the intrinsic microdiffusivity contributions discussed in Section 2.2 could also be computed by similar numerical schemes in order to understand how the applied external force changes the diffusive behavior of a Brownian probe particle.

Chapter 3

Hydrodynamic Interactions and the Motion of Catalytic Nanomotors

3.1 Introduction

Contemplating the motion of microorganisms has intrigued fluid mechanicians for quite some time. The self-propulsion of microorganisms is unique from most of the aquatic animal kingdom since inertia is unreliable as a propulsion mechanism on micron and smaller length scales. Reversible sequences of motion, such as oscillating caudal fin motion in fish, are effective in high-Reynolds number environments, such as water. These motions would prove futile in viscous conditions, such as in glycerol: the Navier-Stokes equations are linearized in the inertialess regime, causing reciprocal movements to yield no net motion [21]. Breaking symmetry is the key to achieving net motion in an inertialess environment, and asymmetry becomes a useful design principle when considering how to construct a nanoscale "motor". By deforming its shape in an irreversible sequence, a microswimmer is capable of translating through its environment. Taylor [53] studied the self-propulsion, energy dissipation, and the stress on undulating sheets due to purely viscous forces, in an effort to understand how flagellating motion of spermatozoa can still provide net motion on the micron scale. Purcell [43] incorporated a sequence of movements into his three-link swimmer that is not identical when reversed and thus is one of the simplest toy models for a deforming body achieving self-propulsion.

Symmetry breaking to provide propulsion can be achieved not only by the body of the microswimmer itself deforming, but also through inducing a change in the local chemical environment. It is to these "catalytic nanomotors" where we direct our attention in this chapter. Paxton *et al* [42] observed the motion of nanorods comprising gold and platinum segments through aqueous solutions of hydrogen peroxide. The gold ends are inert while the platinum ends catalyze the decomposition of aqueous hydrogen peroxide to water and oxygen. A bubble propulsion mechanism where the ejection of oxygen bubbles acts as thrust, successful in describing the motion of similar experiments on the millimeter length scales [24], would indicate that the rods translate through the aqueous solution

along their axis away from the catalytic platinum face. However, these nanorods travel through the suspension toward the platinum segments. A diffusiophoretic model with a gradient of oxygen molecules also predicts the reverse direction of motion away from the platinum segments, and so Paxton *et al* explain the movement as driven by varying interfacial tension.

In other work from the group of Ayusman Sen, Pavlick *et. al.* [41] observed the motion of gold-silica Janus particles onto which the Grubbs ring-opening metathesis polymerization (ROMP) catalyst is grafted. Norbornene monomers are consumed and polymerized at the silica face, creating a norbornene chemical potential gradient driving the motor toward the depletion region. These motors were found to sense and move up externally-imposed gradients of norbornene, exhibiting chemotactic behavior not normally seen in non-living systems. Motion via polymerization is witnessed in living systems such as in the generation of new actin filaments at the leading edge of epithelial keratocytes to transport the cytoskeleton backward toward the nucleus [54], or production of actin filament "comet tails" in *Listeria* bacteria [55] whose mechanisms have been described in a force-dipole generating hydrodynamic model [34].

Applications of catalytic nanomotors have been proposed with the towing of therapeutic payloads in mind. Other "nanocars" have employed surface-initiated ROMP to drive and transport small cargo along a substrate [20]. Over long times compared with the timescale τ_R for Brownian rotation, Janus particles can exhibit a greater effective diffusivity D_{eff} than that which is possible through Brownian motion of inert particles alone. The motor follows a "run-and-tumble" trajectory where each "run" segment happens over a time much shorter than the timescale for Brownian rotation of the colloidal Janus particle, and the effective diffusivity resembles $D_{\text{eff}} = D_0 + U^2/6D_{\text{rot}}$ where U is the motor velocity and D_{rot} is the rotary diffusivity of the particle [22]. This enhanced diffusivity could increase the rate that therapeutic-towing nanoparticles disperse throughout an injection site. Further details of synthetic self-propelling nanomotors may be found in the reviews by Ebbens and Howse [18], Wang [58], and Mirkovic *et al* [38].

Some questions remain unanswered in the description of mechanisms of autonomous motion from a colloidal-level description. When the motor interacts with the solute particles hydrodynamically, what is the limiting velocity of the motor? How does the reactant sense a disturbance from a translating motor? What is the optimal ratio of inert to active faces for a Janus particle motor when the solute is infinitesimally small? What design considerations come into play for motors that are not much larger than the reactant fuel species? A study by Sharifi-Mood *et al* [48] has examined the motion of a colloidal motor particle interacting with reactive species for a variety of interparticle interactions, including van der Waals and exponential reactions, when the reactant species has no finite size. Solute of finite size has a different expression for relative diffusion, and a non-isotropic relative diffusive flux changes the spatiotemporal evolution of the reactant microstructure about translating motors.

The model system that we choose to investigate is a colloidal-level analysis based on the osmotic propulsion model employed by Córdova-Figueroa and Brady [13], [14]. In these works, solute reactant molecules are treated as colloidal species dispersed throughout a Newtonian, viscous, constant property solvent. Some concerns, from a continuum-level analysis, arose over whether motion can arise from local solute gradients ([26], [27]), but the colloidal-level treatment of solute matches the continuum-level analysis in the appropriate limits as shown by Brady [10]. The purpose of this chapter is to explore, in more detail, concepts proposed in the autonomous motion section of Brady's work on particle motion driven by solute gradients. In particular, when the reactant and product species are thought of as colloidal particles dispersed throughout a continuum solvent, the velocity field created by the motion of the motor should alter the trajectories of reactant and product past the motor. We start by highlighting key features of the autonomous motion problem statement in Section 3.2. For a detailed introduction to the problem at hand, the curious reader is referred to sections 4 and 5 of the work of Brady [10]. Future work in preparation by Brady will discuss the proper treatment of advection in autonomous motion.

3.2 Problem Statement

Consider a collection of rigid, spherical, neutrally-buoyant colloidal reactant particles R of hydrodynamic radius b immersed in a Newtonian, viscous, constant property solvent of density ρ and dynamic viscosity η. Among the reactant particles is situated a rigid, spherical catalytic "motor" particle of hydrodynamic radius a. The size of the motor relative to the size of the reactant is arbitrary and is set by the ratio $\lambda \equiv b/a$. The crux of the catalytic nanomotor problem is to determine how the motor induces a local chemical potential gradient about its surface and consequently travels through the dispersion with some mean phoretic velocity $\langle \mathbf{U} \rangle$ of magnitude U. The chemical potential gradients are achieved by means of an asymmetric distribution of reactive and unreactive surface area on the motor, *i.e.* the motor is a Janus particle with catalytic and inert faces. To systematically tune the fraction of catalytically-active surface area, the polar angle θ_s or the "switch angle" is introduced. For polar angles $0 \leq \theta \leq \theta_s$ as measured from the direction of mean motion, the surface of the motor catalyzes the irreversible conversion of reactant R into product P with some stoichiometric ratio ϑ,

$$R \rightarrow \vartheta P. \tag{3.1}$$

For polar angles $\theta_s < \theta \leq \pi$, the surface of the osmotic motor is inert. For micron-sized colloidal particles in a solvent comparable to water at room temperature, the Reynolds number $\mathrm{Re} \equiv \rho U a/\eta$ describing the relative magnitude of inertial to viscous forces is $\sim O\left(10^{-6}\right)$, setting our problem in the regime of Stokes flow. We should note that in the Stokes flow regime, the hydrodynamic force becomes infinite when bringing two rigid spheres into contact at their hydrodynamic radii. Thus, a

surface-mediated reaction cannot occur between colloids without attractive interparticle interactions if the particles are required to come into hydrodynamic contact. The excluded-annulus interparticle potential alleviates this issue of infinite forces preventing contact, with the additional benefit of introducing a parameter that can easily "tune" the strength of hydrodynamic interactions between the reactant particles and the catalytic motor. This potential $\Phi(\mathbf{r})$ is spherically symmetric and depends only on the relative separation $r \equiv |\mathbf{r}|$ of the catalyst and reactant particle centers. The potential is a Heaviside step function preventing the particles from approaching any closer than $r_{\min}$,

$$\Phi(\mathbf{r}) \equiv \begin{cases} 0, & r \geq r_{\min}; \\ \infty, & r < r_{\min}. \end{cases} \tag{3.2}$$

We define the minimum approach distance $r_{\min} \equiv (a+b)(1+\Delta)$, where Δ is the excluded-annulus parameter. The limit of fully-screened hydrodynamic interactions corresponds with $\Delta \to \infty$, while full hydrodynamic interactions are modeled by setting $\Delta = 0$. Note that both motor and reactant can have excluded annulus character on either of their surfaces, as depicted in figure 3.1. The excluded annulus parameter for the system is related to the excluded volumes of the motor and reactant by

$$\Delta \equiv \frac{\Delta_a a + \Delta_b b}{a+b}. \tag{3.3}$$

Reactant and product particles can have different effective hydrodynamic radii and hence different diffusivities. In order to simplify the system, we assume the following for the ratio of the diffusivity of the product, D_P, to the diffusivity of the reactant, D_R

$$\frac{D_P}{\vartheta D_R} \to \infty. \tag{3.4}$$

If this ratio were finite, one would only need to add a factor of $(1 - \vartheta D_R/D_P)$ to the resulting diffusiophoretic force as shown by Córdova-Figueroa and Brady [14]. Because of the large discrepancy in the diffusivities, product effectively disappears upon reaction, and the reaction may be thought of as a "consumption" reaction. An alternative picture would be to think of the rigid reactant particles as a collection of bound solvent monomers, and the catalytic reaction severs the bonds in the reactant particle, hence dissolving it. Thus, the product particle does not need to be accounted for in this model. The rate of consumption is given by $r_R h_s(\theta)$, where r_R is the reactant consumption rate, and the surface catalyst geometry is described by the function $h_s(\theta)$, a Heaviside step function using the switch angle θ_s

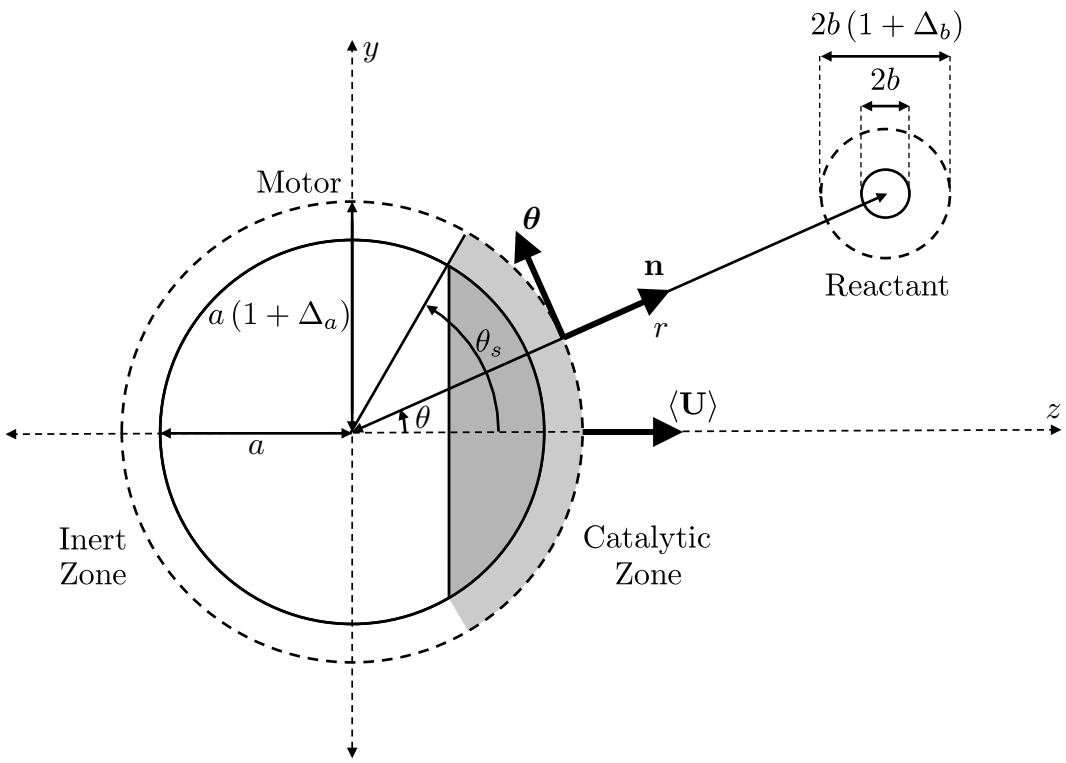

Figure 3.1: The motor-reactant geometry for the catalytic nanomotor problem. Note that the catalytic zone is symmetric about the azimuthal angle ϕ.

$$h_s(\theta) = \begin{cases} 1, & 0 \leq \theta \leq \theta_s; \\ 0, & \theta_s < \theta \leq \pi. \end{cases} \tag{3.5}$$

The reaction is offset from the hydrodynamic radius of the motor to occur at the minimum approach distance $r_{\min}$ used in the definition of the interparticle potential Φ. Unless explicitly noted, the switch angle is taken to be at $\theta_s = \pi/2$ so that the Janus particles have equal parts reactive and inert faces.

The net propulsive force on the motor is dependent on the microstructure, or configuration, of the surrounding reactant. The reactant microstructure is quantified by the pair distribution function $g(\mathbf{r})$, describing the likelihood of finding a reactant particle at some spatial location $\mathbf{r}$ relative to the motor. The pair distribution function is defined as the ratio $g(\mathbf{r}) \equiv P_{1|1}(\mathbf{r}|\mathbf{x}_1)/n_b^\infty$: the conditional probability density $P_{1|1}(\mathbf{r}|\mathbf{x}_1)$ of finding a reactant particle at some position $\mathbf{r}$ relative to the motor center given that the motor is centered about $\mathbf{x}_1$ over the number density n_b^∞ of reactant molecules in the quiescent, undisturbed suspension. Correctly solving for this steady-state pair distribution function, which is governed by the time-invariant Smoluchowski equation, allows for the prediction the diffusiophoretic velocity. The derivation for the dilute Smoluchowski equation with careful consideration of hydrodynamic interactions, becomes more complex when the

advective motion requires solute-motor collisions; the dilute treatment used in the microrheology problem derivation is insufficient. For a discussion of why three-body interactions are needed, and a derivation of the Smoluchowski equation relevant for diffusiophoretic motion, the reader is referred to recent work by Brady.

The advective term that appears in the steady Smoluchowski equation describing the motion of the catalytic nanomotor is more complex than that which governs constant-force microrheology. Only the coupling between the force monopole acting on the probe particle and the relative translational motion needed consideration for microrheology. However, in diffusiophoretic motion the motor is force free as one should expect for any type of phoretic motion. All higher moments, force dipole, force quadrupole, *etc.* contribute to the advective motion of reactant past the motor. In addition, the mobility functions appearing in the advection terms require averaging over three-body ensembles. However, the leading order diffusive motion of the reactant is still described by the same relative diffusivity tensor $\mathbf{D}_{\text{rel}} \equiv kT\left(\mathbf{M}_{22}^{UF} - \mathbf{M}_{21}^{UF} - \mathbf{M}_{12}^{UF} + \mathbf{M}_{11}^{UF}\right)$ as for microrheology. Thus, in the limit of small Péclet number, the governing equation for the reactive bath particles is simply

$$\boldsymbol{\nabla}_{\mathbf{r}} \cdot \mathbf{D}_{\text{rel}} \cdot \boldsymbol{\nabla}_{\mathbf{r}} g = 0. \tag{3.6}$$

The excluded-annulus interparticle potential prevents particles from approaching any closer than their excluded-volume radius allows. The only probability flux normal to the surface is that defined by the consumption reaction on the reactive face of the motor

$$-\mathbf{n} \cdot \mathbf{D}_{\text{rel}} \cdot \nabla_{\mathbf{r}} g = r_R h_s\left(\theta\right) \quad \text{at } r = r_{\min}. \tag{3.7}$$

In Equation 3.7, $\mathbf{n}$ is the outward-facing unit normal oriented along the line of centers from the motor to the reactant particle. Far from the motor, the concentration field should not sense the presence of the motor; thus, the conditional probability density of finding a reactant particle far from the motor should approach the ambient number density of reactant

$$g\left(\mathbf{r}\right) \to g_{\text{eq}} \quad \text{as } r \to \infty. \tag{3.8}$$

Because of the excluded-annulus interparticle potential and the diluteness of the reactant solution, the equilibrium value g_{eq} of the pair distribution function is equal to unity for all radial separations $r > r_{\min}$.

For our model of a surface-mediated reaction, a reaction that is first-order in the concentration of reactant is the intuitive choice, indicating that motor-reactant collisions facilitate the production

of product. We may thus define the reaction rate r_R in terms of the pair-distribution function

$$r_R \equiv -\kappa n_b^{\infty} g\left(\mathbf{r}\right), \tag{3.9}$$

where κ is the reaction velocity. Alternative scenarios, for example a surface-generation model, in which therapeutic molecules diffuse from a hydrogel carrier particle, may be better suited to a zero-order reaction rate.

The choice to non-dimensionalize the radial coordinate is based on the minimum approach distance $r_{\min}$,

$$\tilde{s} \equiv \frac{r}{r_{\min}}. \tag{3.10}$$

The resulting velocity of the motor with a given distribution of reactant comprises both interparticle and Brownian contributions,

$$\left\langle \mathbf{U}_1 \right\rangle = \left\langle \mathbf{U}_1^P \right\rangle + \left\langle \mathbf{U}_1^B \right\rangle. \tag{3.11}$$

The interparticle contribution to the motor motion is a surface integral at the excluded annulus contact distance,

$$\left\langle \mathbf{U}_1^P \right\rangle = -n_b^{\infty} D_a \left(r_{\min}\right)^2 L\left(r = r_{\min}, \lambda\right) \oint_{\tilde{s}=1} \mathbf{n}\; g\left(\tilde{\mathbf{s}}\right)\; \mathrm{d}\Omega. \tag{3.12}$$

The Brownian contribution to the motor motion is the divergence of the relative mobility weighted by the likelihood of the configuration averaged over all space,

$$\left\langle \mathbf{U}_1^B \right\rangle = -n_b^{\infty} D_a \left(r_{\min}\right)^2 \int_{\tilde{s}\geq 1} g\left(\tilde{\mathbf{s}}\right)\; \nabla_{\tilde{\mathbf{s}}} \cdot \hat{\mathbf{M}}_r\; \mathrm{d}\tilde{\mathbf{s}}. \tag{3.13}$$

In Equation 3.12, the function $L\left(r = r_{\min}, \lambda\right)$ is simply the value of the relative mobility hydrodynamic function L evaluated at the minimum approach distance between the motor and reactant molecule, $r_{\min}$. The relative mobility functions depend on the reactant-to-motor particle size ratio $\lambda \equiv b/a$. Recall that L describes the ease of relative motion along the line of centers between the motor and reactant when a force acts solely on the motor, while M describes the facility of tangential motion. That is to say, the relative mobility tensor $\hat{\mathbf{M}}_r$ may be written as,

$$\hat{\mathbf{M}}_r \equiv 6\pi\eta a \left(\mathbf{M}_{11}^{UF} - \mathbf{M}_{12}^{UF}\right) = L\mathbf{nn} + M\left(\mathbf{I} - \mathbf{nn}\right), \tag{3.14}$$

where $\mathbf{n}$ is the outward-facing unit vector along the line of centers between the motor and reactant particles, and $\mathbf{I}$ is the identity tensor. The function $L\left(r_{\min}, \lambda\right)$ increases monotonically with Δ for all λ, from 0, when $\Delta = 0$, to 1, when $\Delta \to \infty$. In the limiting case of very small reactant ,$\lambda \ll 1$, the relative mobility functions L and M need not consider lubrication for a certain limit: if we examine the limit where the size of the additional excluded annulus distance Δa is greater than the size of

the reactant particles b, the gap size between the reactant and motor particles will be large enough, even at center-to-center separations of $r_{\min}$, so that lubrication effects need not be considered, as depicted on the left-hand side of Figure 3.2. It is in this regime that the relative mobility functions L and M take on the following simple functional forms for all accessible motor and reactant particle configurations,

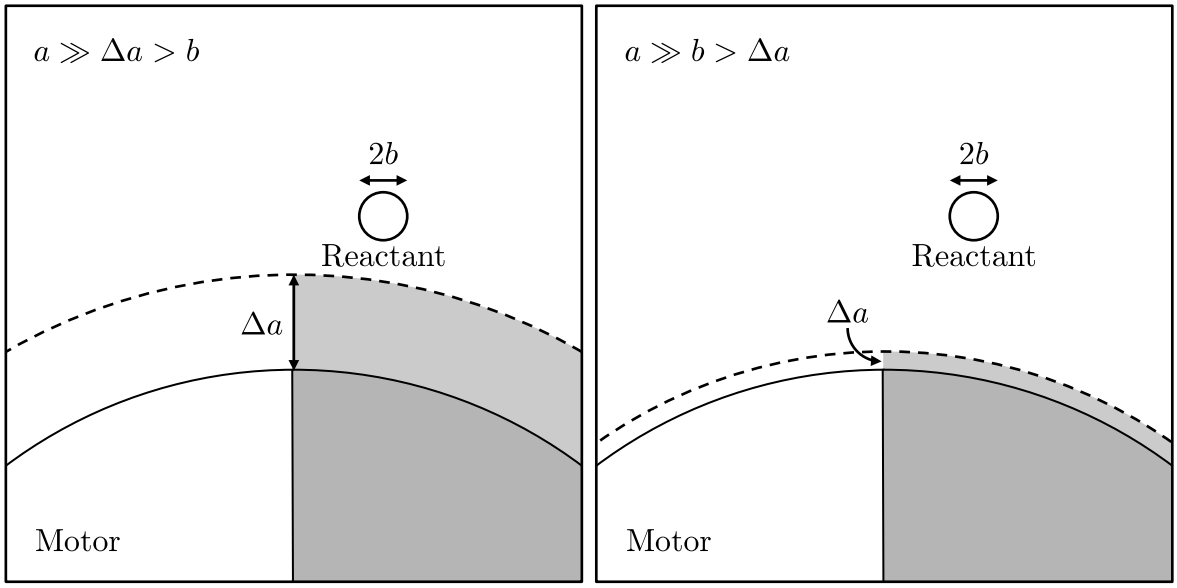

Figure 3.2: The possible limits of small reactant and small excluded annulus length scales. *Left*: When the excluded annulus is larger than the radius of the reactant particle, the lubrication regime in which the gap is the smallest length scale is inaccessible. *Right*: The excluded annulus is smaller than the radius of the reactant and the simple functional forms of L and M proposed in this work do not hold for all center-to-center separations.

$$L\left(\tilde{s},\ \lambda \ll 1\right) = 1 - \frac{3}{2\left(1+\Delta\right)}\tilde{s}^{-1} + \frac{1}{2\left(1+\Delta\right)^3}\tilde{s}^{-3} + O\left(\lambda\right) \tag{3.15}$$

$$M\left(\tilde{s},\ \lambda \ll 1\right) = 1 - \frac{3}{4\left(1+\Delta\right)}\tilde{s}^{-1} - \frac{1}{4\left(1+\Delta\right)^3}\tilde{s}^{-3} + O\left(\lambda\right). \tag{3.16}$$

Note that the limit where the bath particle radius is the smallest length scale in the problem corresponds to the ratio $\Delta/\lambda > 1$. If the excluded annulus thickness were the smallest length scale in the problem, as seen in the right-hand side of Figure 3.2, then Equations 3.15 and 3.16 would not be valid approximations in the lubrication regime, defined by $\tilde{s} - 1 \ll 1$. It is important to note that, for small reactant particles, the divergence of the relative mobility $\nabla \cdot \hat{\mathbf{M}}_r$ scales as $O\left(\lambda^3\right)$ for all radial separations, indicating that the Brownian contribution to the motor velocity, *i.e.* equation 3.13, is negligible.

When also considering advection effects, we arrive at the following partial differential equation

and boundary conditions:

$$\tilde{\mathrm{Pe}}\ \left\langle \hat{\mathbf{U}}_{\mathrm{rel}}\left(g\right)\right\rangle \cdot \nabla g\left(\tilde{\mathbf{s}}\right) + \nabla \cdot \mathbf{D}_{\mathrm{rel}} \cdot \nabla g\left(\tilde{\mathbf{s}}\right) = 0 \tag{3.17}$$

$$g \to 1 \quad \text{as } \tilde{s} \to \infty \tag{3.18}$$

$$\tilde{\mathrm{Pe}}\ \left\langle \hat{\mathbf{U}}_{\mathrm{rel}}\left(g\right)\right\rangle \cdot \mathbf{n}\ g\left(\tilde{\mathbf{s}}\right) + \frac{\partial g}{\partial \tilde{s}} = \tilde{\mathrm{Da}}\ h_s\left(\theta\right) g\left(\tilde{\mathbf{s}}\right) \quad \text{at } \tilde{s} = 1 \tag{3.19}$$

We use the same dimensionless groups to characterize the relative rates of advection, diffusion, and reaction as defined in the problem posed by Brady [10]: the Péclet $\left(\tilde{\mathrm{Pe}}\right)$ and Damköhler $\left(\tilde{\mathrm{Da}}\right)$ numbers. The timescale for advection of the catalytic nanomotor to occur on the order of its excluded-volume size is $\tau_a \equiv a\left(1+\Delta\right)/U$, the timescale for the reaction rate to occur at the surface of the motor is $\tau_r \equiv a\left(1+\Delta\right)/\kappa$, and the timescale for the bath particles to diffuse to fill in the trailing wake behind the motor is is $\tau_d \equiv \left(a\left(1+\Delta\right)\right)^2/D_R$. The Péclet number may be interpreted as the ratio of diffusive and advective timescales,

$$\tilde{\mathrm{Pe}} \equiv \frac{\tau_d}{\tau_a} = \frac{U\ a\left(1+\Delta\right)}{D_R}, \tag{3.20}$$

while the Damköhler number may be thought of as the ratio of diffusive and reactive timescales,

$$\tilde{\mathrm{Da}} \equiv \frac{\tau_d}{\tau_r} = \frac{\kappa\ a\left(1+\Delta\right)}{D_R}. \tag{3.21}$$

We will assume that the reactant microstructure about the motor is at a steady state. In other words, as the catalytic nanomotor constantly reacts with the particles around it, the microstructure remains fully developed. If we were to include Brownian rotation, the result would be a random, as opposed to a directed, walk. Brownian rotation would cause the long-time effective diffusivity of the motor to be

$$D_{motor} = D_a + \frac{1}{6}\frac{U^2}{D_{\mathrm{rot}}}, \tag{3.22}$$

where D_a is the diffusivity of the motor in the absence of Brownian rotation, U is the velocity of the motor, and $D_{\mathrm{rot}} \sim kT/8\pi\eta a^3$ is the rotary diffusivity. Brownian rotation can be ignored when the time scale for the concentration profile to develop, $\tau \sim a^2/D_R$, is short compared to the rotary diffusion time, $\tau_{\mathrm{rot}} \sim 1/D_{\mathrm{rot}}$. Since $\tau/\tau_{\mathrm{rot}} \sim b/a$, Brownian rotation can be ignored in the small-λ regime where $\lambda = b/a \ll 1$ as long as the time of observation of the motor is shorter than the timescale for rotation. For finite size ratios, Brownian rotation happens rapidly enough that a steady-state concentration profile may not have enough time to develop about the motor. To consider steady motion that is still governed by Equations 3.17 through 3.19 in the limit of finite

motor sizes, one can imagine a scenario where the rotational degrees of freedom are constrained. For example a physically-tethered motor protein may be capable of translating along a surface but may not be free to change its orientation. Motor particles with a dipole magnetic moment could also align with an externally applied field while still not applying an external force.

For the remainder of this section, we examine Equations 3.17 through 3.19 in the linear-response regime where the Péclet number is much less than unity. In this limit, ensemble-averaged three body hydrodynamic interactions and the complicated dependence of the relative velocity $\left\langle \hat{\mathbf{U}}_{\mathrm{rel}}\left(g\right)\right\rangle$ on all moments of the microstructure function g are neglected, as only the leading-order diffusive effects described by $\mathbf{D}_{\mathrm{rel}}$ change the character of the microstructure. We examine the Brownian and interparticle velocity contributions for a half-reactive motor ($\theta_s = \pi/2$) of various relative sizes of reactant and motor. Future directions for this colloidal approach to understanding autonomous motion, including proper consideration of advection, are highlighted.

3.3 Preliminary Results and Future Directions

The motor velocity comprises Brownian and interparticle contributions, which take on the forms in Equations 3.12 and 3.13. The magnitude of the interparticle contribution to the translational velocity is plotted as a function of the reactivity $\tilde{\mathrm{D}}\mathrm{a}$ of the motor in figures 3.3, 3.4, and 3.5 for successively smaller excluded annulus parameters of Δ =1, 0.1, and 0.01 respectively. As we can see, the motor velocity reaches a high $\tilde{\mathrm{D}}\mathrm{a}$ limiting velocity, at which point the value of the reactant microstructure is ~ 0 on the reactive face of the motor and $O\left(1\right)$ on the inert face. We see that decreasing the excluded annulus parameter always has the effect of reducing the maximum attainable velocity of the motor as a result of interparticle interactions, as the contribution $\left\langle \mathbf{U}_1^P\right\rangle$ is proportional to the value of the relative translational mobility function L evaluated at the minimum approach distance. Since L is a monotonically increasing function of Δ for all size ratios, it is expected that the interparticle velocity should decrease when the reactive zone moves closer and closer to the hydrodynamic radius of the motor. The hydrodynamic function L scales as Δ^2 for small Δ and small reactant, indicating that for very small λ it would be appropriate to scale the dimensionless value of $\left\langle \mathbf{U}_1^P\right\rangle$ by Δ^2. For larger reactant, namely $\lambda \sim O\left(1\right)$, the hydrodynamic function L scales as Δ.

The Brownian contribution to the motor velocity increases with decreasing excluded annulus parameter as seen by comparing Figures 3.6 and 3.7. This is because the magnitude of the divergence of the relative mobility W grows with decreasing Δ, and the Brownian contribution is the dipolar moment of the microstructure weighted by the divergence of the relative mobility. However, for large motors ($\lambda \to 0$) as discussed by Brady [10] the motor velocity will be strictly due to interparticle interactions at the excluded-annulus radius because the divergence of the relative mobility is proportional to λ^3 for large motors.

This study of properly incorporating hydrodynamic interactions into the diffusiophoretic motion of a catalytic particle from a colloidal perspective is still in a nascent stage. Future directions include considerations of three-body hydrodynamic interactions to properly incorporate advective effects into the reaction-diffusion Smoluchowski equation. Because the translational velocity of the motor is the result of reactant-motor collisions, the Péclet number is not concentration-independent, as it was in the case of active and nonlinear microrheology. Thus, conserving all terms of $O(\phi_b)$ in the Smoluchowski equation requires consideration of a third reactant particle properly averaged over all accessible configurations between the motor and the two reactant particles. Eventually, once the motion of a single catalytic nanomotor, interacting hydrodynamically with the reactive solute, is understood, these results can be extended to a study of the interaction of multiple catalytic nanomotors with each other. This could yield insights into unique phenomena such as dynamic clustering of reactive colloids, as seen in the work of Theurkauff *et. al.* [56]. Understanding the motion of multiple nanomotors in concert with one another is critical when using motors as towing mechanisms or drug delivery vehicles as it is unlikely that only a single microscopic motor will be administered at a time.

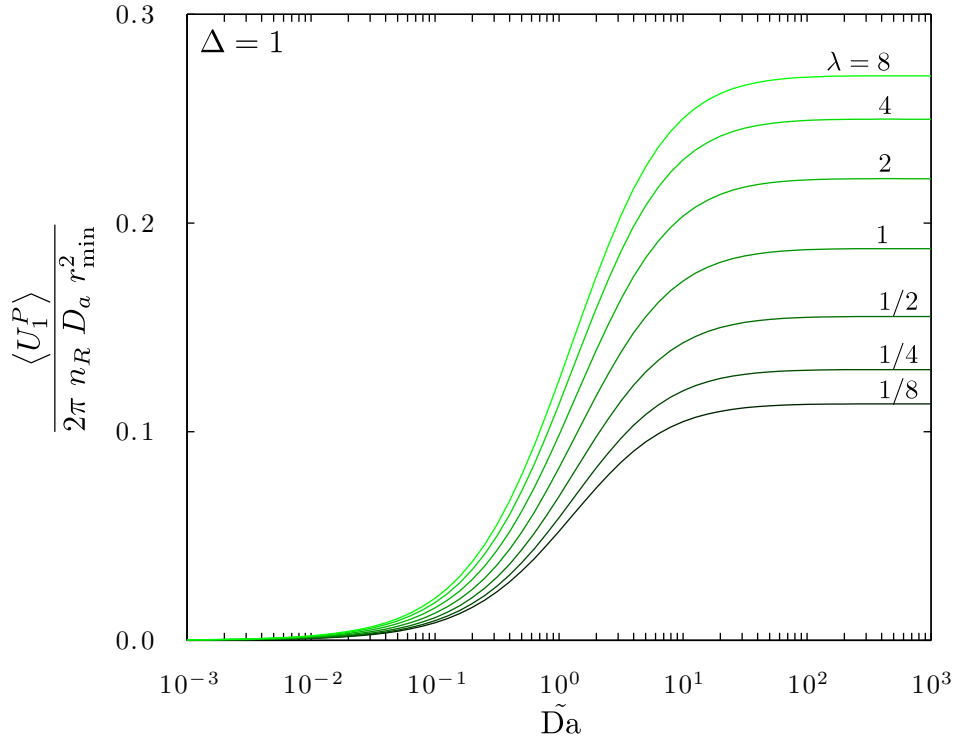

Figure 3.3: The interparticle contribution to the motor velocity normalized by the reactant number density, the motor diffusivity, and the minimum approach distance for an excluded annulus parameter of $\Delta = 1$ for various reactant to motor particle size ratios $\lambda \equiv b/a$ as a function of Damköhler number.

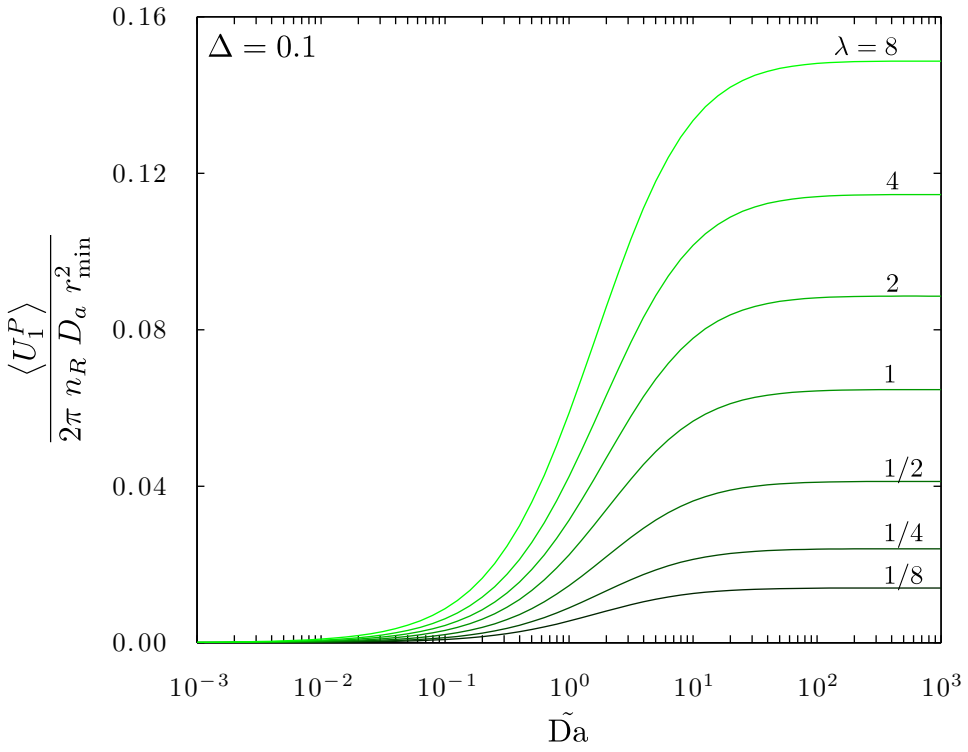

Figure 3.4: The interparticle contribution to the motor velocity normalized by the reactant number density, the motor diffusivity, and the minimum approach distance for an excluded annulus parameter of $\Delta = 0.1$ for various reactant to motor particle size ratios $\lambda \equiv b/a$ as a function of Damköhler number.

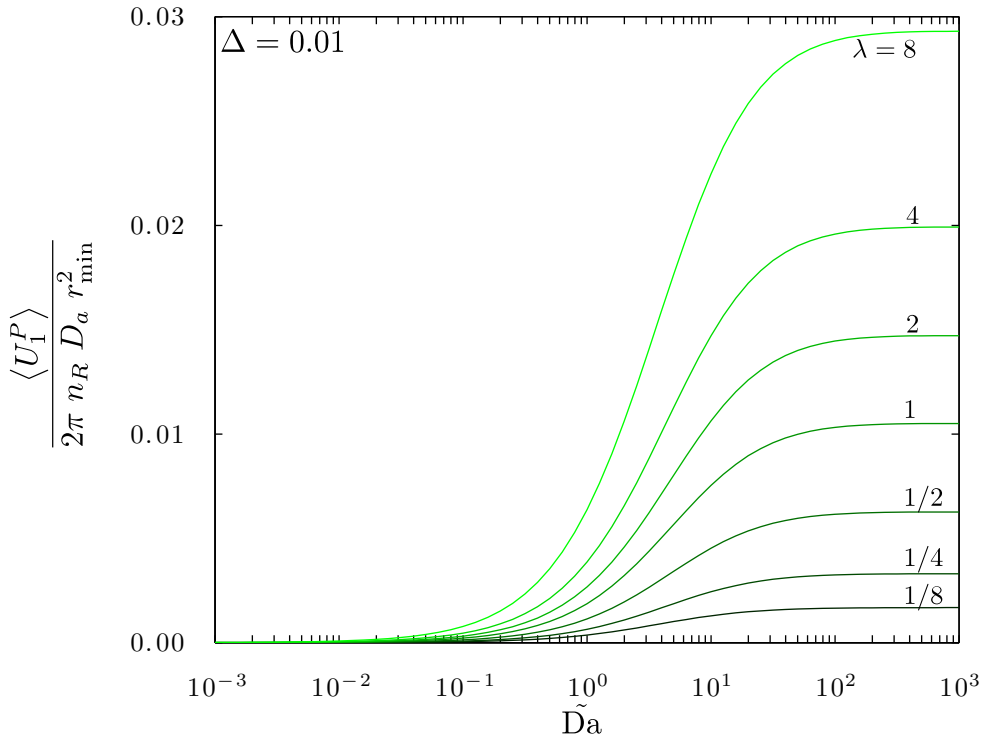

Figure 3.5: The interparticle contribution to the motor velocity normalized by the reactant number density, the motor diffusivity, and the minimum approach distance for an excluded annulus parameter of $\Delta = 0.01$ for various reactant to motor particle size ratios $\lambda \equiv b/a$ as a function of Damköhler number.

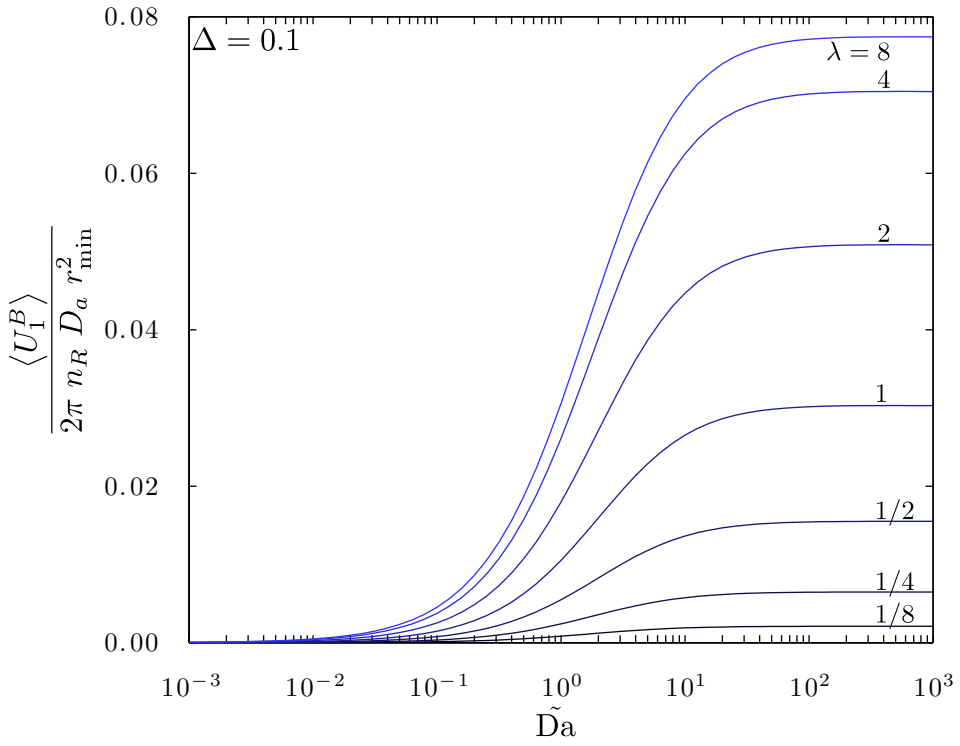

Figure 3.6: The Brownian contribution to the motor velocity normalized by the reactant number density, the motor diffusivity, and the minimum approach distance for an excluded annulus parameter of $\Delta = 0.1$ for various reactant to motor particle size ratios $\lambda \equiv b/a$ as a function of Damköhler number.

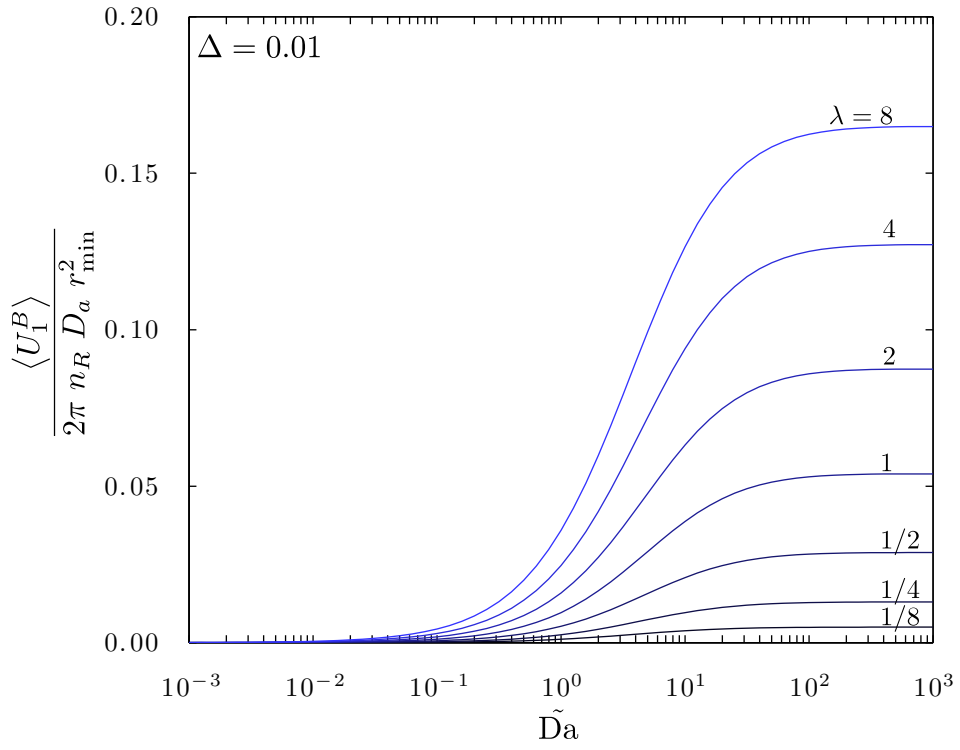

Figure 3.7: The Brownian contribution to the motor velocity normalized by the reactant number density, the motor diffusivity, and the minimum approach distance for an excluded annulus parameter of $\Delta = 0.01$ for various reactant to motor particle size ratios $\lambda \equiv b/a$ as a function of Damköhler number.

Appendix A

Linear Response Equations for the Microstructure and Deflection Field

For low Péclet number, the perturbation expansions proposed for the departure of the steady suspension microstructure from equilibrium $f = g_0 - 1$ and for the deflection field $\mathbf{d}$ are as follows:

$$f\left(\mathbf{s};\ \mathrm{Pe} \ll 1\right) = \mathrm{Pe}\ \mathbf{u}\cdot\mathbf{n}\ f_1\left(s\right) + \mathrm{Pe}^2\ \mathbf{uu} : \left[\mathbf{nn}\ f_2\left(s\right) + \mathbf{I}\ f_3\left(s\right)\right] + O\left(\mathrm{Pe}^3\right), \tag{A.1}$$

$$\mathbf{d}\left(\mathbf{s};\ \mathrm{Pe} \ll 1\right) = \mathbf{n}\ d_1\left(s\right) + \mathrm{Pe}\ \mathbf{u}\cdot\left[\mathbf{nn}\ d_2\left(s\right) + \mathbf{I}\ d_3\left(s\right)\right] + O\left(\mathrm{Pe}^2\right). \tag{A.2}$$

These perturbation expansions are substituted into the steady Smoluchowski equation terms,

$$\mathrm{Pe}\ \nabla_{\mathbf{s}}\cdot\left(\hat{\mathbf{M}}_r\cdot\mathbf{u}\ f\right) + \nabla_{\mathbf{s}}\cdot\hat{\mathbf{D}}_r\cdot\nabla_{\mathbf{s}}f = -\mathrm{Pe}\ \nabla_{\mathbf{s}}\cdot\left(\hat{\mathbf{M}}_r\cdot\mathbf{u}\right), \tag{A.3}$$

$$\mathrm{Pe}\ \nabla_{\mathbf{s}}\cdot\left(\hat{\mathbf{M}}_r\cdot\mathbf{u}\ \mathbf{d}\right) + \nabla_{\mathbf{s}}\cdot\hat{\mathbf{D}}_r\cdot\nabla_{\mathbf{s}}\mathbf{d} = \cdots$$

$$\frac{\lambda}{1+\lambda}\left[\nabla_{\mathbf{s}}\cdot\left(\hat{\mathbf{M}}_r\ g_0\right) + \hat{\mathbf{M}}_r\cdot\nabla_{\mathbf{s}}g_0\right] + \mathrm{Pe}\left(\hat{\mathbf{M}}_{11} - \mathbf{I}\right)\cdot\mathbf{u}\ g_0. \tag{A.4}$$

The radial boundary conditions at the excluded annulus separation are statements of no relative flux. Again, the perturbation expansions are substituted into the expressions for no relative flux,

$$\mathrm{Pe}\ \mathbf{n}\cdot\hat{\mathbf{M}}_r\cdot\mathbf{u}\ f + \mathbf{n}\cdot\hat{\mathbf{D}}_r\cdot\nabla_{\mathbf{s}}f = -\mathrm{Pe}\ \mathbf{n}\cdot\hat{\mathbf{M}}_r\cdot\mathbf{u} \quad \text{at } s = 2, \tag{A.5}$$

$$\mathrm{Pe}\ \mathbf{n}\cdot\hat{\mathbf{M}}_r\cdot\mathbf{u}\ \mathbf{d} + \mathbf{n}\cdot\hat{\mathbf{D}}_r\cdot\nabla_s\mathbf{d} = \frac{\lambda}{1+\lambda}g_0\ \mathbf{n}\cdot\hat{\mathbf{M}}_r \quad \text{at } s = 2. \tag{A.6}$$

The relative mobility associated with an applied external force acting on the probe is

$$\hat{\mathbf{M}}_r = L\left(\gamma s, \lambda\right)\mathbf{nn} + M\left(\gamma s, \lambda\right)\left(\mathbf{I} - \mathbf{nn}\right), \tag{A.7}$$

where $\gamma \equiv 1+\Delta$ is the ratio of the minimum approach distance $r_{\min}$ to the sum of the hydrodynamic radii $a+b$. The relative diffusivity describing the Brownian motion of a pair of spheres is

$$\hat{\mathbf{D}}_r = G(\gamma s, \lambda)\,\mathbf{nn} + H(\gamma s, \lambda)\,(\mathbf{I} - \mathbf{nn}). \tag{A.8}$$

The divergence of the relative mobility tensor appears on the right-hand side of both the microstructure and deflection field PDEs, and is equal to

$$\nabla_{\mathbf{s}} \cdot \hat{\mathbf{M}}_r = \left[\frac{2}{s}(L-M) + \frac{dL}{ds}\right]\,\mathbf{n} = W\,\mathbf{n}. \tag{A.9}$$

The perturbation expansion for the departure of the steady microstructure from equilibrium is regular through $O\left(\mathrm{Pe}^2\right)$ and the perturbation expansion for the deflection field is regular through $O(\mathrm{Pe})$. Thus, for as far as the perturbation expansions have been written in Equations A.1 and A.2, each of the radial functions $f_\alpha(s)$ and $d_\alpha(s)$ will decay to zero as $s \to \infty$ to satisfy the condition of no long-ranged order in the suspension microstructure. Like terms are grouped together to assemble a system of coupled ODEs. For the ODE governing the microstructure function f_1 we find

$$\frac{1}{s^2}\frac{d}{ds}\left[s^2 G\, f_1'(s)\right] - \frac{2H}{s^2} f_1(s) = -W, \tag{A.10}$$

$$f_1'(s=2) = -\frac{L}{G}, \tag{A.11}$$

$$f_1(s\to\infty) \to 0. \tag{A.12}$$

For f_2, we find

$$\frac{1}{s^2}\frac{d}{ds}\left[s^2 G\, f_2'(s)\right] - \frac{6H}{s^2} f_2(s) = -W\, f_1(s) - L\, f_1'(s) + \frac{M}{s} f_1(s), \tag{A.13}$$

$$f_2'(s=2) = -\frac{L}{G} f_1, \tag{A.14}$$

$$f_2(s\to\infty) \to 0. \tag{A.15}$$

For f_3, we find

$$\frac{1}{s^2}\frac{d}{ds}\left[s^2 G\, f_3'(s)\right] = -\frac{2H}{s^2} f_2(s) - \frac{M}{s} f_1(s), \tag{A.16}$$

$$f_3'(s=2) = 0, \tag{A.17}$$

$$f_3(s\to\infty) \to 0. \tag{A.18}$$

To reduce the region of integration from the semi-infinite domain $[2,\infty)$, the functions f_α are estimated to be power series in s^{-1} at large separations and the far-field approximations for the

hydrodynamic functions are used. For example, for f_1, the far-field form is:

$$f_1\left(s \gg 2\right) \approx f_1^{\infty}\left(\gamma s\right)^{-2} + \left(3f_1^{\infty} - \frac{10\lambda^2}{\left(1+\lambda\right)^2}\right)\left[\frac{3\lambda}{2\left(1+\lambda\right)^2}\left(\gamma s\right)^{-3} + \frac{36\lambda^2}{5\left(1+\lambda\right)^4}\left(\gamma s\right)^{-4}\right] + \cdots \quad \text{(A.19)}$$

This expression was evaluated for a large value of the radial separation $s_{\max} = 20$ for some guess of the constant f_1^{∞} and integrated backwards from $s = s_{\max}$ to $s = 2$ using the initial value problem solver `ode45` in `MATLAB`. At $s = 2$, this solution is checked to see how accurately the no-flux boundary condition, Equation A.11, is satisfied. The constant f_1^{∞} is adjusted iteratively until the no-flux boundary condition is satisfied to within an absolute tolerance of 10^{-8}. Similar expressions to equation A.19 were found for $f_2\left(s \gg 2\right)$ and $f_3\left(s \gg 2\right)$, each with an adjustable constant like f_1^{∞} used to satisfy the no-flux boundary condition upon integrating backward from $s = s_{\max}$ to $s = 2$.

The governing ODE for the leading-order perturbation to the deflection field is

$$\frac{1}{s^2}\frac{d}{ds}\left[s^2 G\; d_1'\left(s\right)\right] - \frac{2H}{s^2}d_1\left(s\right) = \frac{\lambda}{\lambda+1}\; W, \quad \text{(A.20)}$$

$$d_1'\left(s=2\right) = \frac{\lambda}{\lambda+1}\;\frac{L}{G}, \quad \text{(A.21)}$$

$$d_1\left(s\to\infty\right) \to 0. \quad \text{(A.22)}$$

By substituting $d_1\left(s\right) = -\lambda f_1\left(s\right)/\left(\lambda+1\right)$ into the system of equations for d_1, the ODE and boundary conditions for f_1 are recovered, indicating that the leading order perturbation for the deflection field is simply a scalar multiple of the leading order perturbation for the departure from equilibrium. For $d_2\left(s\right)$, we find

$$\frac{1}{s^2}\frac{d}{ds}\left[s^2 G\; d_2'\left(s\right)\right] - \frac{6H}{s^2}d_2\left(s\right) = \frac{3\lambda}{\lambda+1}\;\left(\frac{2}{3}W\; f_1\left(s\right) + L\; f_1'\left(s\right) - \frac{M}{s}f_1\left(s\right)\right) + \cdots \left(x_{11}^A - y_{11}^A\right), \quad \text{(A.23)}$$

$$d_2'\left(s=2\right) = \frac{2\lambda}{\lambda+1}\;\frac{L}{G}\; f_1\left(s\right) \quad \text{(A.24)}$$

$$d_2\left(s\to\infty\right) \to 0 \quad \text{(A.25)}$$

For $d_3\left(s\right)$, we find

$$\frac{1}{s^2}\frac{d}{ds}\left[s^2 G\; d_3'\left(s\right)\right] = -\frac{2H}{s^2}d_2\left(s\right) + \frac{3\lambda}{1+\lambda}\;\frac{M}{s}f_1\left(s\right) + \left(y_{11}^A - 1\right), \quad \text{(A.26)}$$

$$d_3'\left(s=2\right) = 0, \quad \text{(A.27)}$$

$$d_3\left(s\to\infty\right) \to 0. \quad \text{(A.28)}$$

The perturbations d_2 and d_3 to the deflection field can be calculated numerically using `ode45` in the same manner described above for the perturbations to the steady microstructure.

Appendix B

Large Péclet Boundary-Layer Analysis for Finite Size Ratios

This derivation follows from Appendix D of the work of Khair and Brady [29]. Here, we emphasize the distinction between (1) the relative mobility functions L and M arising from the applied external force, and (2) the relative diffusivity functions G and H arising from thermal motion. For identically-sized probe and bath particles, $L = G$ and $M = H$ so no distinction was necessary in the case of identical probe and bath particles. In this derivation, the excluded annulus parameter Δ is identically zero, resulting in hard-sphere interactions acting at a range coincident with the hydrodynamic radii of the probe and bath particle.

Including hydrodynamic interactions, the governing equation for the spatial evolution of the suspension microstructure is as follows:

$$\frac{1}{s^2}\frac{\partial}{\partial s}\left[s^2 G\frac{\partial g_0}{\partial s}\right] - \frac{H}{s^2}\frac{\partial}{\partial \mu}\left[\left(\mu^2-1\right)\frac{\partial g_0}{\partial \mu}\right] + \mathrm{Pe}\left[W\mu g_0 + L\mu\frac{\partial g_0}{\partial s} - \frac{M\left(\mu^2-1\right)}{s}\frac{\partial g_0}{\partial \mu}\right] = 0. \quad \text{(B.1)}$$

The conditions of no flux due to the excluded annulus potential and no long-ranged order in the suspension are, respectively

$$G\frac{\partial g_0}{\partial s} + \mathrm{Pe}\ L\ \mu\ g_0 = 0 \quad \text{at } s = 2, \quad \text{(B.2)}$$

and

$$g_0 \to 1 \quad \text{as } s \to \infty. \quad \text{(B.3)}$$

As was the case for the outer solution in the absence of hydrodynamic interactions, the microstructure will be spherically symmetric aside from the thin boundary layer on the surface of the probe particle. Batchelor [5] showed that the radial dependence of the microstructure outside the boundary layer is as follows:

$$g_0\left(s\right) = \frac{1}{L}\exp\left[\int_s^\infty \frac{2}{z}\left(1-\frac{M}{L}\right)\ \mathrm{d}z\right]. \quad \text{(B.4)}$$

Equation B.4 is $O\left(1\right)$ until lubrication effects are significant. In the limit where the radial separation

between the probe and bath particle approaches hydrodynamic contact, the hydrodynamic relative mobility functions L and M and the relative diffusivity functions G and H take on the following functional forms, which are expansions in the dimensionless surface-separation distance $\xi \equiv s - 2$:

$$L(\xi, \lambda) = L_1(\lambda)\,\xi + O\left(\xi^2 \log \xi\right), \tag{B.5}$$

$$M(\xi, \lambda) = M_0(\lambda) + M_1(\lambda)\left(\log\left(\xi^{-1}\right) - z_2(\lambda)\right)^{-1} + M_2(\lambda)\left(\log\left(\xi^{-1}\right) - z_2(\lambda)\right)^{-1} + O(\xi \log \xi), \tag{B.6}$$

$$G(\xi, \lambda) = G_1(\lambda)\,\xi + O\left(\xi^2 \log \xi\right), \tag{B.7}$$

$$H(\xi, \lambda) = H_0(\lambda) + H_1(\lambda)\left(\log\left(\xi^{-1}\right) - z_2(\lambda)\right)^{-1} + H_2(\lambda)\left(\log\left(\xi^{-1}\right) - z_2(\lambda)\right)^{-1} + O(\xi \log \xi). \tag{B.8}$$

Here, we use the forms of the hydrodynamic functions M and H suggested by Almog and Brenner [1] making the solution accurate to $O(\xi)$. Substituting the expressions B.5 and B.6 into Equation B.4, we can see that the leading-order behavior of the steady microstructure near contact is

$$g_0(\xi \to 0) \sim A_0(\lambda)\,\xi^{(M_0 - L_1)/L_1}\left(\log \xi^{-1} - z_1\right)^{-M_1/L_1}\left(\log \xi^{-1} - z_2\right)^{-M_2/L_1}, \tag{B.9}$$

which diverges as $\xi \to 0$ and which does not satisfy the no-flux boundary condition at hydrodynamic contact. Near the surface, advection and diffusion balance in a boundary layer of thickness $\delta \sim O\left(\mathrm{Pe}^{-1}\right)$ as in the identical problem with hydrodynamic interactions neglected. The inner solution must match to the outer solution given by Equation B.9 and it must satisfy the no-flux boundary condition of probability density through hydrodynamic contact. The radial coordinate near the surface is rescaled by the boundary layer thickness, *i.e.* $y = \xi/\delta = \mathrm{Pe}\ \xi$ and is substituted back into Equation B.1 to obtain the microstructure boundary-layer equation

$$\mathrm{Pe}\ \left(\frac{\partial}{\partial y}\left[G_1 y \frac{\partial g_0}{\partial y}\right] + W_0 \mu g_0 + L_1\ \mu\ y \frac{\partial g_0}{\partial y} - \frac{M_0}{2}\left(\mu^2 - 1\right)\frac{\partial g_0}{\partial \mu}\right) + \cdots = 0. \tag{B.10}$$

Only the leading order terms, those multiplied by Pe, are kept in the boundary-layer equation. The first term represents radial diffusion of pair-probability density with a linearly-growing diffusivity $G_1 y$. The second term is a source dipole of probability density weighted by the contact value of the divergence of the relative mobility $W_0 \equiv L_1 - M_0$. The third and fourth terms are the relative advection of probability density normal to and along the surface of the probe particle, respectively. The boundary conditions on the pair-distribution function are to leading order in Pe

$$G_1 y \frac{\partial g_0}{\partial y} + L_1\ y\ \mu\ g_0 = 0 \quad \text{at } y = 0, \tag{B.11}$$

$$g_0(y, \mu) \sim A_0\ \mathrm{Pe}^{W_0/L_1} y^{-W_0/L_1} \quad \text{as } y \to \infty. \tag{B.12}$$

Matching the inner problem with the outer solution to the microstructure, given in Equation B.9, we are unable to resolve the two weak multiplicative corrections in the leading-order boundary layer solution of order $(\log(\mathrm{Pe}/y) - z_\alpha)^{-M_\alpha/L_1}$. A similarity variable $\eta \equiv y/Y(\mu)$ describes the stretching of the boundary layer radial coordinate y as a function of the angle μ from the applied external force. The microstructure is proposed to have a similarity solution in this stretched boundary layer coordinate η weighted by an angular function, *i.e.* $g_0 = h(\mu)\, p(\eta)$. The governing ODE and boundary conditions for the similarity solution are

$$\eta\, p''(\eta) + [1 - \alpha\eta]\, p'(\eta) - \beta p(\eta) = 0, \tag{B.13}$$

$$\eta p'(\eta) = 0 \quad \text{at } \eta = 0 \tag{B.14}$$

$$p(\eta) \sim A_0 \frac{Y^{-W_0/L_1}(\mu)}{h(\mu)}\, \mathrm{Pe}^{W_0/L_1} \eta^{-W_0/L_1} \quad \text{as } \eta \to \infty. \tag{B.15}$$

In order for the far-field boundary condition on $p(\eta)$ to be strictly a function of the similarity variable η, it is required that the function $h(\mu) = Y^{-W_0/L_1}$. The constants α and β in Equation B.13 contain the μ-dependent function $Y(\mu)$ as well as the leading-order coefficients to the hydrodynamic functions as follows:

$$\alpha \equiv -\frac{L_1}{G_1}\, \mu Y(\mu) - \frac{M_0}{2G_1}\left(\mu^2 - 1\right) Y'(\mu), \tag{B.16}$$

$$\beta \equiv \frac{W_0}{L_1}\left[-\frac{L_1}{G_1}\mu Y(\mu) - \frac{M_0}{2G_1}\left(\mu^2 - 1\right) Y'(\mu)\right] = \frac{W_0}{L_1}\alpha \tag{B.17}$$

The ratio of the two constants is thus $\beta/\alpha = W_0/L_1$. With $\tilde{\eta} = \alpha\eta$, the governing equation may be expressed as

$$\tilde{\eta}\, p''(\tilde{\eta}) + [1 - \tilde{\eta}]\, p'(\tilde{\eta}) - \frac{W_0}{L_1} p(\tilde{\eta}) = 0, \tag{B.18}$$

which is Kummer's Equation (Abramowitz & Stegun 13.1.1)

$$z\frac{d^2w}{dz^2} + (b - z)\frac{dw}{dz} - aw = 0, \tag{B.19}$$

with $a = W_0/L_1$ and $b = 1$. Solutions to Kummer's Equation are confluent hypergeometric functions of the first and second kind, Kummer's function M and the Tricomi function U respectively

$$p\left(\frac{W_0}{L_1},\ 1,\ \alpha\eta\right) = c_1 M\left(\frac{W_0}{L_1},\ 1,\ \alpha\eta\right) + c_2 U\left(\frac{W_0}{L_1},\ 1,\ \alpha\eta\right). \tag{B.20}$$

The Tricomi function U has a logarithmic singularity as $\eta \to 0$ which would not satisfy the no-flux boundary condition at hydrodynamic contact and is so neglected ($c_2 = 0$). The limit of Kummer's

Function for large argument, provided that $\alpha < 0$, is

$$\lim_{|\alpha\eta|\to\infty} M\left(\frac{W_0}{L_1},\ 1,\ \alpha\eta\right) = \frac{1}{\Gamma\left(M_0/L_1\right)}\left(-\alpha\eta\right)^{-W_0/L_1}\left[1+O\left(\left|\alpha\eta\right|^{-1}\right)\right]. \tag{B.21}$$

If α were greater than zero, Kummer's function for large argument would behave to leading order as $\sim \exp\left(\eta\right)\eta^{-M_0/L_1}$, which is not the correct asymptotic behavior to match with Equation B.15. We may solve for the coefficient c_1 in terms of the limiting behavior from Equation B.15,

$$c_1 = A_0\ \Gamma\left(\frac{M_0}{L_1}\right)\ \left(-\alpha\mathrm{Pe}\right)^{W_0/L_1}.$$

Thus, the expression for the microstructure within the boundary layer is

$$g_0\left(y,\mu\right) = A_0\ \Gamma\left(\frac{M_0}{L_1}\right)\ \left(\frac{\mathrm{Pe}}{Y\left(\mu\right)}\right)^{W_0/L_1}\ M\left(\frac{W_0}{L_1},\ 1,\ -\frac{y}{Y\left(\mu\right)}\right).$$

We have removed α by redefining the boundary layer thickness $Y\left(\mu\right)$. Kummer's function is equal to unity for an argument of zero, and thus we may obtain the contact value of the pair-distribution function

$$g_0\left(y=0,\mu\right) = A_0\ \Gamma\left(\frac{M_0}{L_1}\right)\ \left(\frac{\mathrm{Pe}}{Y\left(\mu\right)}\right)^{W_0/L_1}.$$

The important scaling behavior to extract from the contact value of the pair distribution function is that it scales as $g_0 \sim \mathrm{Pe}^{W_0/L_1}$. If we assume that the the boundary layer thickness $Y\left(\mu\right)$ and the rate-of-change of the boundary layer thickness $Y'\left(\mu\right)$ are finite at the leading edge of the boundary layer (at $\mu = 1$), we can show from Equation B.16 that $Y\left(1\right) = G_1/L_1$. The boundary layer thickness for $-1 < \mu \leq 1$ is simply the solution to Equation B.16

$$Y\left(\mu\right) = \frac{2G_1}{M_0}\left(1-\mu^2\right)^{-L_1/M_0}\int_{\mu}^{1}\left(1-\xi^2\right)^{W_0/M_0}\mathrm{d}\xi.$$

The boundary layer thickness diverges opposite the direction of forcing as $Y\left(\mu\to-1\right) \sim \left(1+\mu\right)^{-L_1/M_0}$. Within the radial boundary layer near $\mu = -1$ is an angular region of thickness $\epsilon \sim \mathrm{Pe}^{-1}$ in which the angular diffusion terms cannot be neglected from the leading-order governing PDE. Thus, if we define a second boundary layer coordinate $x \equiv \left(\mu+1\right)/\epsilon = \mathrm{Pe}\left(\mu+1\right)$, the governing PDE for the microstructure in this region where angular diffusion terms become important is

$$\frac{\partial}{\partial y}\left(G_1 y\frac{\partial g_0}{\partial y}\right) + \frac{\partial}{\partial x}\left(\frac{H_0}{2}x\frac{\partial g_0}{\partial x}\right) - W_0 g_0 - L_1 y\frac{\partial g_0}{\partial y} + M_0 x\frac{\partial g_0}{\partial x} = 0.$$

We see that within this coalescence region we have radial and angular diffusive terms whose diffusivities, $G_1 y$ and $H_0 x/2$ respectively, increase linearly. The advection terms push the probability density in the direction of increasing y (toward $y\to\infty$) and in the direction of decreasing x, toward

$x \to 0$. What was a source dipole in the original boundary-layer equation for y alone is now a sink of probability density for the coalescence region boundary layer equation. Further analysis in this region is unnecessary because the volume of the coalescence region $\mathrm{d}\mathbf{s} = s^2 \mathrm{d}s\ \sin\theta \mathrm{d}\theta\ \mathrm{d}\phi \sim O\left(\mathrm{Pe}^{-2}\right)$, which will not be the leading-order contribution to microviscosity integrals in the entire boundary layer region, whose volume scales as $O\left(\mathrm{Pe}^{-1}\right)$.

Appendix C

Large Péclet Boundary-Layer Analysis for Small Probes ($\lambda \gg 1$)

As $\lambda \rightarrow \infty$ the growth of the boundary layer thickness on the rear face of the probe particle becomes more and more rapid, as was shown in Figure 2.9. In the limit of infinitesimally small probe particles, the boundary layer thickness Y diverges at $\mu = 0$, indicating the similarity solution is no longer valid for both the anterior and posterior face of the probe. Physically, in the limit $\lambda \rightarrow \infty$, bath particles on the anterior face of the probe that diffuse radially outward will exit the boundary layer to reenter the advection-dominated region. The streamlines from the infinite Péclet outer solution will advect the bath particle right back inside the boundary layer; the relative velocity along the line of centers owing to advective motion is $O(1)$. Once we reach $\mu = 0$ and pass into the posterior face of the probe particle, any diffusive motion normal to the surface that takes the bath particle outside of the thin boundary layer will cause it to advect away from the probe particle as it no longer hydrodynamically "sees" the probe. In this appendix, we approach the boundary layer solution for the equilibrium microstructure for infinitesimally small probe particles and find that a boundary layer solution exists and is valid for only the anterior face of the probe particle, much like what was the case for the boundary layer solution for the steady microstructure in the absence of hydrodynamic interactions presented in Appendix D of the work by Khair and Brady [29].

We begin by recognizing that the outer solution for the advection-dominated suspension microstructure given in Equation B.9 takes on the limiting form as the radial separation between the probe and bath particle approaches the lubrication regime

$$g_0 = C\xi^{-1} \quad \text{as } \xi \rightarrow 0 \tag{C.1}$$

In order for lubrication interactions to be significant in the limit $\lambda \gg 1$, the dimensionless surface separation ξ must be the smallest length scale in the problem, even more so than the probe radius, and hence the product $\lambda\xi$ should be less than unity. The matching condition for the boundary layer

problem, in which advection balances diffusion, as the rescaled radial boundary layer coordinate $y \equiv \mathrm{Pe}\xi$ grows to infinity is thus

$$g_0 = \mathrm{Pe}\ C y^{-1} \quad \text{as } y \to \infty \tag{C.2}$$

The constant C is size-ratio dependent, and is found to approach $2/\lambda$ for small probes as shown in Figure 2.6. The governing differential equation inside the boundary layer expanded in powers of the size ratio λ is

$$\begin{aligned} &\frac{1}{2}\lambda\left[\frac{\partial}{\partial y}\left(y\left(\frac{\partial g}{\partial y}+\mu g\right)\right)\right]+\frac{1}{2}\lambda^0\left[\frac{\partial}{\partial y}\left(y\left(2\frac{\partial g}{\partial y}+3\mu g\right)\right)\right] \\ &+\frac{1}{2}\lambda^{-1}\left[\frac{\partial}{\partial y}\left(y\left(\frac{\partial g}{\partial y}+3\mu g\right)\right)-\frac{3}{4}\frac{\partial}{\partial \mu}\left[\left(\mu^2-1\right)g\right]\right]+\cdots \quad = \quad 0 \end{aligned} \tag{C.3}$$

The no-flux boundary condition, expanded in powers of the size ratio, is

$$\frac{1}{2}\lambda\left(y\left(\frac{\partial g}{\partial y}+\mu g\right)\right)+\frac{1}{2}\lambda^0\left(y\left(2\frac{\partial g}{\partial y}+3\mu g\right)\right)+\frac{1}{2}\lambda^{-1}\left(y\left(\frac{\partial g}{\partial y}+3\mu g\right)\right)+\cdots=0 \quad \text{at } y=0. \tag{C.4}$$

We expand the suspension microstructure inside the boundary layer in powers of Pe and λ,

$$g_0\left(y,\mu;\ \mathrm{Pe},\lambda\right)=\mathrm{Pe}\left[\lambda\overline{g}_0\left(y,\mu\right)+\lambda^0\overline{g}_1\left(y,\mu\right)+\lambda^{-1}\overline{g}_2\left(y,\mu\right)+\cdots\right]+O\left(\mathrm{Pe}^0\right). \tag{C.5}$$

The choice of allowing the largest term in the perturbation expansion to be $O\left(\mathrm{Pe}\lambda\right)$ is known with some foresight: we will be unable to match to the outer solution until the term $\overline{g}_2$ – both $\overline{g}_0$ and $\overline{g}_1$ are found to decay exponentially with increasing y. Because the prefactor $C = 2/\lambda$, we know that the prefactor for the function $\overline{g}_2$ should scale as $\mathrm{Pe}\lambda^{-1}$. The governing equation for $\overline{g}_0$ is obtained by substituting Equation C.5 into C.3 and keeping only the largest terms, *i.e.* those of order $O\left(\mathrm{Pe}\lambda^2\right)$,

$$\frac{\partial}{\partial y}\left(y\left(\frac{\partial \overline{g}_0}{\partial y}+\mu\overline{g}_0\right)\right)=0. \tag{C.6}$$

The general solution to Equation C.6 has the following functional form:

$$\overline{g}_0 = A_0\left(\mu\right)\exp\left(-\mu y\right). \tag{C.7}$$

This solution satisfies the no-flux boundary condition at $y = 0$ and decays to zero outside the boundary layer as $y \to \infty$ as it should with no terms of $O\left(\mathrm{Pe}\lambda\right)$ in the outer solution. To determine the coefficient $A_0\left(\mu\right)$, we must progress further in the perturbation expansion in λ. The governing

equation for $\overline{g}_1$ is obtained from terms of order $O(\mathrm{Pe}\lambda)$ from equation C.3,

$$\frac{\partial}{\partial y}\left(y\left(\frac{\partial \overline{g}_1}{\partial y}+\mu\overline{g}_1+A_0(\mu)\,\mu\exp(-\mu y)\right)\right)=0. \tag{C.8}$$

Knowing the general solution for $\overline{g}_1$ does not yet allow us to evaluate the functional form of $A_0(\mu)$, as the tangential advection terms are another order of λ smaller. The general solution for $\overline{g}_1$ also introduces another constant $A_1(\mu)$ that is yet to be determined,

$$\overline{g}_1=\left(A_1(\mu)-\mu y A_0(\mu)\right)\exp(-\mu y). \tag{C.9}$$

We see that, like $\overline{g}_0$, this solution decays to zero outside of the boundary layer to satisfy the matching criterion. In solving the governing equation for $\overline{g}_2$, we will be able to determine the coefficient A_0,

$$\frac{\partial}{\partial y}\left(y\left(\frac{\partial \overline{g}_2}{\partial y}+\mu\overline{g}_2+\left(\mu A_1-\mu^2 y A_0\right)\exp(-\mu y)\right)\right)=\frac{3}{4}\frac{\partial}{\partial\mu}\left[\left(\mu^2-1\right)A_0(\mu)\exp(-\mu y)\right]. \tag{C.10}$$

We can integrate this expression once with respect to y, introducing a third integration constant $A_2(\mu)$,

$$y\left(\frac{\partial \overline{g}_2}{\partial y}+\mu\overline{g}_2+\left(\mu A_1-\mu^2 y A_0\right)\exp(-\mu y)\right)=-\frac{3}{4}\frac{\partial}{\partial\mu}\left[\frac{\left(\mu^2-1\right)A_0}{\mu}\exp(-\mu y)\right]+A_2(\mu). \tag{C.11}$$

In order to satisfy the no-flux boundary condition, the right-hand side of Equation C.11 must equal zero at hydrodynamic contact ($y=0$). Thus, we can relate $A_0(\mu)$ to the latest introduced integration constant $A_2(\mu)$ and a constant α,

$$A_0(\mu)=\frac{\mu}{\mu^2-1}\left[\int\frac{4}{3}A_2(\mu)\,\mathrm{d}\mu+\alpha\right]. \tag{C.12}$$

To determine the coefficient $A_2(\mu)$, we must continue to solve for $\overline{g}_2$ and match to the outer solution. Solving Equation C.11 for $\overline{g}_2$, we find,

$$\overline{g}_2=\left[B_0^*(\mu)+B_1^*(\mu)\ln y+B_2^*(\mu)\,y+B_3^*(\mu)\,y^2\right]\exp(-\mu y)+A_2(\mu)\frac{\mathrm{Ei}(\mu y)}{\exp(\mu y)}, \tag{C.13}$$

where we have introduced the coefficients $B_0^*-B_3^*$ for compactness. The coefficient B_0^* is simply the last integration constant, and the remaining coefficients are combinations of μ, $A_0(\mu)$, and $A_1(\mu)$:

$$B_1^*(\mu)=-\frac{3}{4}\frac{d}{d\mu}\left[\frac{\mu^2-1}{\mu}A_0(\mu)\right], \tag{C.14}$$

$$B_2^*(\mu)=\frac{3}{4}\frac{\mu^2-1}{\mu}A_0(\mu)-\mu A_1(\mu), \tag{C.15}$$

and

$$B_3^*(\mu) = \frac{\mu^2}{2} A_0(\mu), \tag{C.16}$$

The function $\mathrm{Ei}(\mu y)$ is the exponential integral. For large argument, the ratio $\mathrm{Ei}(\mu y)/\exp(\mu y)$ approaches $(\mu y)^{-1} + O\left((\mu y)^{-2}\right)$. All other terms in $\overline{g}_2$ decay exponentially quickly with large y, rather than algebraically. Thus, the limit of $\mathrm{Pe}\lambda^{-1}\overline{g}_2(y,\mu)$ for large y is

$$\lim_{y\to\infty} \mathrm{Pe}\lambda^{-1}\overline{g}_2(y,\mu) \sim \mathrm{Pe}\lambda^{-1} A_2(\mu)(\mu y)^{-1}. \tag{C.17}$$

In order to satisfy the matching criterion in Equation C.2 and knowing that $C = 2/\lambda$, we are able to determine that the coefficient $A_2(\mu)$ must equal 2μ. We may now determine the function $A_0(\mu)$

$$A_0(\mu) = \frac{\mu}{\mu^2 - 1}\left[\frac{4}{3}\mu^2 + \alpha\right]. \tag{C.18}$$

In order to prevent the boundary-layer solution from becoming singular along the line of forcing ($\mu = 1$), the constant of integration α must be equal to $-4/3$. The leading order boundary-layer solution is thus

$$g_0(y,\mu;\ \mathrm{Pe},\lambda) = \mathrm{Pe}\lambda\left[\frac{4}{3}\mu\exp(-\mu y)\right] + O(\mathrm{Pe}). \tag{C.19}$$

The Brownian contribution to the intrinsic microviscosity η_i^B resulting from this boundary layer solution scales like $\lambda^2\mathrm{Pe}^{-1}$, with the two powers of λ arising from the magnitude of the leading order boundary-layer solution and the magnitude of the divergence of the relative mobility near hydrodynamic contact. However, in order for the hydrodynamic mobility functions perpendicular to the line of centers, *i.e.* M and H, to adopt the asymptotic form of $3/4\lambda$ for the entirety of the compression boundary layer, the Péclet number must be greater than $\lambda\mathrm{e}^{\lambda}$. Thus, the magnitude of the Brownian contribution to the intrinsic microviscosity is negligible even for small probes in the limit of strong forcing.

Recall that the hydrodynamic contribution to the intrinsic microviscosity η_i^H is

$$\eta_i^H = -\frac{3}{4\pi}\left(\frac{1+\lambda^{-1}}{2}\right)^3 \int_{s\geq 2} g_0(\mathbf{s})\ (\mathbf{M}_{11}^* - \mathbf{I}) : \mathbf{uu}\ \mathrm{d}\mathbf{s},$$

and that when the bath particle resides in the compression boundary layer, the probe particle's self mobility must be $O\left(\lambda^{-1}\right)$ as a force applied to itself must translate both the probe and the large bath particle. The hydrodynamic contribution to the intrinsic microviscosity arising from the boundary layer on the anterior face of the probe is simply $\eta_i^H = \lambda$. Note that Davis and Hill predicted [16], for a fore-aft symmetric microstructure at infinite Pe, *i.e.* no Brownian motion whatsoever, that the intrinsic microviscosity for small probes with full consideration of hydrodynamic interactions is $\eta_i = 2\lambda$, consistent with the answer derived in this appendix. Thus, we predict a small probe

forced through a dispersion at a large-but-finite Péclet number will still have an $O(\lambda)$ perceived microviscosity. Interparticle interactions are necessary to explain how interpreted microviscosities for small probes could drop to $O(1)$.

Appendix D

Microviscosity contributions for various excluded annulus parameters

In this appendix, we compile the microviscosity contributions as a function of Péclet number for fine bath-to-probe particle size ratios ranging from $\lambda = 1/8$ to $\lambda = 8$. Results for excluded annulus parameters ranging from $\Delta = 10^{-5}$ to $\Delta = 1$ are presented. Some features of note include the scaling of the interparticle contribution with the excluded-annulus parameter Δ, a decreasing extent of force-thickening from the hydrodynamic contribution once probe and bath particle configurations within the lubrication limit are disallowed by the excluded annulus potential, and nonmonotonicity in the Brownian contribution as a function of particle size ratio λ for $O(1)$ excluded annulus parameters. The same legend conventions apply to each plot, with hydrodynamic, Brownian, interparticle, and total intrinsic microviscosity contributions denoted by red, blue, green, and black, respectively. Dark symbols are results computed by the Legendre polynomial method and light symbols are calculated from the discretized microstructure of the finite difference scheme. Both methods are detailed in section 2.5. In the event where space did not permit inclusion of a legend, please refer to the microviscosity contributions at a different excluded-annulus parameter.

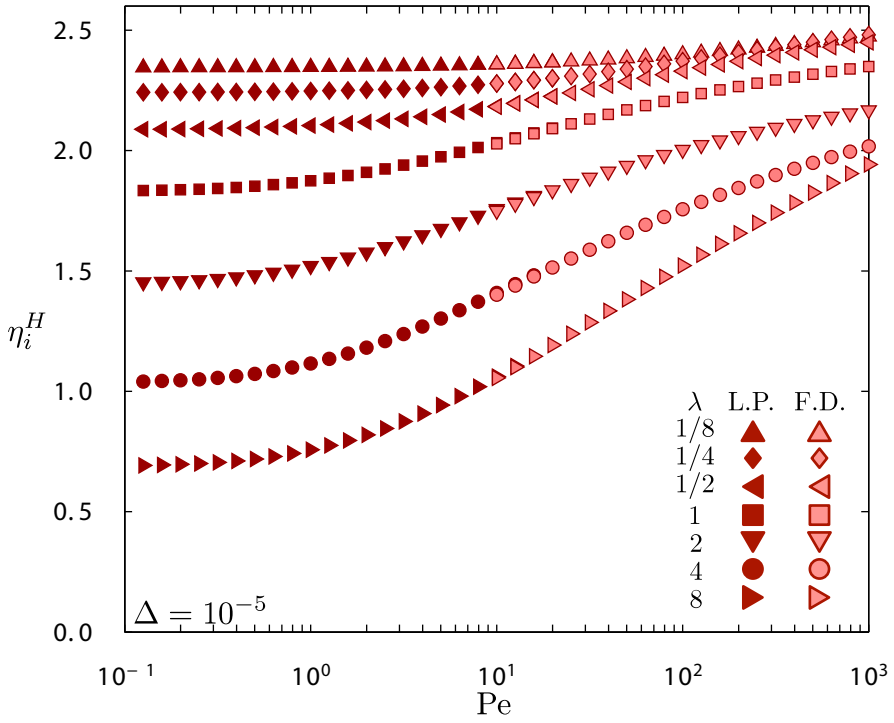

Figure D.1: Hydrodynamic contribution to the intrinsic microviscosity η_i^H as a function of Pe for an excluded annulus parameter Δ of 10^{-5}.

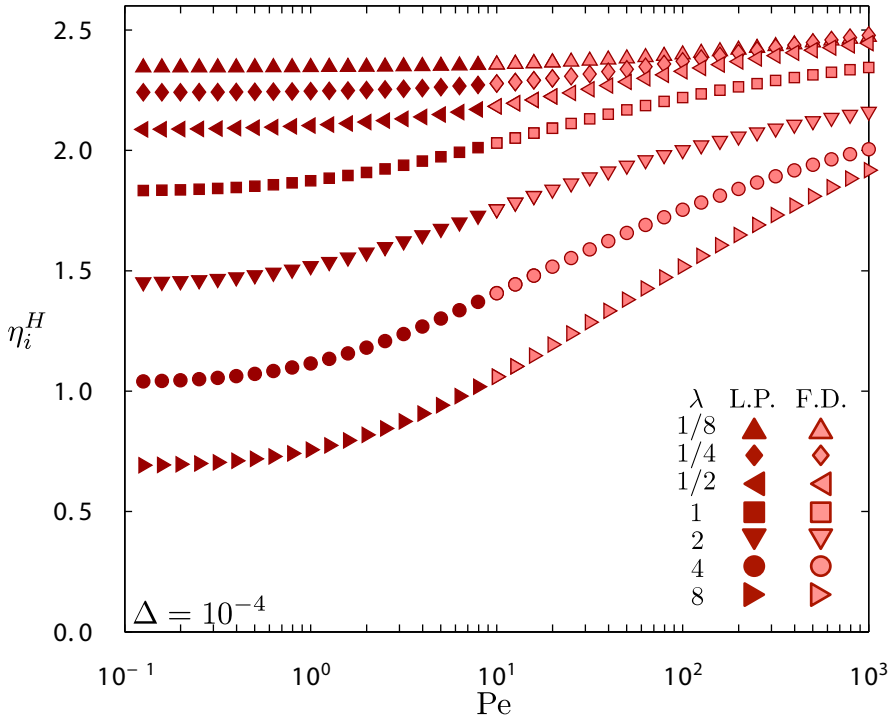

Figure D.2: Hydrodynamic contribution to the intrinsic microviscosity η_i^H as a function of Pe for an excluded annulus parameter Δ of 10^{-4}.

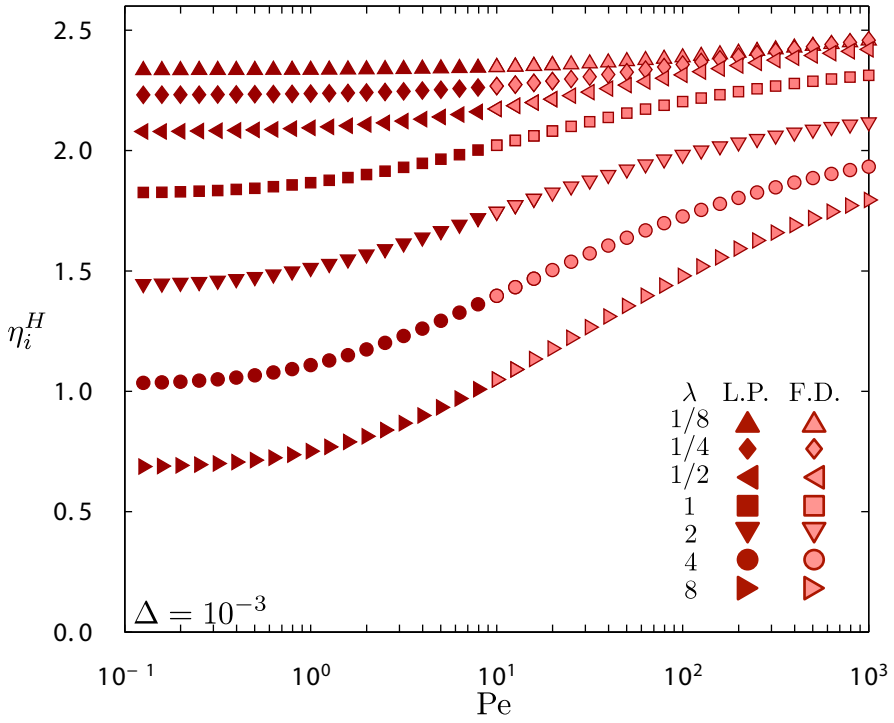

Figure D.3: Hydrodynamic contribution to the intrinsic microviscosity η_i^H as a function of Pe for an excluded annulus parameter Δ of 10^{-3}.

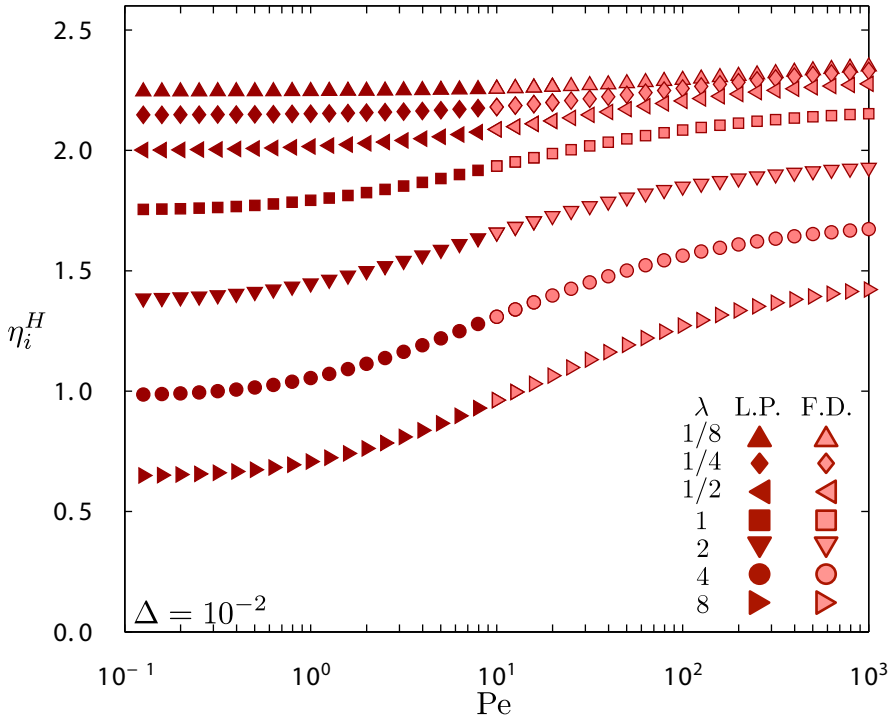

Figure D.4: Hydrodynamic contribution to the intrinsic microviscosity η_i^H as a function of Pe for an excluded annulus parameter Δ of 10^{-2}.

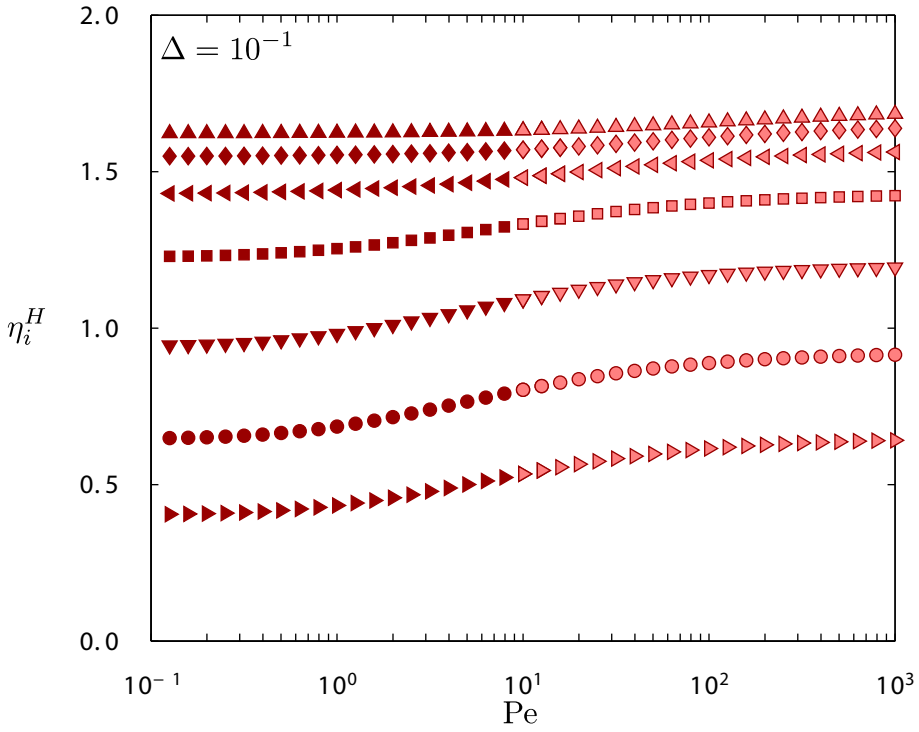

Figure D.5: Hydrodynamic contribution to the intrinsic microviscosity η_i^H as a function of Pe for an excluded annulus parameter Δ of 10^{-1}.

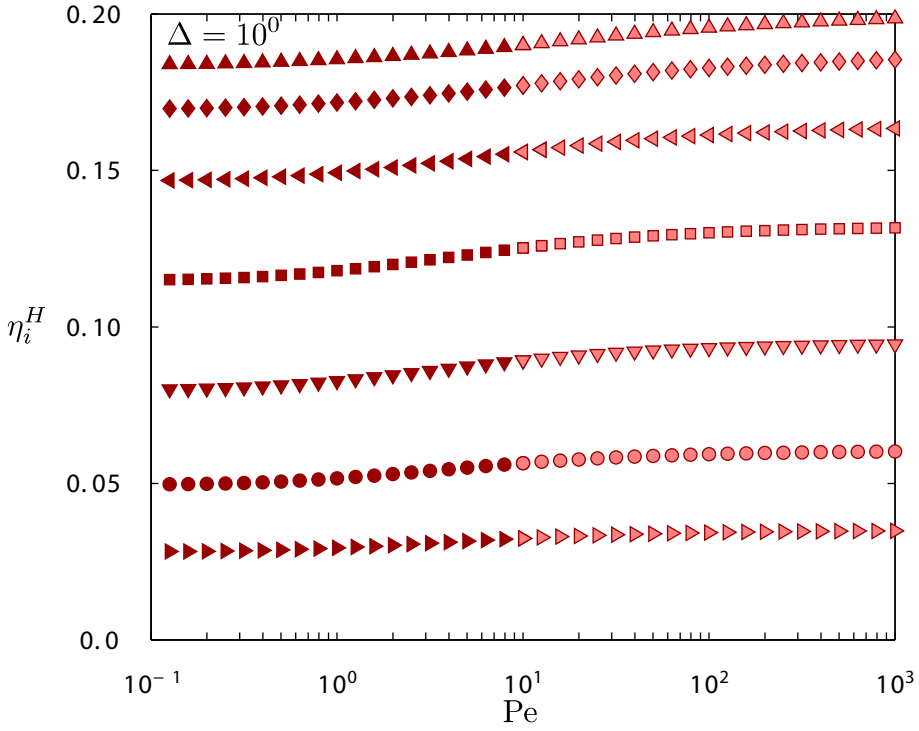

Figure D.6: Hydrodynamic contribution to the intrinsic microviscosity η_i^H as a function of Pe for an excluded annulus parameter Δ of 10^0.

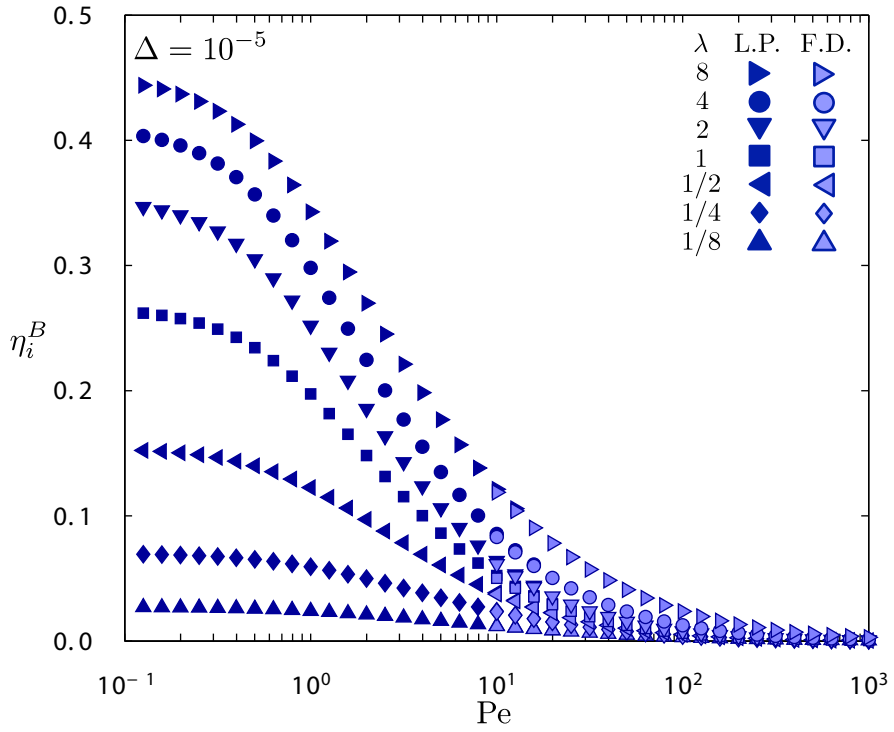

Figure D.7: Brownian contribution to the intrinsic microviscosity η_i^B as a function of Pe for an excluded annulus parameter Δ of 10^{-5}.

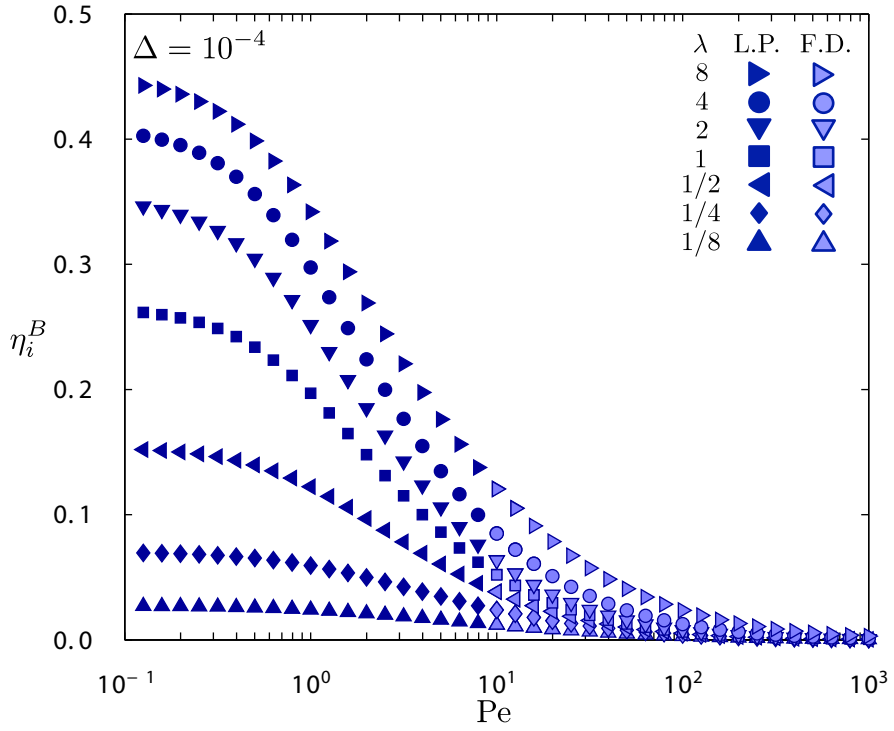

Figure D.8: Brownian contribution to the intrinsic microviscosity η_i^B as a function of Pe for an excluded annulus parameter Δ of 10^{-4}.

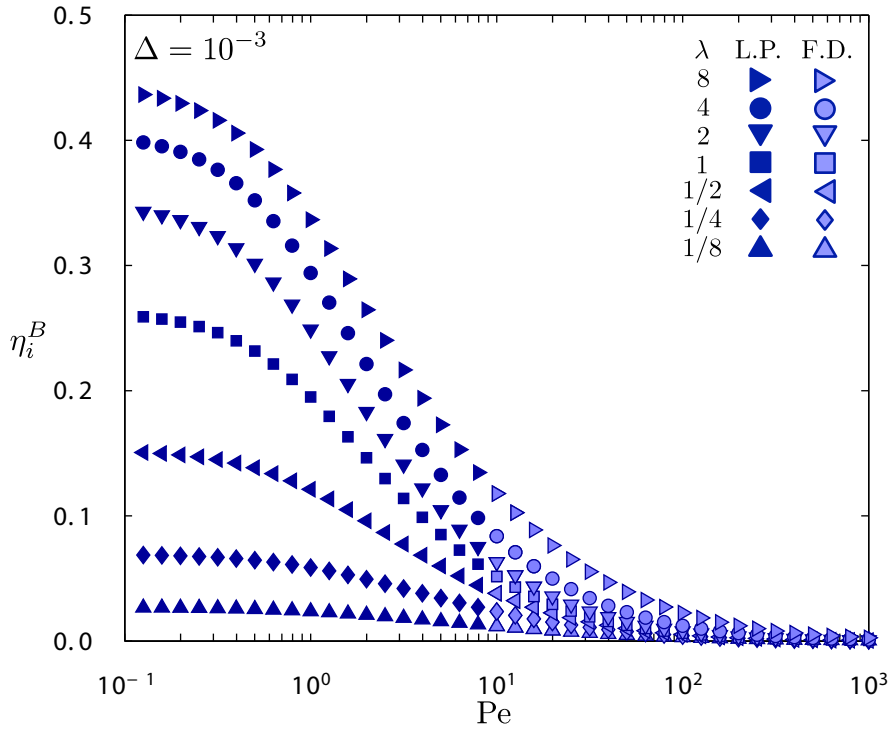

Figure D.9: Brownian contribution to the intrinsic microviscosity η_i^B as a function of Pe for an excluded annulus parameter Δ of 10^{-3}.

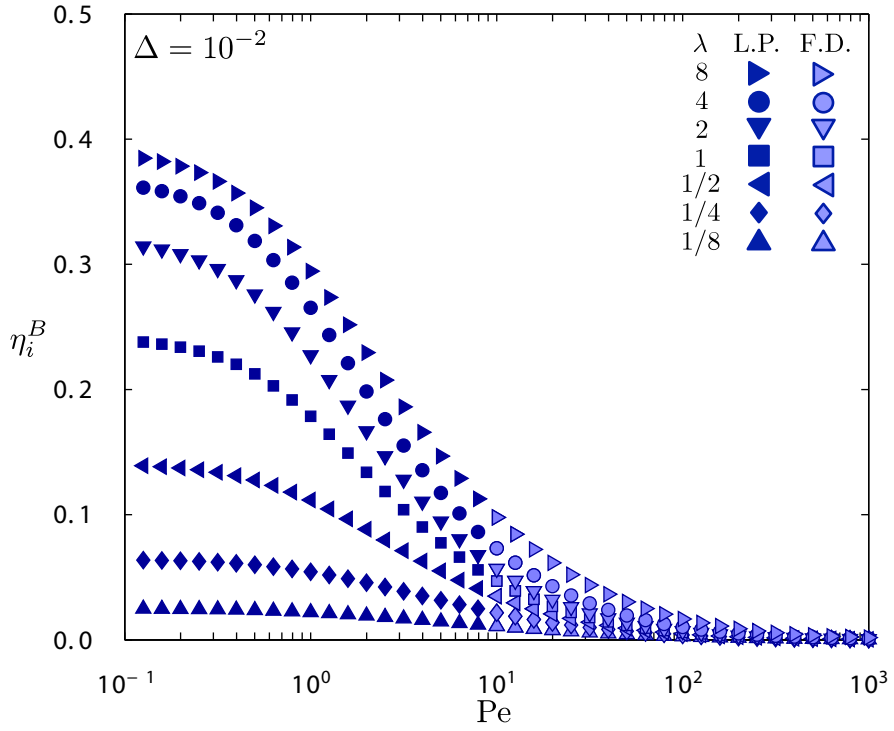

Figure D.10: Brownian contribution to the intrinsic microviscosity η_i^B as a function of Pe for an excluded annulus parameter Δ of 10^{-2}.

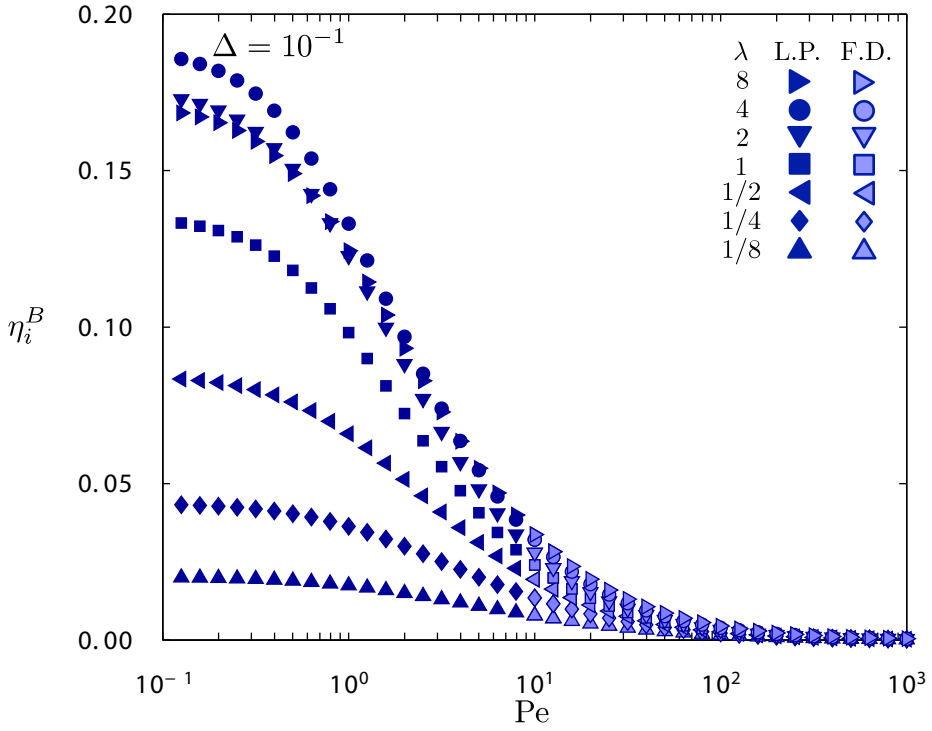

Figure D.11: Brownian contribution to the intrinsic microviscosity η_i^B as a function of Pe for an excluded annulus parameter Δ of 10^{-1}.

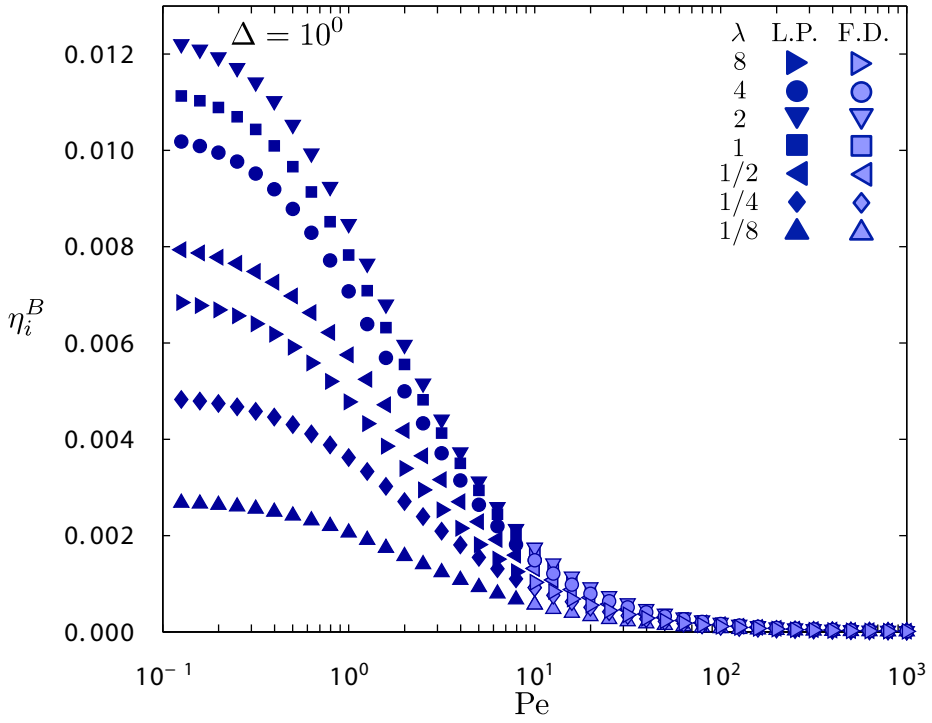

Figure D.12: Brownian contribution to the intrinsic microviscosity η_i^B as a function of Pe for an excluded annulus parameter Δ of 10^0.

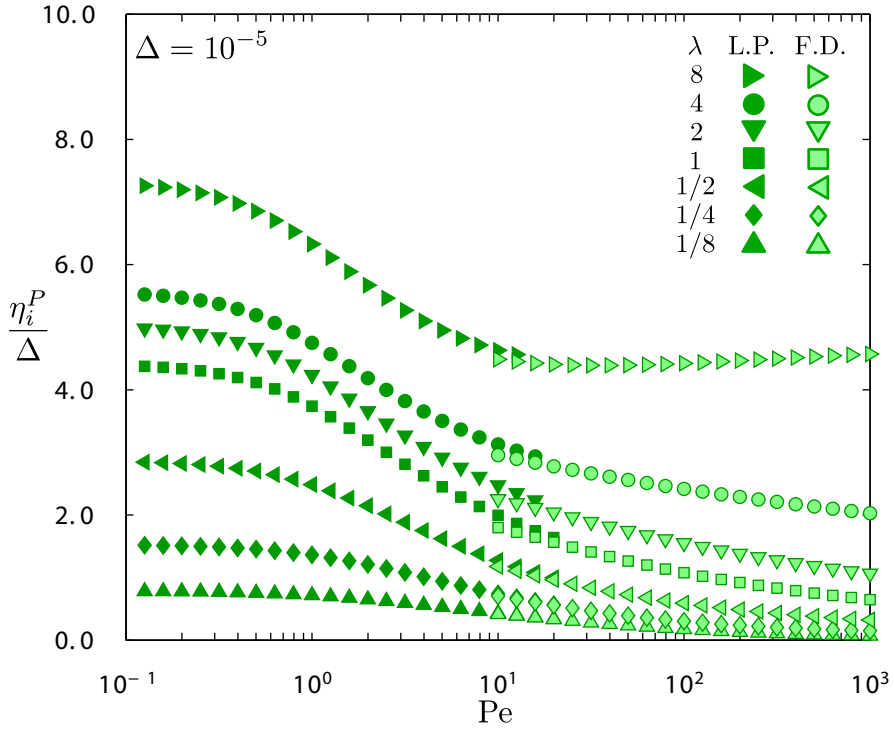

Figure D.13: Interparticle contribution to the intrinsic microviscosity normalized by the excluded-annulus parameter η_i^P/Δ as a function of Pe for Δ of 10^{-5}.

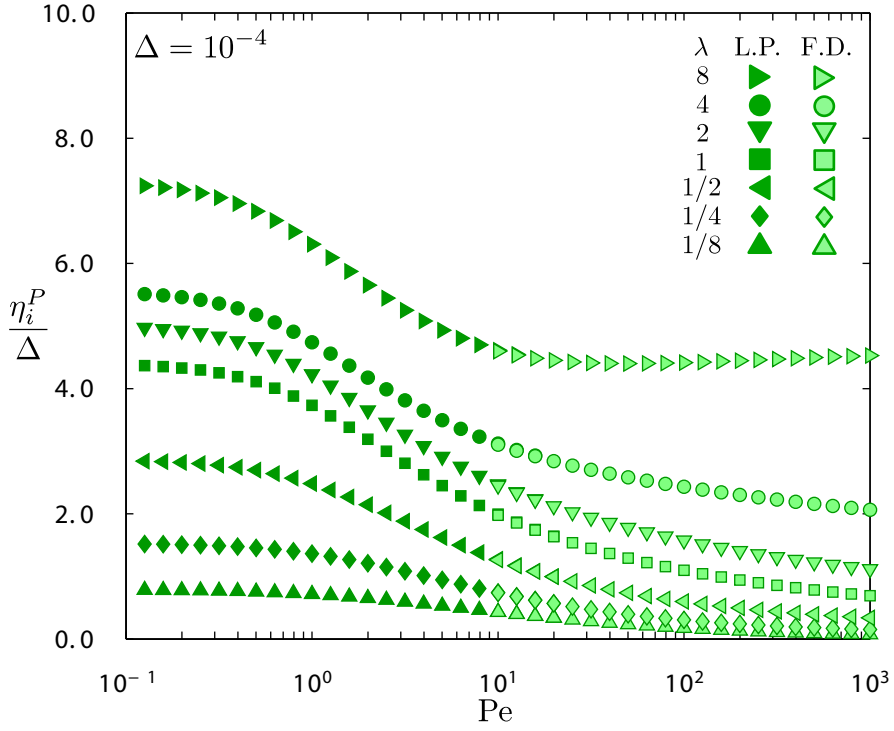

Figure D.14: Interparticle contribution to the intrinsic microviscosity normalized by the excluded-annulus parameter η_i^P/Δ as a function of Pe for Δ of 10^{-4}.

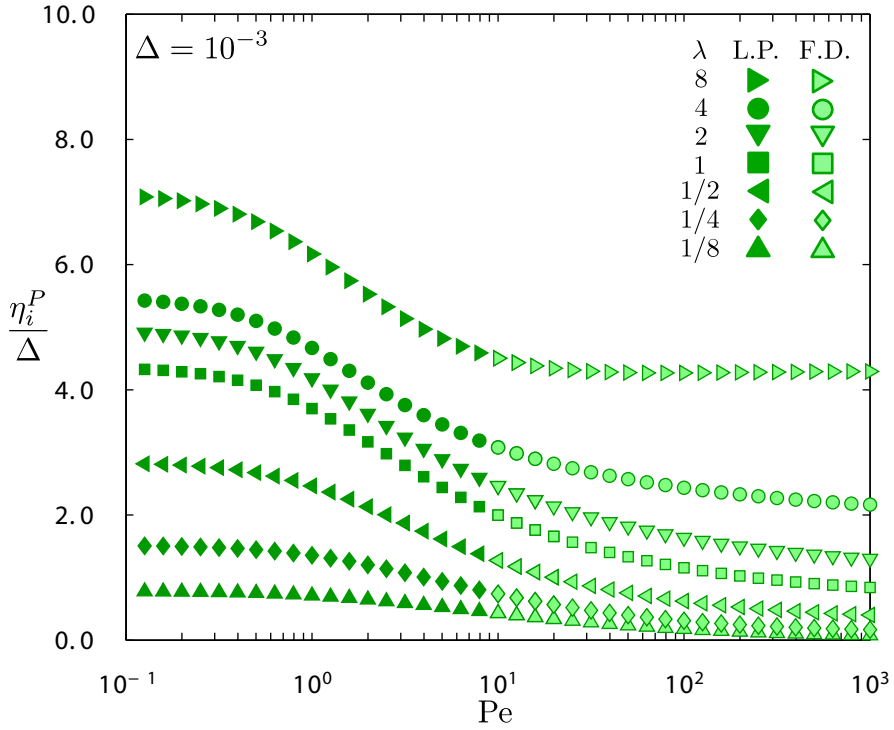

Figure D.15: Interparticle contribution to the intrinsic microviscosity normalized by the excluded-annulus parameter η_i^P/Δ as a function of Pe for Δ of 10^{-3}.

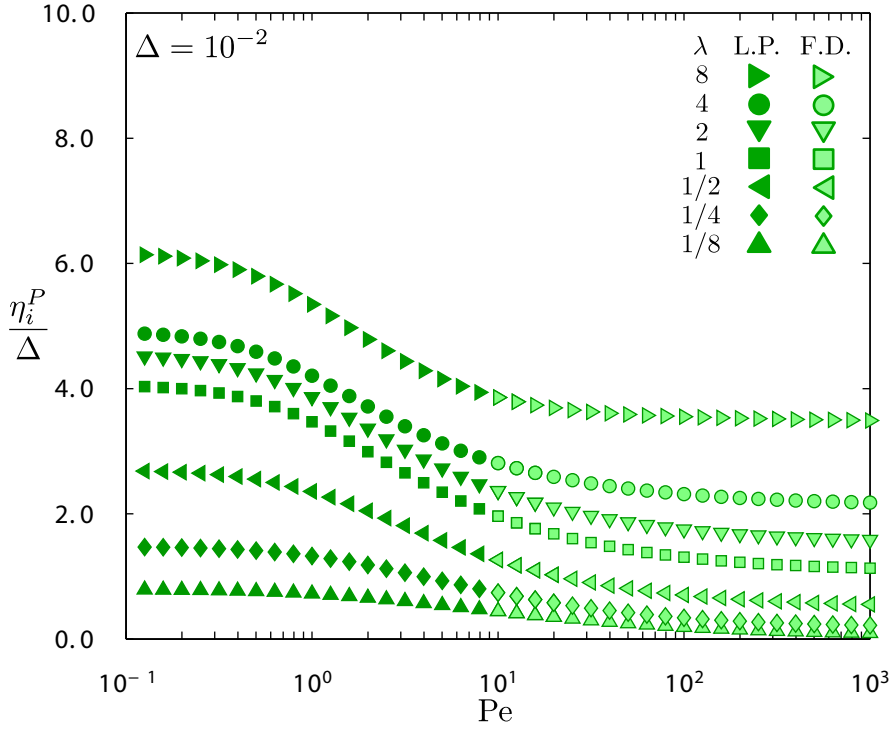

Figure D.16: Interparticle contribution to the intrinsic microviscosity normalized by the excluded-annulus parameter η_i^P/Δ as a function of Pe for Δ of 10^{-2}.

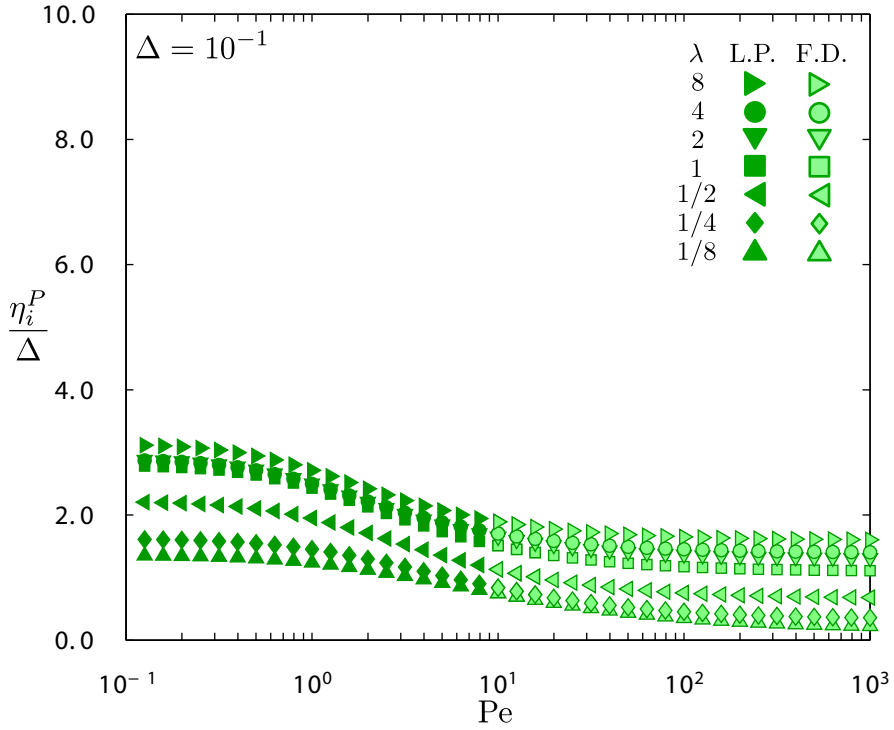

Figure D.17: Interparticle contribution to the intrinsic microviscosity normalized by the excluded-annulus parameter η_i^P/Δ as a function of Pe for Δ of 10^{-1}.

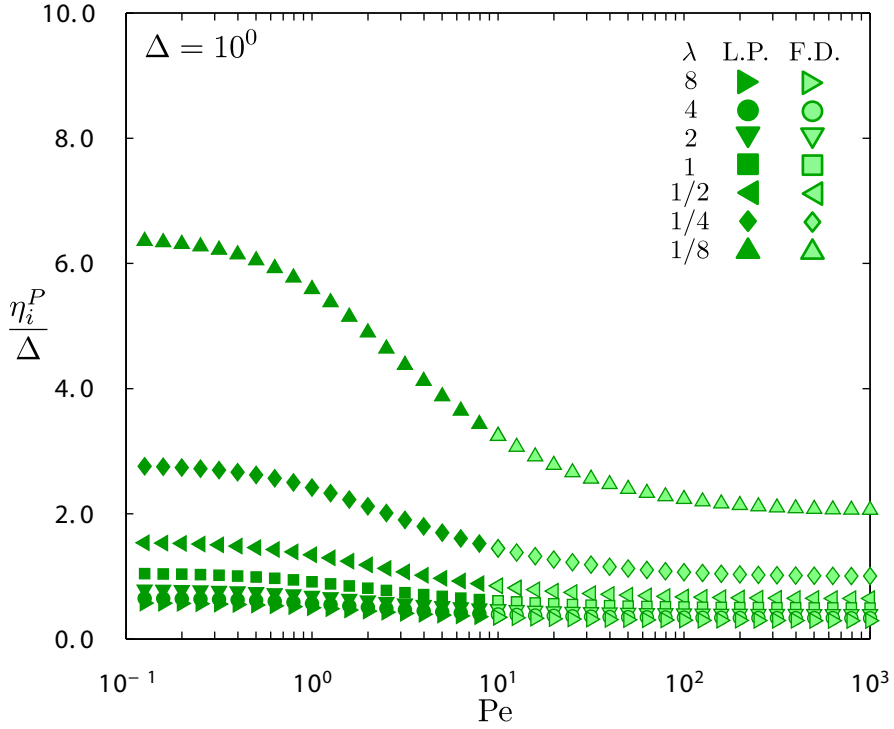

Figure D.18: Interparticle contribution to the intrinsic microviscosity normalized by the excluded-annulus parameter η_i^P/Δ as a function of Pe for Δ of 10^0.

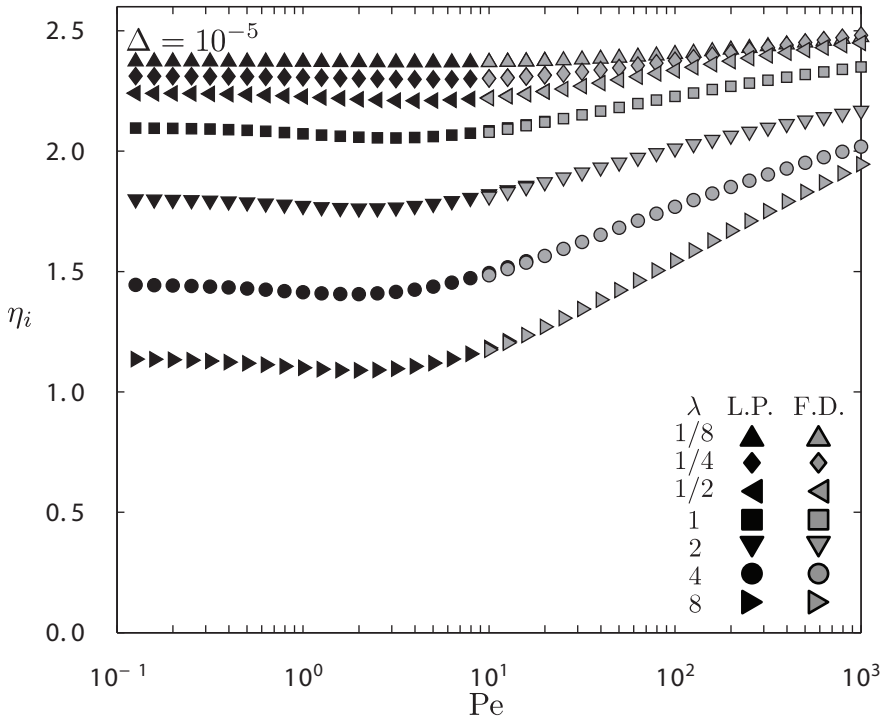

Figure D.19: Total intrinsic microviscosity as a function of Pe for an excluded annulus parameter Δ of 10^{-5}.

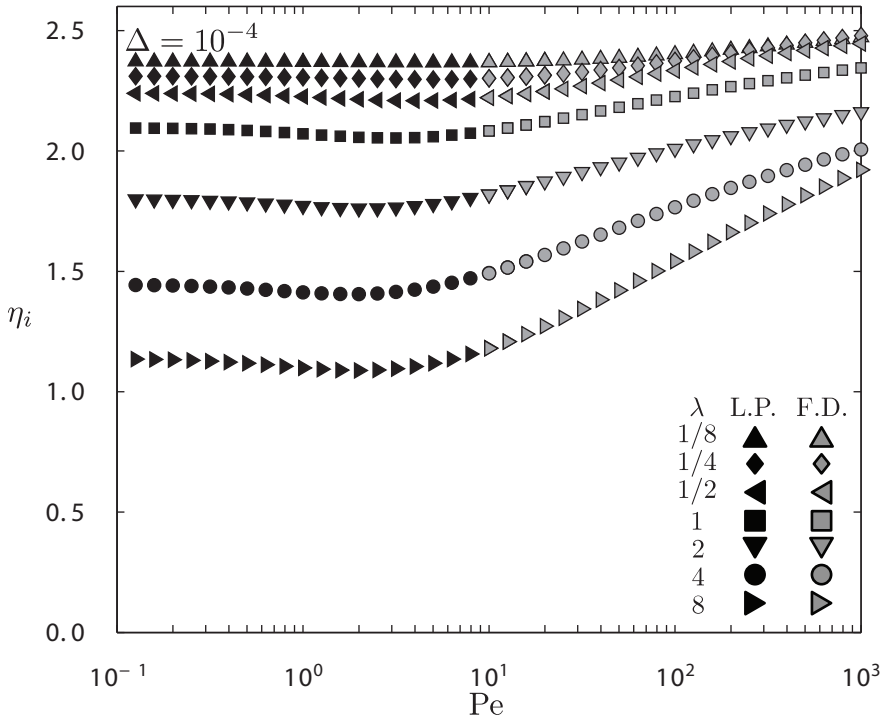

Figure D.20: Total intrinsic microviscosity as a function of Pe for an excluded annulus parameter Δ of 10^{-4}.

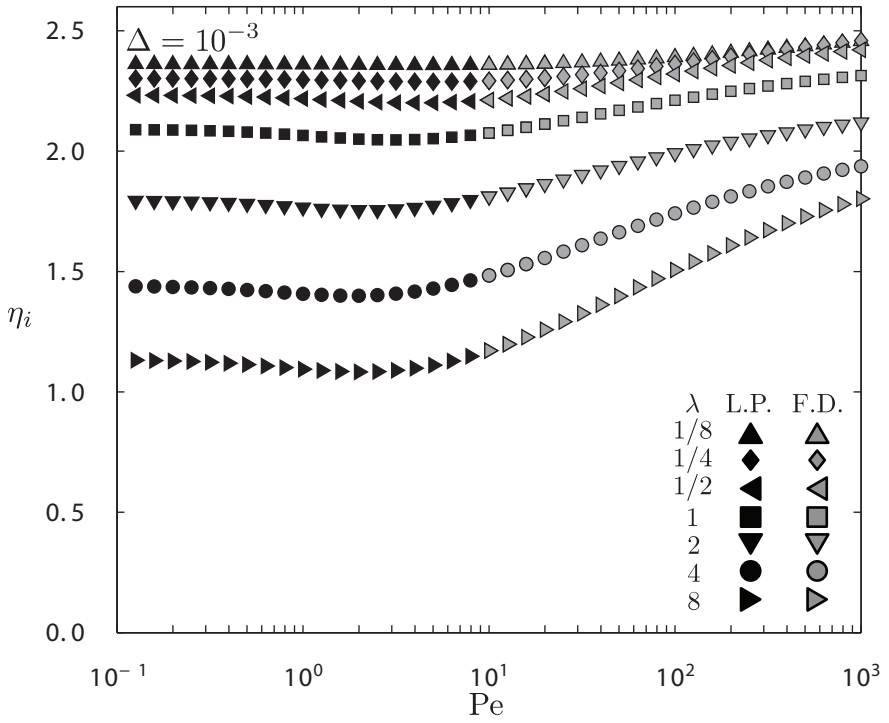

Figure D.21: Total intrinsic microviscosity as a function of Pe for an excluded annulus parameter Δ of 10^{-3}.

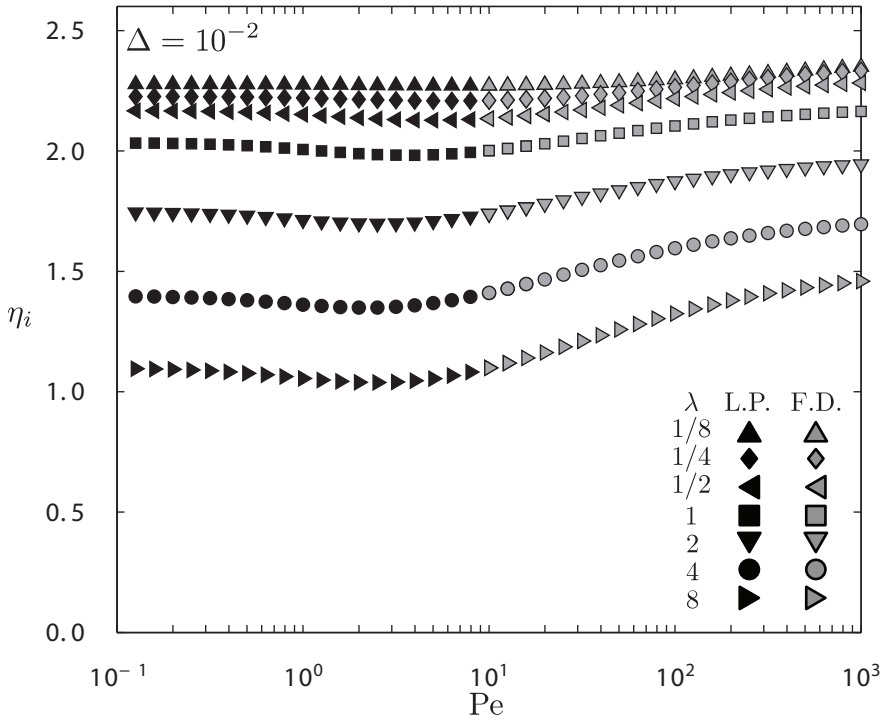

Figure D.22: Total intrinsic microviscosity as a function of Pe for an excluded annulus parameter Δ of 10^{-2}.

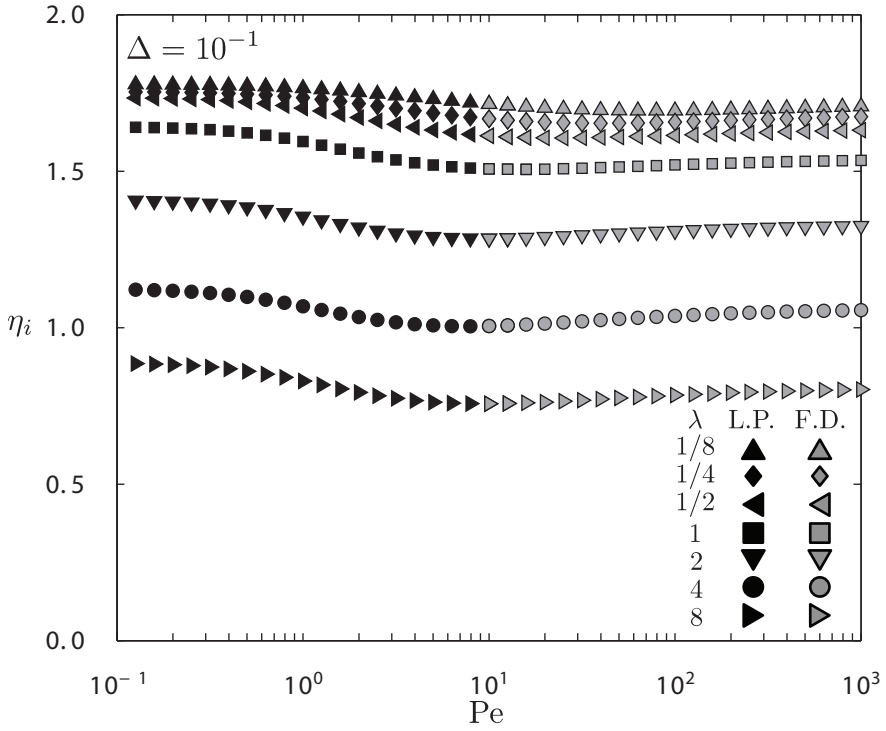

Figure D.23: Total intrinsic microviscosity as a function of Pe for an excluded annulus parameter Δ of 10^{-1}.

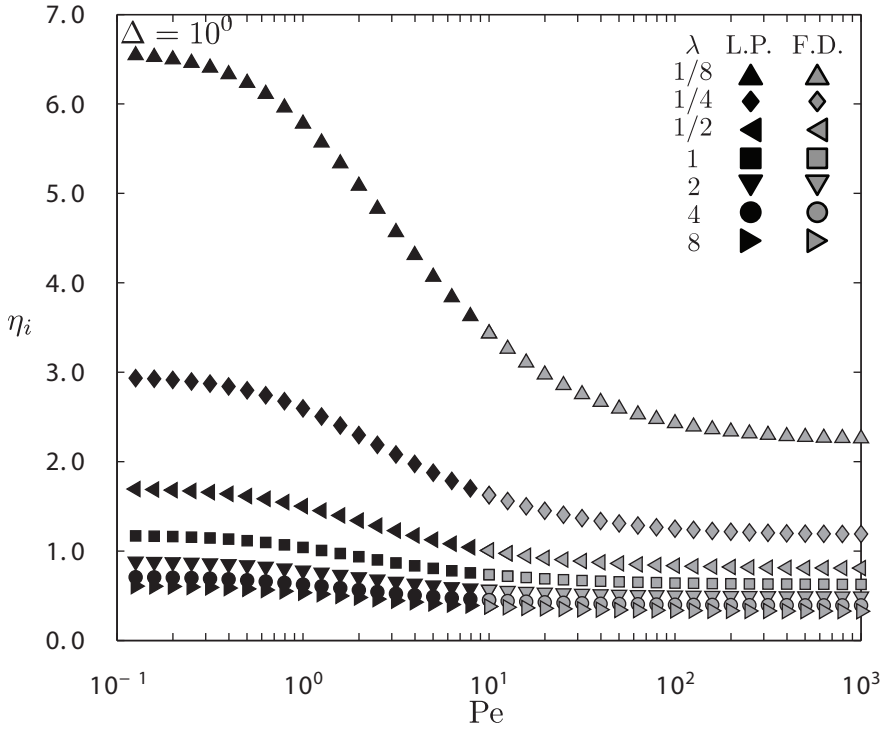

Figure D.24: Total intrinsic microviscosity as a function of Pe for an excluded annulus parameter Δ of 10^{0}.

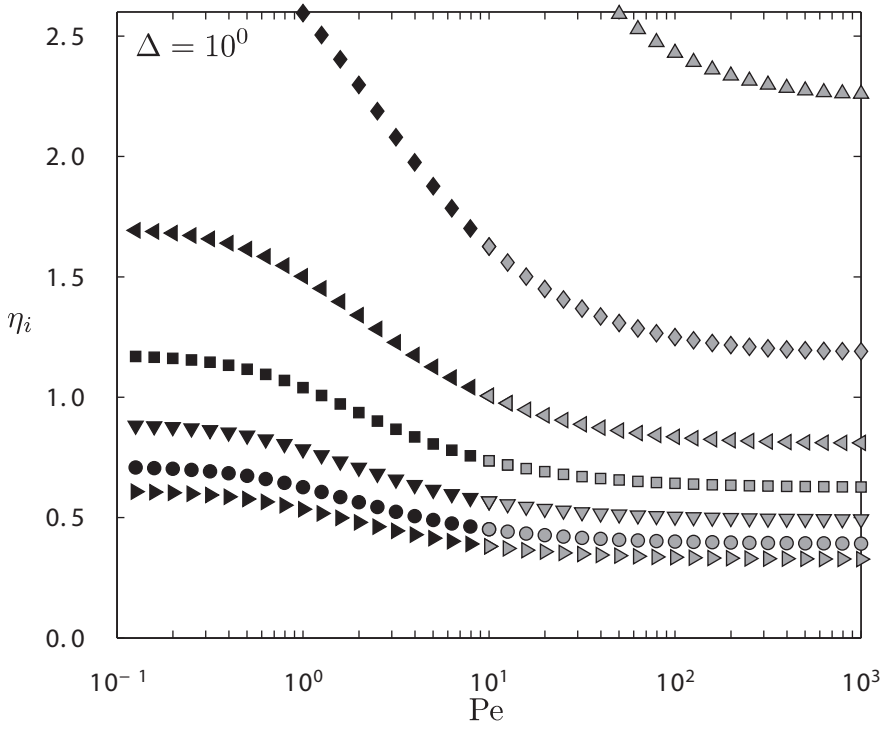

Figure D.25: Zoomed-in view of total intrinsic microviscosity for small probes as a function of Pe for an excluded annulus parameter Δ of 10^0.

Bibliography

[1] James R. Abbott, Alan L. Graham, Lisa A. Mondy, and Howard Brenner. Dispersion of a ball settling through a quiescent neutrally buoyant suspension. *J. Fluid Mech.*, 361:309–331, 1998.

[2] A. Acrivos and T. D. Taylor. Heat and mass transfer from single spheres in Stokes flow. *Phys. Fluids*, 5:387–394, 1965.

[3] G. K. Batchelor. Sedimentation in a dilute dispersion of spheres. *J. Fluid Mech.*, 52:245–268, 1972.

[4] G. K. Batchelor. Brownian diffusion of particles with hydrodynamic interaction. *J. Fluid Mech.*, 74:1–29, 1976.

[5] G. K. Batchelor. Sedimentation in a dilute polydisperse system of interacting spheres. Part 1. General theory. *J. Fluid Mech.*, 119:379–408, 1982.

[6] G. K. Batchelor. Corrigendum. *J. Fluid Mech.*, 137:467–469, 1983.

[7] G. K. Batchelor. Diffusion in a dilute polydisperse system of interacting spheres. *J. Fluid Mech.*, 131:155–175, 1983.

[8] G. K. Batchelor and C.-S. Wen. Sedimentation in a dilute polydisperse system of interacting spheres. Part 2. Numerical results. *J. Fluid Mech.*, 124:495–528, 1982.

[9] John F. Brady. Model hard-sphere dispersions: statistical mechanical theory, simulations, and experiments. *Current Opinion in Colloid & Interface Science*, 1:472–480, 1996.

[10] John F. Brady. Particle motion driven by solute gradients with application to autonomous motion: continuum and colloidal perspectives. *J. Fluid Mech.*, 667:216–259, 2011.

[11] H. Brenner, A. L. Graham, J. R. Abbott, and L. A. Mondy. Theoretical basis for falling-ball rheometry in suspensions of neutrally buoyant spheres. *Int. J. Multiphase Flow*, 16(4):579–596, 1990.

[12] Ileana C. Carpen and John F. Brady. Microrheology of colloidal dispersions by Brownian dynamics simulations. *J. Rheol.*, 49(6):1483–1502, 2005.

[13] Ubaldo M. Córdova-Figueroa. *Directed motion of colloidal particles via chemical reactions: Osmotic propulsion*. PhD thesis, California Institute of Technology, 2008.

[14] Ubaldo M. Córdova-Figueroa and John F. Brady. Osmotic propulsion: The osmotic motor. *Phys. Rev. Lett.*, 100(15):158303–1–158303–4, 2008.

[15] John C. Crocker, M. T. Valentine, Eric R. Weeks, T. Gisler, P. D. Kaplan, A. G. Yodh, and D. A. Weitz. Two-point microrheology of inhomogeneous soft materials. *Phys. Rev. Lett.*, 85(4):888–891, 2000.

[16] R. H. Davis and N. A. Hill. Hydrodynamic diffusion of a sphere sedimenting through a dilute dispersion of neutrally buoyant spheres. *J. Fluid Mech.*, 236, 1992.

[17] Ryan J. DePuit, Aditya S. Khair, and Todd M. Squires. A theoretical bridge between linear and nonlinear microrheology. *Phys. Fluids*, 23:063102–1–063102–13, 2011.

[18] Stephen J. Ebbens and Jonathan R. Howse. In pursuit of propulsion at the nanoscale. *Soft Matter*, 6:726–738, 2010.

[19] I. Gazuz and M. Fuchs. Nonlinear microrheology of dense colloidal suspensions: A mode-coupling theory. *Phys. Rev. E*, 87:032304–1–032304–20, 2013.

[20] Jazmin Godoy, Guillaume Vives, and James M. Tour. Toward chemical propulsion: Synthesis of ROMP-propelled nanocars. *ACS Nano*, 5(1):85–90, 2011.

[21] John R. Happel and Howard Brenner. *Low Reynolds Number Hydrodynamics: with Special Applications to Particulate Media*. Springer, 1965.

[22] Jonathan R. Howse, Richard A. K. Jones, Anthony J. Ryan, Tim Gough, Reza Vafabakhsh, and Ramin Golestanian. Self-motile colloidal particles: From directed propulsion to random walk. *Phys. Rev. Lett.*, 99:048102–1–048102–4, 2007.

[23] Kyu Hyun, Manfred Wilhelm, Christopher O. Klein, Kwang Soo Cho, Jung Gun Nam, Kyung Hyun Ahn, Seung Jong Lee, Randy H. Ewoldt, and Gareth H. McKinley. A review of nonlinear oscillatory shear tests: Analysis and application of large amplitude oscillatory shear (LAOS). *Progress in Polymer Science*, 36:1697–1753, 2011.

[24] Rustem F. Ismagilov, Alexander Schwartz, Ned Bowden, and George M. Whitesides. Autonomous movement and self-assembly. *Agnew. Chem. Int. Ed.*, 41(4):652–654, 2002.

[25] D. J. Jeffrey and Y. Onishi. Calculation of the resistance and mobility functions for two unequal rigid spheres in low-Reynolds-number flow. *J. Fluid Mech.*, 139:261–290, 1984.

[26] Frank Jülicher and Jacques Prost. Comment on "Osmotic propulsion: The osmotic motor". *Phys. Rev. Lett.*, 103(7):079801–1, 2009.

[27] Frank Jülicher and Jacques Prost. Generic theory of colloidal transport. *Euro. Phys. J. E*, 29(1):27–36, 2009.

[28] Aditya S. Khair and John F. Brady. "microviscoelasticity" of colloidal dispersions. *J. Rheol.*, 49(6):1449–1481, 2005.

[29] Aditya S. Khair and John F. Brady. Single particle motion in colloidal dispersions: a simple model for active and nonlinear microrheology. *J. Fluid Mech.*, 557:73–117, 2006.

[30] Aditya S. Khair and John F. Brady. On the motion of two particles translating with equal velocities through a colloidal dispersion. *Proc. R. Soc. A*, 463:223–240, 2007.

[31] Aditya S. Khair and John F. Brady. Microrheology of colloidal dispersions: Shape matters. *J. Rheol.*, 52(1):165–196, 2008.

[32] Aditya S. Khair and Todd M. Squires. Active microrheology: A proposed technique to measure normal stress coefficients of complex fluids. *Phys. Rev. Lett.*, 105(15):156001–1–156001–4, 2010.

[33] Sangtae Kim and Seppo J. Karrila. *Microhydrodynamics: Principles and Selected Applications*. Butterworth-Heinemann, 1991.

[34] A. M. Leshansky. Actin-based propulsion of a microswimmer. *Phys. Rev. E*, 74:012901–1–012901–4, 2006.

[35] J. Liu, M. L. Gardel, K. Kroy, E. Frey, B. D. Hoffman, J. C. Crocker, A. R. Bausch, and D. A. Weitz. Microrheology probes length scale dependent rheology. *Phys. Rev. Lett.*, 96(11):118104–1–118104–4, 2006.

[36] Brent J. Maranzano and Norman J. Wagner. The effects of particle size on reversible shear thickening of concentrated colloidal dispersions. *J. Chem. Phys.*, 114(23):10514, 2001.

[37] T. G. Mason and D. A. Weitz. Optical measurements of frequency-dependent linear viscoelastic moduli of complex fluids. *Phys. Rev. Lett.*, 74(7):1250–1253, Feb 1995.

[38] Tihana Mirkovic, Nicole S. Zacharia, Gregory D. Scholes, and Geoffrey A. Ozin. Fuel for thought: Chemically powered nanomotors out-swim nature's flagellated bacteria. *ACS Nano*, 4(4):1782–1789, 2010.

[39] Jeffrey F. Morris and John F. Brady. Self-diffusion in sheared suspensions. *J. Fluid Mech.*, 312:223–252, 1996.

[40] H. Nicolai, B. Herzhaft, E. J. Hinch, L. Oger, and E. Guazzelli. Particle velocity fluctuations and hydrodynamic self-diffusion of sedimenting non-Brownian spheres. *Phys. Fluids*, 7:12–23, 1995.

[41] Ryan A. Pavlick, Samundra Sengupta, Timothy McFadden, and Ayusman Sen. A polymerization-powered motor. *Agnew. Chem. Int. Ed.*, 50(40):9374–9377, 2011.

[42] Walter F. Paxton, Kevin C. Kistler, Christine C. Olmeda, Ayusman Sen, Sarah K. St. Angelo, Yanyan Cao, Thomas E. Mallouk, Paul E. Lammert, and Vincent H. Crespi. Catalytic nanomotors: Autonomous movement of striped nanorods. *J. Am. Chem. Soc.*, 126:13424–13431, 2004.

[43] E. M. Purcell. Life at low Reynolds number. *Am. J. Phys.*, 45(1):3–11, 1977.

[44] Patrick T. Reardon, Alan L. Graham, James R. Abbott, and Howard Brenner. Experimental observations of non-continuum effects in suspensions: Falling-ball versus towed-ball rheometry. *Phys. Fluids*, 17:093101–1–093101–7, 2005.

[45] William B. Russel. The Huggins coefficient as a means for characterizing suspended particles. *J. Chem. Soc., Faraday Trans. 2*, 80:31–41, 1984.

[46] Kelly M. Schultz, Alexandra V. Bayles, Aaron D. Baldwin, Kristi L. Kiick, and Eric M. Furst. Rapid, high resolution screening of biomaterial hydrogelators by μ^2Rheology. *Biomacromolecules*, 12:4178–4182, 2011.

[47] Kelly M. Schultz and Eric M. Furst. High-throughput rheology in a microfluidic device. *Lab Chip*, 11:3802–3809, 2011.

[48] Nima Sharifi-Mood, Joel Koplik, and Charles Maldarelli. Diffusiophoretic self propulsion of colloids driven by a surface reaction: The sub-micron particle regime for exponential and van der Waals interactions. *Phys. Fluids*, 25:012001–1–012001–34, 2013.

[49] Todd M. Squires and John F. Brady. A simple paradigm for active and nonlinear microrheology. *Phys. Fluids*, 17:073101–1–073101–21, 2005.

[50] Todd M. Squires and Thomas G. Mason. Fluid mechanics of microrheology. *Annu. Rev. Fluid Mech.*, 42:413–438, 2010.

[51] Indira Sriram and Eric M. Furst. Out-of-equilibrium forces between colloids. *Soft Matter*, 8:3335–3341, 2012.

[52] Indira Sriram, Alexander Meyer, and Eric M. Furst. Active microrheology of a colloidal suspension in the direct collision limit. *Phys. Fluids*, 22:062003–1–062003–10, 2010.

[53] Geoffrey I. Taylor. Analysis of the swimming of microscopic organisms. *Proc. R. Soc. Lond. A*, 209(1099):447–461, 1951.

[54] Julie A. Theriot and Timothy J. Mitchison. Actin microfilament dynamics in locomoting cells. *Nature*, 352:126–131, 1991.

[55] Julie A. Theriot, Timothy J. Mitchison, Lewis G. Tilney, and Daniel A. Portnoy. The rate of actin-based motility of intracellular Listeria monocytogenes equals the rate of actin polymerization. *Nature*, 357:257–260, 1992.

[56] I. Theurkauff, C. Cottin-Bizonne, J. Palacci, C. Ybert, and L. Bocquet. Dynamic clustering in active colloidal suspensions with chemical signaling. *Physical Review Letters*, 108:268303–1–268303–5, 2012.

[57] T. A. Waigh. Microrheology of complex fluids. *Rep. Prog. Phys.*, 68:685–742, 2005.

[58] Joseph Wang. Can man-made nanomachines compete with nature biomotors? *ACS Nano*, 3(1):4–9, 2009.

[59] Laurence G. Wilson and Wilson C. K. Poon. Small-world rheology: an introduction to probe-based active microrheology. *Phys. Chem. Chem. Phys.*, 13:10617–10630, 2011.

[60] Roseanna N. Zia and John F. Brady. Single particle motion in colloids: Force-induced diffusion. *J. Fluid Mech.*, 658:188–210, 2010.

[61] Roseanna N. Zia and John F. Brady. Microviscosity, microdiffusivity, and normal stresses in colloidal dispersions. *J. Rheol.*, 56(5):1175–1208, 2012.

[62] Roseanna N. Zia and John F. Brady. Stress development, relaxation, and memory in colloidal dispersions: Transient nonlinear microrheology. *J. Rheol.*, 57(2):457–492, 2013.